THE EFFECT OF ARTIFICIAL DAMAGES ON ELECTRICAL IMPEDANCE IN CARBON NANOFIBER-MODIFIED GLASS FIBER/EPOXY COMPOSITES AND THE DEVELOPMENT OF FDEIT

by

Yuhao Wen

A Thesis

Submitted to the Faculty of Purdue University

In Partial Fulfillment of the Requirements for the degree of

Master of Science in Aeronautics and Astronautics

School of Aeronautics and Astronautics
West Lafayette, Indiana
May 2022

THE PURDUE UNIVERSITY GRADUATE SCHOOL
STATEMENT OF COMMITTEE APPROVAL

Dr. Tyler N. Tallman, Chair

School of Aeronautics and Astronautics

Dr. R. Byron Pipes

School of Aeronautics and Astronautics

Dr. Wenbin Yu

School of Aeronautics and Astronautics

Approved by:

Dr. Gregory A. Blaisdell

For Mom, Dad, and Sister

ACKNOWLEDGMENTS

First, I would like to express my sincere gratitude to my advisor, Dr. Tyler Tallman. I am grateful for his guidance and support for my graduate studies in the school of Aeronautics and Astronautics at Purdue University. His inspiring opinions and encouragement have helped me in every aspect of my research career. I am honored to have the opportunity to work with such an outstanding and inspiring advisor. Thank you, Dr. Tallman.

I would like to thank Dr. R. Byron Pipes and Dr. Wenbin Yu for their advice in my first year of study at Purdue University. I was uncertain about the research direction or the major's focus when I first came to Purdue. Without their help, I could never find the goal for my graduate studies. I would also like to thank them for being part of my defense and taking the time to offer their insights.

I am thankful to all my fellow lab mates for their support and helps. I have learn a lot from their advice and comments on my work over the past two years. I also want to thank Julio A. Hernandez particularly for his continuous encouragement and professional suggestions. His support and positive attitudes have brought me confidence in pursuing my goal.

Lastly, I would like to thank my fiancee, Wei Huang, for supporting me. Her company and encouragement throughout the years had helped me through all the difficulties in life. I would not have the determination to finish my graduate study without her help. I would also like to thank my parents, Xiaoye Weng and Chuanjian Wen, and my dear sister, Longyi Wen, for their support and confidence in me for all the years I studied abroad. Last but not least, I want to thank all my friends, especially Junyu Wang, for all the fun time we spent together that kept the boredom and stress away throughout all the years abroad.

TABLE OF CONTENTS

LIST OF FIGURES

LIST OF SYMBOLS

$\delta\xi$	admittivity change distribution
δ_{ij}	Kronecker-delta
ϵ	permittivity
ω	angular frequency
ρ	domain resistivity
$\sigma_{\omega_{\mathrm{i}}}$	AC conductivity measured at ith frequency value
σ_{AC}	AC conductivity
σ_{DC}	DC conductivity
θ	phase angle
ξ	electrical admittivity
A	cross-sectional area
C_{i}	parallel capacitor
D	distance between two inner probes in four-probe measurement
E_l	area of the lth electrode
$F(\xi)$	forward model electrode voltages
I	injected current vector
J	sensitivity matrix
j	imaginary unit
L	total number of electrodes
L_s	length of specimen
n	outward-pointing normal vector
R	experimentally measured resistance
$R(\delta\xi)$	regularization term
R_{i}	parallel resistor
R_0	series resistor
U	vector domain potential
u	domain potential
V	electrode voltage vector

V_D	voltage measured between two inner probes in four-probe measurement
V_d	difference between two voltage vectors
V_l	voltage of the lth electrode
x	position vector
Z	complex impedance
$Z_{\mathrm{eq}}(\omega)$	complex impedance for equivalent circuit
z_l	contact impedance between lth electrode and the domain

ABBREVIATIONS

AC	alternating current
CB	carbon black
CFRP	carbon-fiber-reinforced polymers
CNF	carbon nanofiller/nanofiber
CNT	carbon nanotube
DC	direct current
EIT	electrical impedance tomography
EIS	electrical impedance spectroscopy
EMI	electromechanical impedance method
ERT	electrical resistance tomography
fdEIT	frequency difference electrical impedance tomography
FRP	fiber-reinforced polymer
GFRC	glass fiber reinforced composite
GNP	graphene nanoplatelets
GREIT	Graz consensus reconstruction electrical impedance tomography
LVDT	linear variable differential transformers
NDE	non-destructive evaluation
MWCNT	multi-walled carbon nanotube
TV	total variation regularization
tdEIT	time difference electrical impedance tomography
PWAS	piezoelectric wafer active sensors
PZT	lead zirconia titanate
SHM	structural health monitoring

ABSTRACT

Self-sensing materials are engineered to transduce mechanical effects like deformations and damages into detectable electrical changes. As such, they have received immense research attention in areas including aerospace, civil infrastructure, robotic skin, and biomedical devices. In structural health monitoring (SHM) and nondestructive evaluation (NDE) applications, damages in the material cause breakage in the conductive filler networks, resulting in changes in the material's conductivity. Most SHM and NDE applications of self-sensing materials have used direct current (DC) measurements. DC-based methods have shown advantages with regard to sensitivity to microscale damages compared to other SHM methods. Comparatively, alternating current (AC) measurement techniques have shown potential for improvement over existent DC methods. For example, using AC in conjunction with self-sensing materials has potential for benefits such as greater data density, higher sensitivity through electrodynamics effects (e.g., coupling the material with resonant circuitry), and lower power requirements. Despite these potential advantages, AC techniques have been vastly understudied compared to DC techniques.

To overcome this gap in the state of the art, this thesis presents two contributions: First, an experimental study is conducted to elucidate the effect of different damage types, numbers, and sizes on AC transport in a representative self-sensing composite. And second, experimental data is used to inform a computational study on using AC methods to improve damage detection via electrical impedance tomography (EIT) – a conductivity imaging modality commonly paired with self-sensing materials for damage localization. For the first contribution, uniaxial glass fiber specimens containing 0.75 wt.% of carbon nanofiber (CNF) are induced with five types of damage (varying the number of holes, size of holes, number of notches, size of notches, and number of impacts). Impedance magnitude and phase angle were measured after each permutation of damage to study the effect of the new damage on AC transport. It was observed that permutations of hole and notch damages show clear trends of increasing impedance magnitude with the increasing damage, particularly at low frequencies. These damages had little-to-no effect on phase angle, however. Increasing numbers of impacts on the specimens did not show any discernable trend in ei-

ther impedance magnitude or phase angle, except at high frequencies. This shows that different AC frequencies can be more or less useful for finding particular damage types.

Regarding the second contribution, AC methods were also explored to improve damage detection in self-sensing materials via EIT. More specifically, the EIT technique could benefit from developing a baseline-free (i.e., not requiring a ‘healthy’ reference) formulations enabled by frequency-difference (fd) imaging. For this, AC conductivity measurements ranging from 100 Hz to 10 MHz were collected from various weight fractions of CNF-modified glass fiber/epoxy laminates. This experimental data was used to inform fdEIT simulations. In the fdEIT simulations, damage was simulated as a simple through-hole. Simulations used 16 electrodes with four equally spaced electrodes on each side of the domain. The EIT forward problem was used to predict voltage-current response on the damaged mesh, and a fdEIT inverse problem was formulated to reconstructs the damage state on an undamaged mesh. The reconstruction images showed the simulated damage clearly. Based on this preliminary study, this research shows that fdEIT does have potential to eliminate the need for a healthy baseline in NDE applications, which can potentially help proliferate the use of this technique in practice.

1. INTRODUCTION

1.1 Literature Review

Self-sensing materials have potential to be important in a broad spectrum of technological fields such as biomedical engineering [1] [2], aerospace structures [3] [4], civil engineering [5] [6] [7], and automotive industries [8] [9] [10] as they provide continuous health monitoring and improve the safety of structures and durability without (or minimally) affecting their designed functionality. Therefore, self-sensing materials have received considerable attention for their potential in SHM and NDE. As an example, in biomedical engineering, a study promotes the usage of the electromechanical impedance method (EMI), which is a commonly investigated method of SHM, in the procedure of total knee replacement (TKR) on embedded lead zirconate titanate piezoelectric transducers (PZTs) in the polymer bearing component of the TKR [1]. A common TKR procedure is shown in Figure 1.1. According to the article, 20% of patients after TKR procedures have reported being dissatisfied with the implant due to loosening of the implant components or infections around the implant area. In order to prevent such structural failures in the component as well as possible material defects that eventually lead to infections, the study suggests applying EMI techniques. These methods have also shown positive outcomes in detecting structure stability in dental implants [2], with the combination of PZTs to perform continuous self-powered health monitoring that utilizes the self-sensing and energy harvesting capabilities in PZTs. Such applications can reduce the stress on medical resources as the number of periodic screenings of the knee implants can be reduced and potentially allow patients to monitor the condition of their implants.

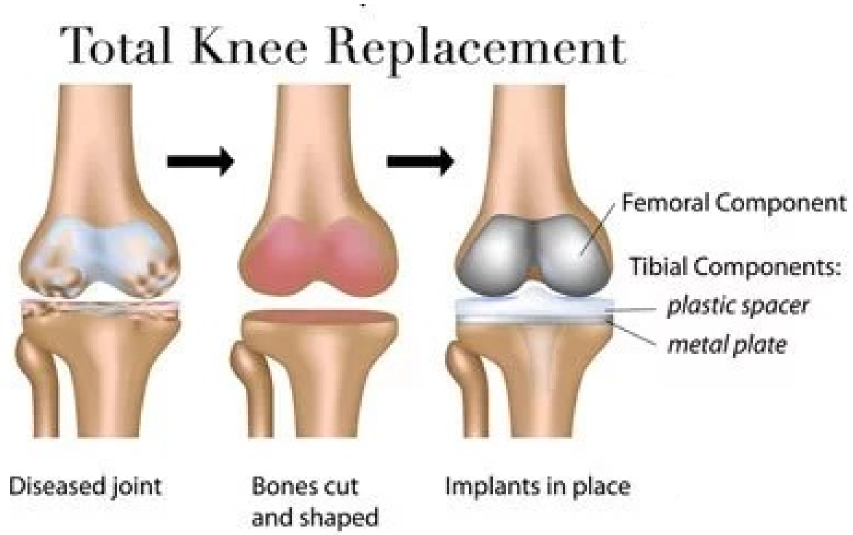

Figure 1.1. Total knee replacement schematic [11].

For another example, in a civil engineering case, researchers have focused on developing carbon fiber reinforced mortar to promote self-monitoring technique by reactance measurements [5]. Reinforced concrete with short carbon fibers has shown potential for low drying shrinkage, high flexural strength and toughness, tensile strength and ductility, and the ability to self-sense deformation and damage. As concrete is one of the most popularly used construction materials, applying self-sensing concrete on future civil construction can provide accessibility to SHM applications, improving the safety and durability of the structure. As another example, a study [6] also promoted the potential of continuous monitoring of the carbon-based cementitious composite to prevent potential crack propagation due to the inherent brittleness nature of the material. Research on using cost-efficient self-sensing materials such as graphene/fly ash geopolymeric composites as structure materials have shown highly sensitive and linear responses to axial tensile and compressive strain, promoting an alternative, low-cost option for self-sensing materials in civil applications that is economically scalable [7].

And as an aerospace-relevant example, Abot et al. [3] presented research on self-sensing composite that focused on using carbon nanotube (CNTs) materials to form sensor threads, which can detect in-plane damage and delamination in the composite material. Different sensor configurations are used to detect different types of damages in the composite. As shown in Figure 1.2, for in-plane strains/damages, continuous sensors threads are embedded into the tows of woven fabric reinforcement to detect strains aligned with the sensor threads direction. The sensor threads can also detect cracks that cross them. For out-of-plane strains or delamination, the sensor threads are pinned perpendicular to the material plane to detect interlaminar delamination or debonding. In addition, the use of self-sensing materials has advantages compared to embedded or attached sensors in aerospace applications. Eddib and Chung [4] have discussed that it is vital to continuously monitor the structural health of airframe to prevent failures due to aging in aircraft structures. Using self-sensing material may be a better option for embedded sensors in this case, since self-sensing materials do not show tendencies in mechanical properties degradation, and they also have advantages such as lower cost, higher durability, and larger sensing volume compared to embedded sensors.

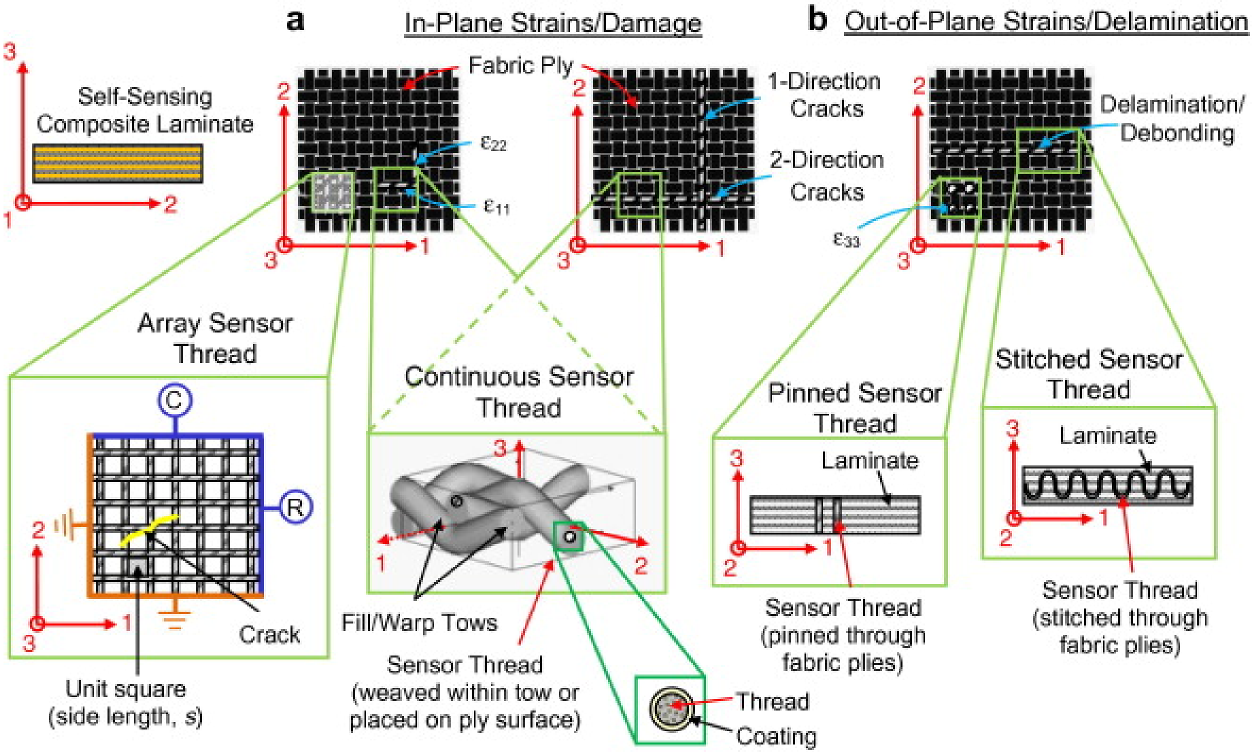

Figure 1.2. (a) Sensor threads are applied to the surface or embedded into the composite to detect cracks within its area. (b) Sensor configuration for out-of-plane and through-thickness damage detection [3].

Robotic engineers have also been developing soft robots that are suitable for complicated geometric locations and harsh environments with the use of self-sensing material to improve actuation and motion [12] [13] [14]. The studies utilized the piezoresistive characteristics exhibited in many self-sensing materials to transduce deformation in the robot arms made with self-sensing soft polymer to measurable electrical change to detect obstacles in moving direction. In addition, based on these works, soft robots can also benefit from self-sensing material by reducing structural complexity. Lo et al. [12] combined the actuation and self-sensing into a single composite material to reach the self-monitoring actuator. This allows the actuator to be constructed as a homogeneous structure, providing the ability to exhibit omni-directional and anisotropic locomotion, as well as preventing potential cracking and long-term damage due to modulus mismatch at the sensor-actuator interface.

Because of the large body of existent research on self-sensing materials in SHM and NDE, it is worthwhile to compare this approach to other modalities. Traditional applications of SHM utilize embedded sensors or sensors attached to surfaces, including linear variable differential transformers (LVDT), fiber optics, strain gages, and piezoelectric wafer active sensors (PWAS). These types of sensors mentioned can be commonly seen in civil applications [15] [16], aerospace structures [17] [18] [19], automobile [20], medical [21] [22], and robotics [23]. For example, for LVDT applications, Olivera et al. [24] proposed a cement-based stress/strain sensor with embedded magnetic microwire in cement-based composite (MMCC), as shown in Figure 1.3, to develop low-cost distributed sensors with wireless capabilities in order to reduce maintenance costs. For fiber optics applications, Kahandawa [17] discussed the use of fiber Bragg grating (FBG) sensors for SHM applications in aerospace fiber-reinforced polymer (FRP) structures to eliminate the effect on the strength of the part with embedded sensors. For strain gages applications, Choi et al. [15] presented an integrated solution that uses strain gage enabled wireless sensors nodes to monitor structural health conditions and provides the collected data for risk analysis in order to provide a wireless deployment of the monitoring system and promote cost-effective maintenance. Lin and Giurgiutiu [19] have developed PWAS using polyvinylidene fluoride (PVDF) instead of traditionally used PZT to overcome the brittleness in PZT-PWAS and provide better conformability on curved surfaces so that these types of sensors can be better applied on aerospace structures.

However, despite the aforementioned advantages of sensor applications in different fields, these applications are limited by the discrete nature of the sensors in the sense that the entire structure cannot be fully monitored unless the structure is built with an extensive network of sensors. Moreover, embedded sensor can cause potential mechanical property loss. Possible stress concentration can occur around the embedded sensor in fiber reinforced material if the sensor is much larger than the fiber in the material. Furthermore, the sensor could suffer with low durability and be hard to maintain since it is being embedded into the material. In some cases, such as biomedical implant mentioned previously in the TKR example, the built-in sensor method cannot be applied due to its requirement of wire attachments, which is hard to access as the patient cannot constantly have an open wound for the wire port.

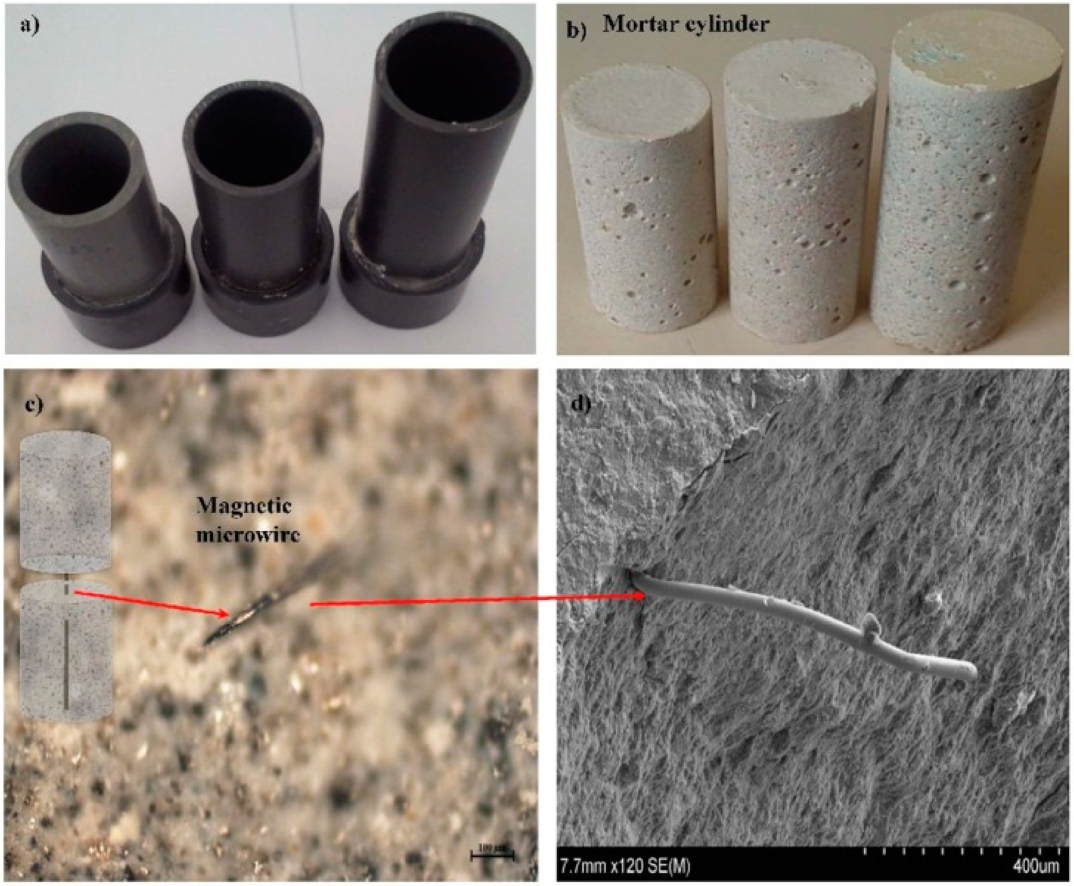

Figure 1.3. (a) Molds for MMCC sensors; (b) mortar cylinder with an embedded microwire; (c) optical micrograph of embedded microwire; (d) electronic micrograph of the embedded microwire [24].

In comparison, self-sensing materials show potential for overcoming the aforementioned shortcomings. Self-sensing materials eliminate the need to build sensors within the structure during or post-construction as the materials themselves are the sensors. This means that the use of self-sensing material can bring advantages such as low cost [7] [25], being capable of sensing a larger volume of the structure [26] [27] [28], reduce possible stress concentrations [29] [30], and high durability and with little to no maintenance [31] [32] [33]. The sensing behavior of the material is commonly approached through the piezoresistive effect, referring to having deformation dependent electrical properties. Some commonly used structural composites like carbon fiber-reinforced polymers also exhibit the piezoresistive effect. To achieve piezoresistivity in non-conductive materials (e.g., polymers and cements), conductive fillers such as CNFs [34] [35] or CNTs [36] [37] are dispersed into the matrix. Beyond imparting conductive and piezoresistive properties, this often also enhances to the mechanical properties of the matrix [38] [39] [40]. When sufficiently many conductive fillers are added, electrical percolation is reached, and material system becomes conductive [41] [42]. Mechanical effects such as deformation and damages to this type of material system will cause breakages in the nanofillers network or change the distance between fillers in the conductive network, resulting in changes in electrical conductivity. This allows subsurface mechanical effects to be detected by conductivity-based techniques. Therefore, conductivity-based methods have been developed in SHM and NDE that use the electrical measurement change in the self-sensing material to detect and locate the damaged area. Below, advantages in DC and AC conductivity-based methods are discussed.

1.2 DC-Based Methods

In the present majority of SHM/NDE applications using self-sensing materials, DC-based techniques are most used. DC-based methods are extensively applied in SHM/NDE for several reasons. First, the electrical resistance measurement method is particularly effective for detecting small and subtle defects in composite materials and in joints that involves metals, cement, and conductor filled polymers [43]. Cholker et al. [44] presented the applications of resistance-based technique on smart structural concrete that showed sensitive crack detection, as shown in Figure 1.4. Specimens were loaded at a constant rate until failure. Sudden drops in the faction change in resistance (FRC) curves indicate an increase of electrical resistance due to initiation of crack formations in the smart concrete. Mao et al. [45] also presented work in applying electrical resistance measurement to detect small defects in monitoring failure behavior of pultruded carbon-fiber-reinforced polymers (CFRP) composites. According to the article, an infrared thermography NDE technique was used to observe the temperature change in the specimen due to matrix deformation and cracking, fiber breakage, and debonding and delamination of composite. Combining the two techniques, it was found that the electrical resistance measurement was able to detect early damages in the tensile loading test of unidirectional CFRP composites.

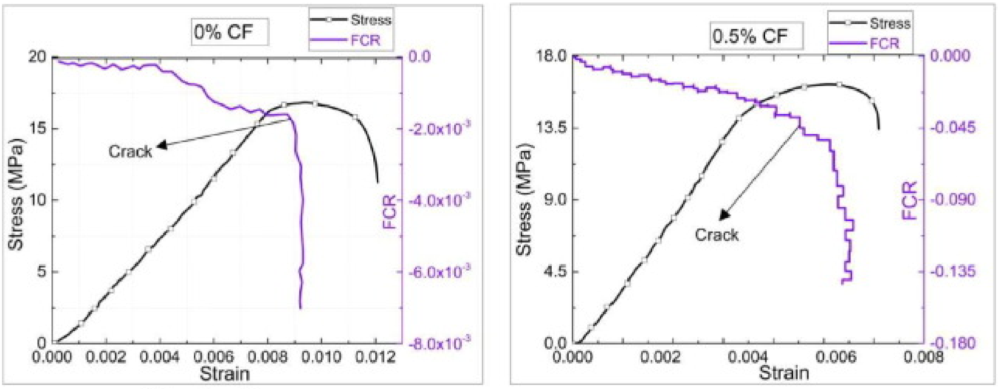

0% carbon fibers

0.5% carbon fibers

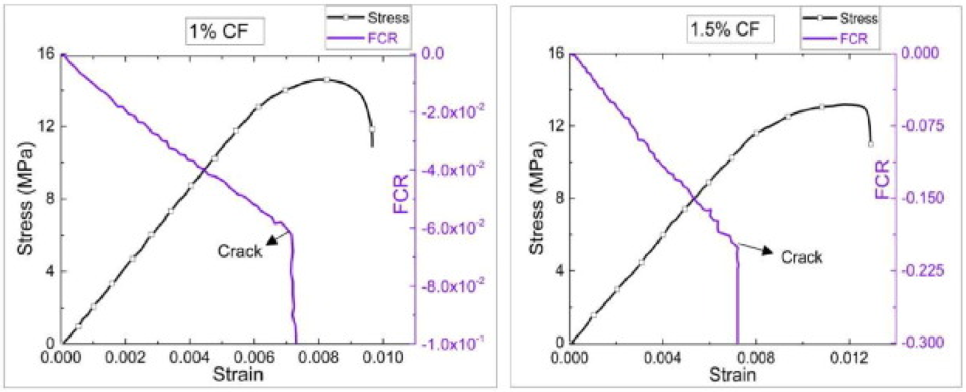

1% carbon fibers

1.5% carbon fibers

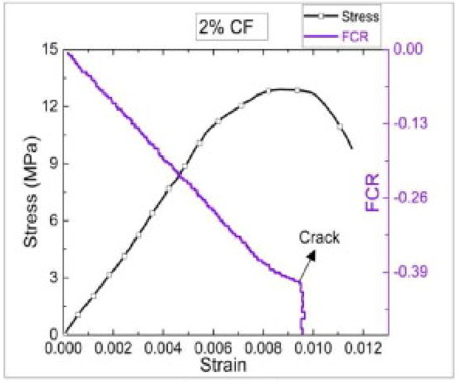

2% carbon fibers

Figure 1.4. Cracks detection in smart concrete [44].

Second, DC-based electrical measurements can be easily collected in real-time, allowing signal processing algorithms to also monitor structural health in real-time. Datta et al. [46] developed a fully probabilistic prognosis methodology to predict the real-time fatigue crack propagation using Bayesian techniques. As shown in Figure 1.5 (a), the crack growth rate was plotted as a function of cycles and showed fair agreement with the prediction from developed model. In Figure 1.5 (b), the results of predictions of crack length indicated that the developed model was able to predict crack length accurately within the 95% confidence intervals.

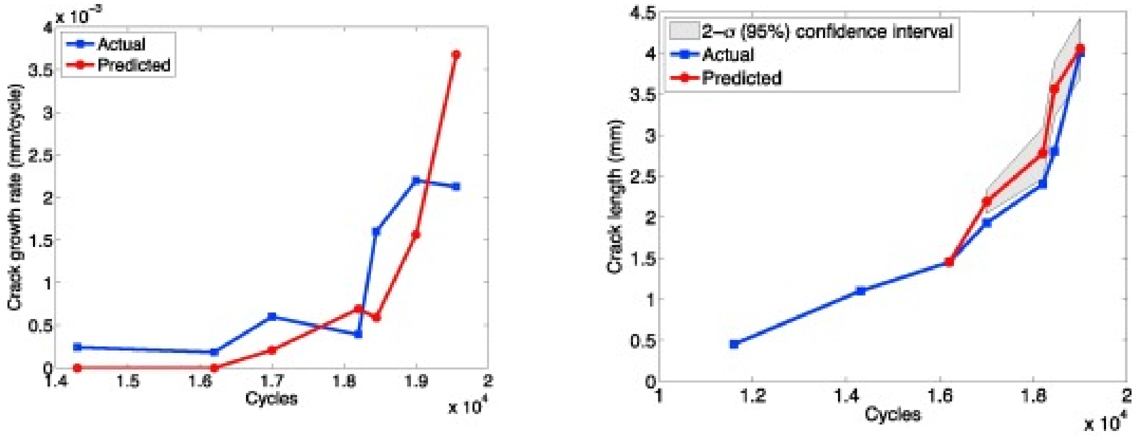

(a) Crack growth rate (b) Crack length

Figure 1.5. Crack length predictions [46].

And third, devices used in DC-based methods in general are low cost. Most of the experiments consist of DC electrical measurements on self-sensing material were conducted with the use of digital multimeters (DMMs) [44] [47] [48], which are basic testing tools that are commonly used to measure two or more electrical values such as voltage, current, and resistance. The use of DMMs also simplifies the equipment installation process, creates a simple and cost-effective work environment for SHM on self-sensing material.

However, even with the above-mentioned advantages, AC-based methods may have even greater potential. For example, AC in general has higher data density, higher sensitivity [5] [49] [50], and lower power requirement [51]. The details of AC-based methods are discussed below.

1.3 AC-Based Methods

Most NDE and SHM applications in self-sensing materials utilize DC measurement techniques due to the ease of use and low cost of the required test devices. Comparatively, AC measurement techniques have not received nearly as much attention despite several potential advantages. First, AC electrical transport provides greater data density. AC electrical measurements provide two sets of data: impedance and phase angle, which both can be utilized to detect and analyze deformations or damages. Comparatively, DC electrical measurements can provide only resistance. Second, AC has the potential to provide higher sensitivity through electrodynamic effects. For example, experiments have been conducted to show that sensitivity to damage can be improved by inducing electrical resonance in a CNF/epoxy material with the use of an external inductor [49]. Third, the AC conductivity of low filler weight fraction nanocomposites generally increases exponentially along with the interrogation frequency (i.e. the material exhibits capacitive transport) [51]. Due to the fact that piezoresistive materials generally have relatively high resistivity, AC techniques that use high frequency can lower power requirements in most applications.

Studies on AC-based method in SHM in the state of the art are summarized next. Fu et al. [5] extended work from self-monitoring in carbon fiber reinforced concrete with DC to AC because the AC electrical measurements can provide both resistance and reactance information for improving damage sensing ability. The research found that reactance is a more sensitive indicator than resistance. Abry et al. [50] monitored damages in CFRP laminates, comparing the results of DC and AC measurements. As shown in Figure 1.6, their results show that the curve of the AC measurements versus strain shows different shapes with a different layup of the laminates, that the [0/90] laminates exhibited moderate nonlinear strain behavior until the final failure, while the [90/0] laminates show more abruptly behavior correspondingly. Tallman [49] presented an investigation into the potential of using AC techniques to bolster piezoresistive nanocomposite-based damage detection in SHM. The study shows the shifts in electrical resonant frequencies can be used to detect damages in a CNF modified epoxy by connecting the CNF/epoxy nanocomposite into series and in parallel with an inductor. The results also indicate that the problem of poor sensitivity in detecting conductivity change from small damages can be improved with the use of AC techniques. Helseth [52] used electrical impedance spectroscopy (EIS) to characterize AC electrical properties of multi-walled carbon nanotubes (MWCNT)-modified polydimethylsiloxane (PDMS) under the effect of compressive loading. As shown in Figure 1.7, EIS curves under compression forces range from 2 N to 30 N vary and can be simulated using the single-relaxation time model (solid line). However, despite the references discussed above, AC methods are still vastly understudied compared to DC methods.

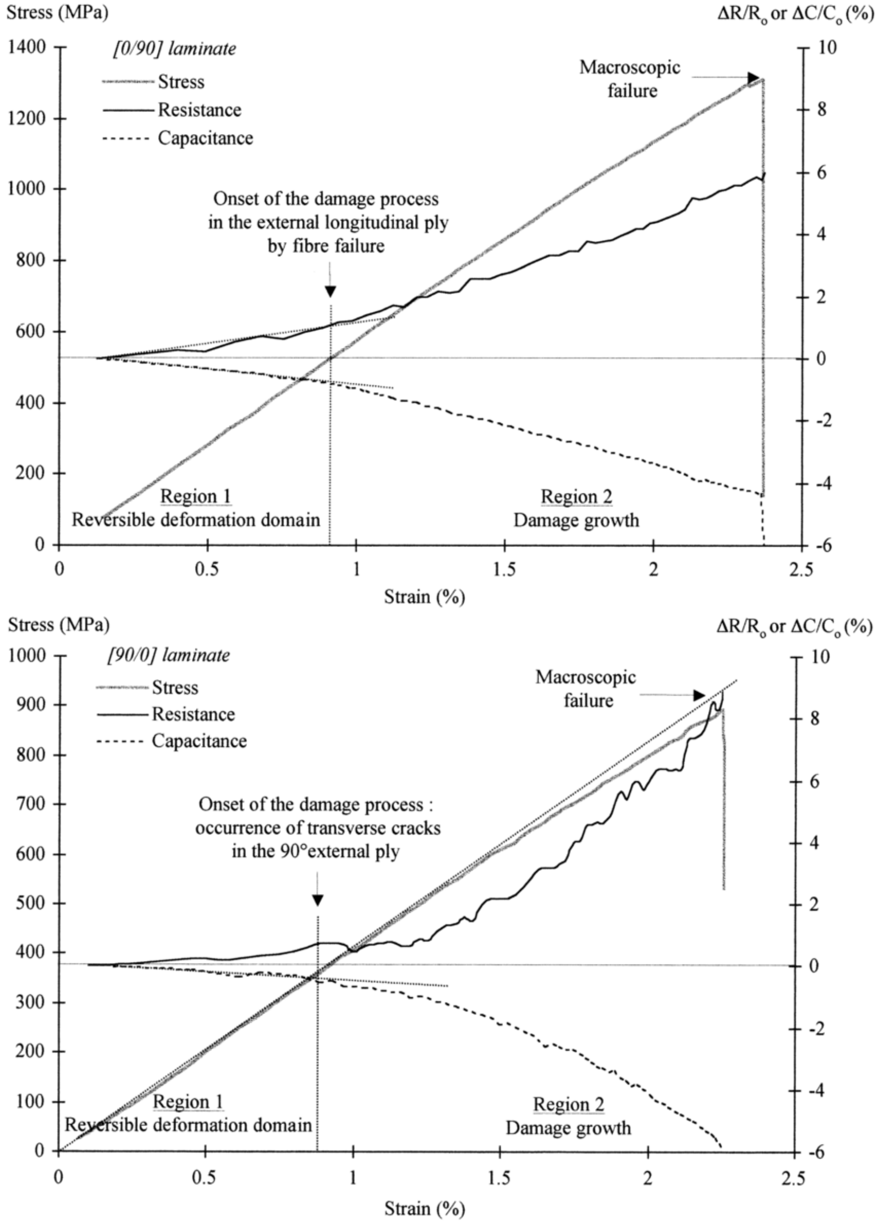

Figure 1.6. Changes in stress and AC measurements as a function of the applied strain during flexural monotonic loading for [0/90] (top) and [90/0] (bottom) composite [50].

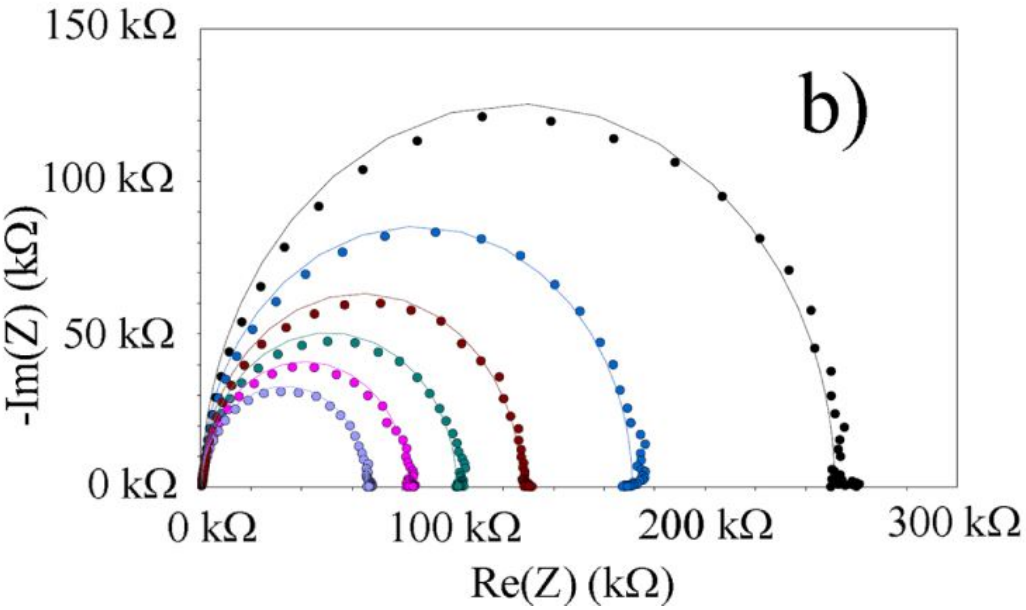

Figure 1.7. Effect of compressive loading on EIS curves of MWCNT modified PDMS [52].

1.4 Frequency Difference Electrical Impedance Tomography

In addition to just measuring impedance or resistance for self-sensing in these materials, EIT has been studied as a mean of detecting, localizing, and shaping deleterious effects in self-sensing materials [53] [54] [55] [56] [57]. EIT is a non-invasive imaging method that spatially maps the internal resistivity (or its inverse, conductivity) distribution of the domain based on voltage-current relations observed at the domain's boundary. It has shown great potential with its advantages of low cost, real-time employment, and non-ionizing characteristics. Early developments of EIT were for biomedical applications [58] [59], and the technique has since been applied to materials used in civil, aerospace, mechanical, and chemical engineering [60] [61] [62] [63] [64]. For example, Tallman et al. [65] showed that the damage could be reconstructed at the impact location on carbon black filler modified glass fibre/epoxy plates, as shown in Figure 1.8. However, EIT is a mathematically ill-posed inverse problem. As such, its imaging results can be markedly affected by factors such as experiment-to-model electrode misplacement, noise in electrical measurements, and deformation in the shape of the domain. To solve these problems, difference imaging techniques have been commonly used. Difference imaging takes boundary measurements from two different times then seeks to find the conductivity difference in the two measurements. In time-difference (td) imaging, pre-damage and post-damage measurements are taken. The practice of tdEIT in SHM has shown advantages in eliminating possible errors caused by experiment-to-model electrode misplacements, deformation in domain shape, and noise in the system. However, tdEIT needs data at the material's pristine state to function. In the realistic environment, pre-damage or baseline data could have been lost over time, or the baseline data was never collected due to the structure was constructed before the tdEIT was developed, or deformation occurred to the structure by natural disasters or erosion that made the baseline data irreverent to the later state of the structure.

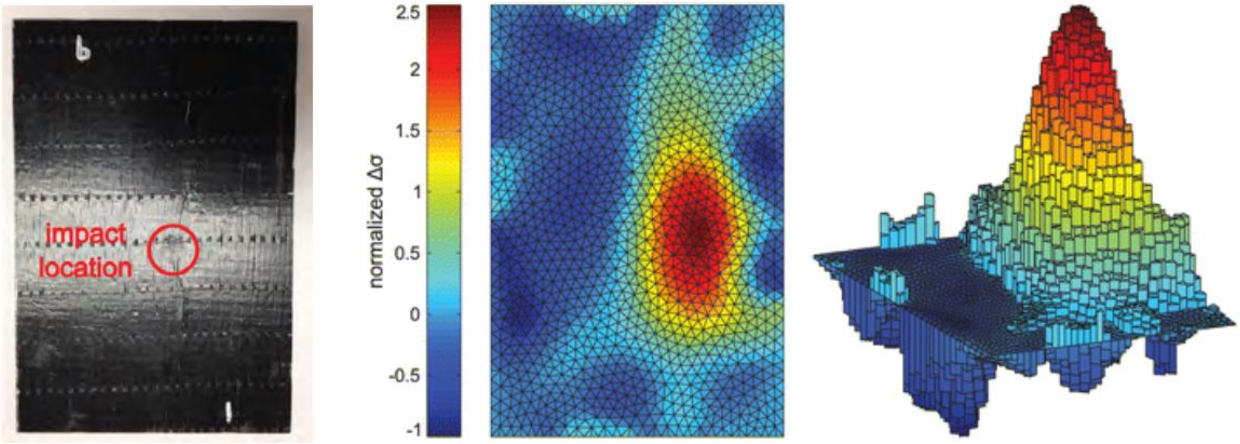

Figure 1.8. Damage reconstruction imaging in carbon black modified glass fibre/epoxy plate using EIT [65].

Due to the above-mentioned limits of tdEIT, the absence of baseline data in biomedical applications (e.g., tumor monitoring [66] [67], breast cancer screening [68] [69] [70], thorax imaging [71] [72]) have led to the development of multifrequency imaging methods. In these approaches, a difference between AC frequencies is used. That is, frequency-difference (fd) methods are commonly used by biomedical practitioners of EIT [73]. The fdEIT technique uses electrical measurements at two different frequencies to form a reconstruction image. This approach was initially developed in medical applications, such as cancer screening as mentioned previously, because baseline data (before tumor forms in the body) is extremely unlikely to be available. To counter this problem, a multifrequency method that collects electrical measurements at different frequencies was designed to reconstruct images [74] [75]. Chauveau et al. [76] have developed a multifrequency serial EIT system that can measure impedance within the frequency range from 1 kHz to 1 MHz. This work has performed tests on samples that use salt water to simulate the physiological background and 2 cm radius steel rods to simulate the tumorous tissue. As shown in Figure 1.10, it can be seen that this frequency-based approach has successfully captured the inclusion in both real and imaginary parts of images (as discussed later in this thesis, AC material properties have a real part and an imaginary part).

As another example example, Wu et al. [77] used the total variation regularization [78] formulation to promote a solution for monitoring tumor movement using EIT and experimentally explored this process in a phantom tank. Two separate voltage measurements of the background at 1 kHz and 50 kHz were collected, and the results of the reconstruction can be seen in Figure 1.9. As shown in the figure, conventional global weighted frequency different (GWFD) reconstruction showed the detection of the samples without indications of sample locations, while modified global weighted frequency difference (MGWFD) and limited region weighted frequency difference (ROI-WFD) reconstruction images showed indications of sample locations, but low in accuracy. This was due to the samples being too small that the presence of noise contaminated the signal. Despite several flaws in the results, this development has shown that the multi-frequency method for EIT has the potential to overcome the requirement of baseline data in tdEIT.

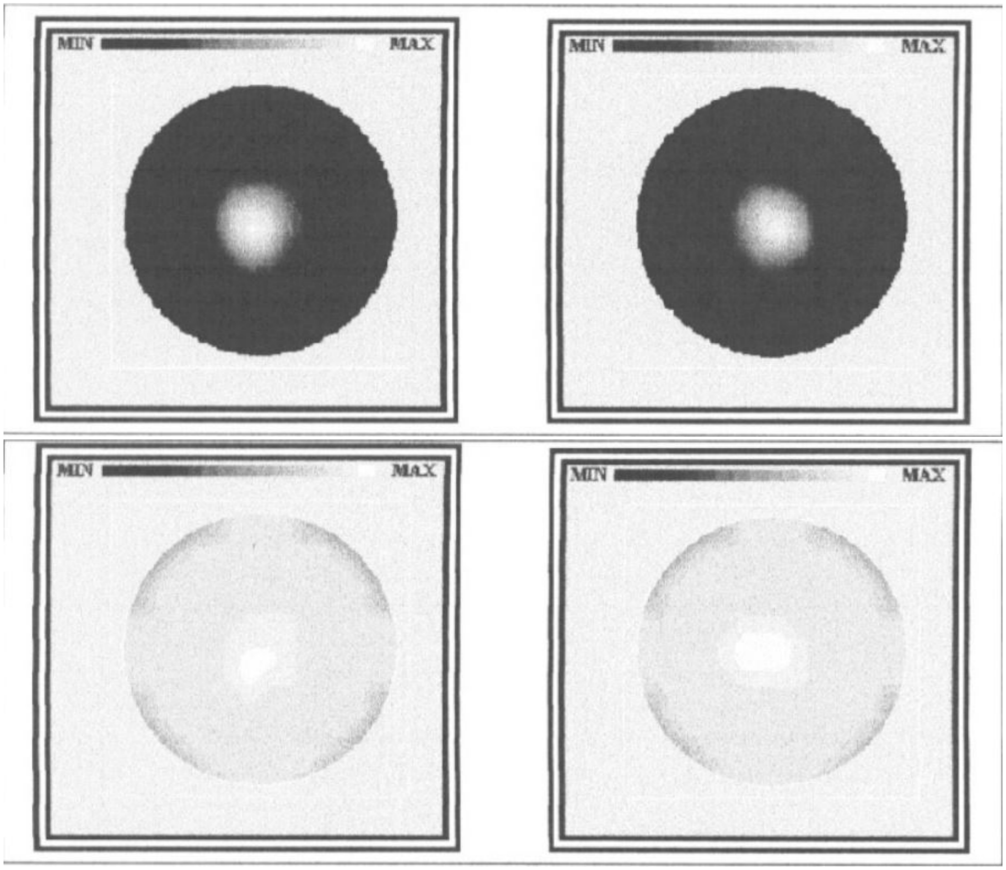

Figure 1.9. Real (top) and imaginary (bottom) part of images of a 2 cm radius steel rod in center at 10 kHz (left) and at 100 kHz (right) [76] .

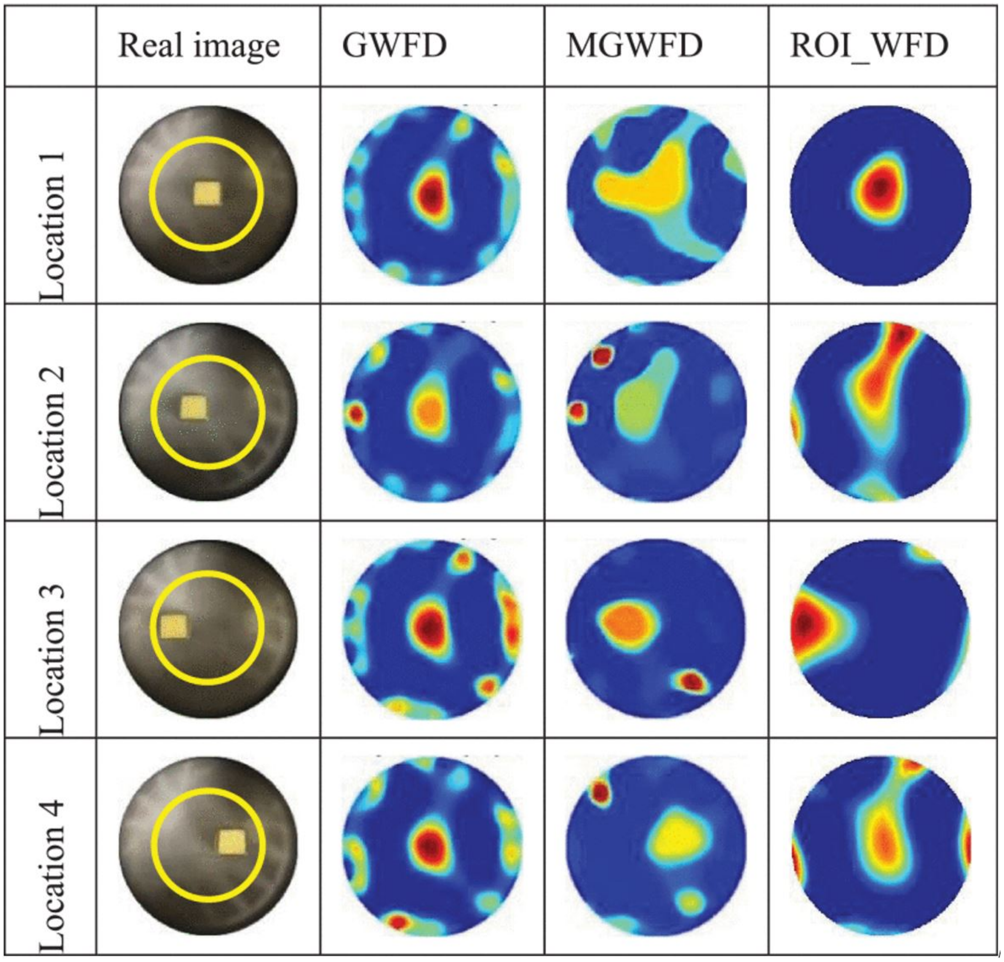

Figure 1.10. Theoretical model and reconstructions of small potato samples in 0.5% saline water background in a phantom tank [77].

fdEIT works in biological applications because physiological tissues exhibit frequency-dependent transport properties. Importantly, self-sensing materials also exhibit frequency-dependent transport properties. However, to the best of the author's knowledge, no materials practitioners of EIT have ever employed frequency-difference methods. This is an important oversight because fdEIT can potentially eliminate the need for a healthy baseline. Thus, in addition to the potential advantages of AC-based methods of self-sensing, we find another potential advantage with regard to damage imaging via fdEIT. Therefore, in addition to presenting AC conductivity measurements of artificially damaged specimens, this work will also present a study on the potential of utilizing fdEIT within experimentally informed computations.

2. PROBLEM STATEMENT AND RESEARCH GOAL

In light of the previous discussion, a great number of studies have been conducted in developing DC-based techniques for SHM/NDE applications using self-sensing materials. In contrast, significantly less work has been done with AC techniques. The lack of a basic understanding of damage-AC transport coupling is a bottleneck to the proliferation of AC-based self-sensing. Therefore, the following Problem Statement and Research Goal are formulated.

2.1 Problem Statement

Self-sensing materials have attracted immense attention in diverse and far-reaching applications due to their ability to transduce external stimuli into measurable property changes in a spatially continuous manner. In particular, self-sensing materials utilizing the piezoresistive effect have been extremely well-studied. However, work to date has focused overwhelmingly on the use of DC transport for self-sensing. This is important because AC-based techniques, though comparatively understudied, have significant potential advantages including providing greater data density, higher sensitivity, and lower power requirements. Thus, much greater knowledge into the basic responsiveness of AC transport in self-sensing materials to stimuli of interest is needed.

2.2 Research Goal

In light of the preceding Problem Statement, this research has two goals: Goal 1) Develop basic knowledge on the responsiveness of a representative self-sensing composite, CNF-modified glass fiber/epoxy, to various damage types. This goal is important because damage-AC transport relations are largely unstudied in the current state of the art. Utilizing AC-based self-sensing in structural materials therefore requires greater insight into how damage manifests in the electrical frequency response of the material. Goal 2) Explore the potential of AC to overcome the baseline limitation of EIT. This goal is important because existent EIT methods in this field are dependent on the availability of a health or pristine baseline. Removing this requirement could be a significant step towards the proliferation of conductivity imaging in materials research. Collectively, these two goals work towards closing the gap between DC and AC-based self-sensing.

2.3 Thesis Organization

The work presented in this thesis will be organized as follows: First, a discussion on theoretical aspects self-sensing materials including basic definitions, a summary of electrical transport mechanisms, and DC and AC measurement techniques will be presented. This will also include a brief introduction of fdEIT theory. Second, experimental procedures, including manufacture and preparation of test specimens, measurements of electrical properties, and EIT simulations formulation will be discussed. Third, results from through-hole, notch, impact damage testing, and the fdEIT simulation will be presented. Lastly, this thesis concludes with a summary, conclusions, and recommendations for future work.

3. THEORY

This chapter includes two sections regarding the theoretical context of the work performed in this thesis. The first section focuses on self-sensing materials and includes definitions of self-sensing materials and relevant nomenclature, describes how electrical changes occur due to damage or deformation, and summarizes DC and AC measurement techniques. The second section focuses on EIT and includes descriptions of the forward and the inverse problem.

3.1 Self-Sensing Materials

3.1.1 Introduction

Self-sensing materials have attracted attention from a wide variety of engineering disciplines. This includes areas such as robotics [12] [13] [14], biomedical engineering [1] [79], aerospace engineering [80] [81], and civil infrastructure [82] [83] [33]. This section includes the basic definition of self-sensing material, the physics of how damage or deformation in the self-sensing material leads to electrical changes, terminology used for describing DC and AC properties, and a summary of DC and AC measurement techniques. Advantages of self-sensing materials in one particular application, SHM, are also discussed.

Self-sensing materials can be broadly defined as materials that exhibit some measurable property change in response to external stimuli. The most common approach to self-sensing is via the piezoresistive effect. The piezoresistive effect refers to a material having deformation and damage-dependent electrical transport properties. A wide variety of materials, naturally occurring and engineered, exhibit piezoresistivity including biological materials [84], semi-saturated cements [85], soils [86], metals [87] [88] [89], carbon fiber composites [90] [91], and, among others, conductive filler-modified polymeric [92] [93], ceramic [94] [95], and cementitious composites [96] [97] [98]. Regarding the last example, carbon nanofiller-modified composites have received immense attention because ultra-high aspect ratio fillers such as CNTs and CNFs achieve electrical percolation at very low filler concentrations. To clarify, to achieve conductivity in a non-conductive matrix (e.g. epoxy), conductive fillers are added until they form a conductive network in the material. When the concentration of the conductive filler in the material exceeds a critical point, referred to as the percolation threshold, the material becomes conductive. Electrical transport through this network depends on connections between individual fillers. Thus, deformations that alter the connectedness of the network manifest as conductivity changes. This is schematically shown in Figure 3.1. In general, compressive deformation of the material decreases the distance between fillers, bringing more fillers in contact, increasing the conductivity. On the other hand, damages that break the filler connections in the conductive network and tensile deformations that increase the distance between fillers result in a decrease in conductivity. In short, this allows the material to sense its mechanical state by transducing mechanical changes (i.e. deformations and/or damages) into measurable electrical changes, making the material self-sensing.

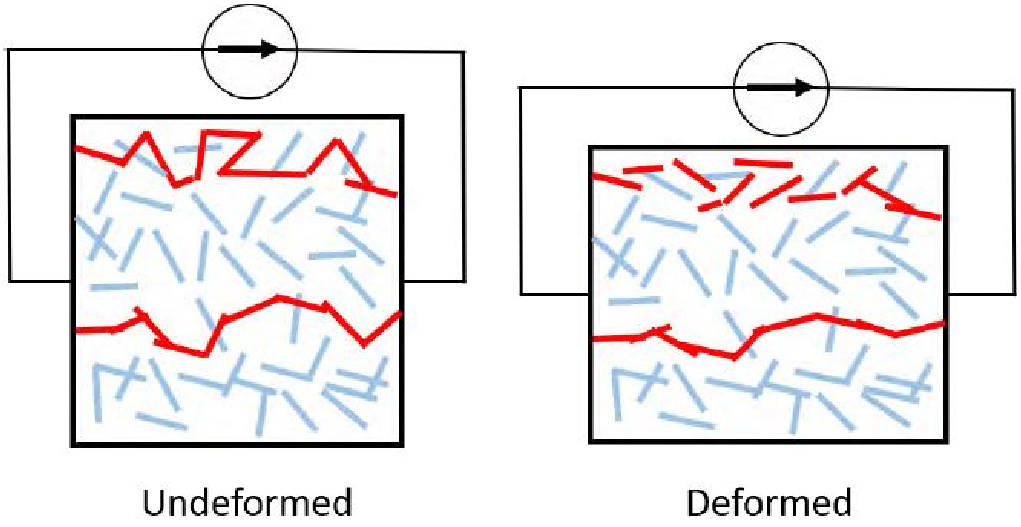

Figure 3.1. Depiction of nanofiller network in the piezoresistive nanocomposites. Resistivity changes due to applied deformation. Conductive path as shown in red is disconnected due to deformation. Left: undeformed state of nanofiller network. Right: deformed state of nanofiller network which increases the resistivity due to disconnection of conductive paths [99].

For DC transport, the nanofiller network can be considered as: 1) a collection of resistors in which each of the nanofillers can be treated as a resistor and 2) inter-nanofiller resistors where electrons can tunnel through the space (on the order of 1-2 nm) between sufficiently proximate nanofillers, as shown in Figure 3.2. Deformation in the material that alters the distance between nanofillers can affect the tunneling resistance, contributing to the piezoresistive effect.

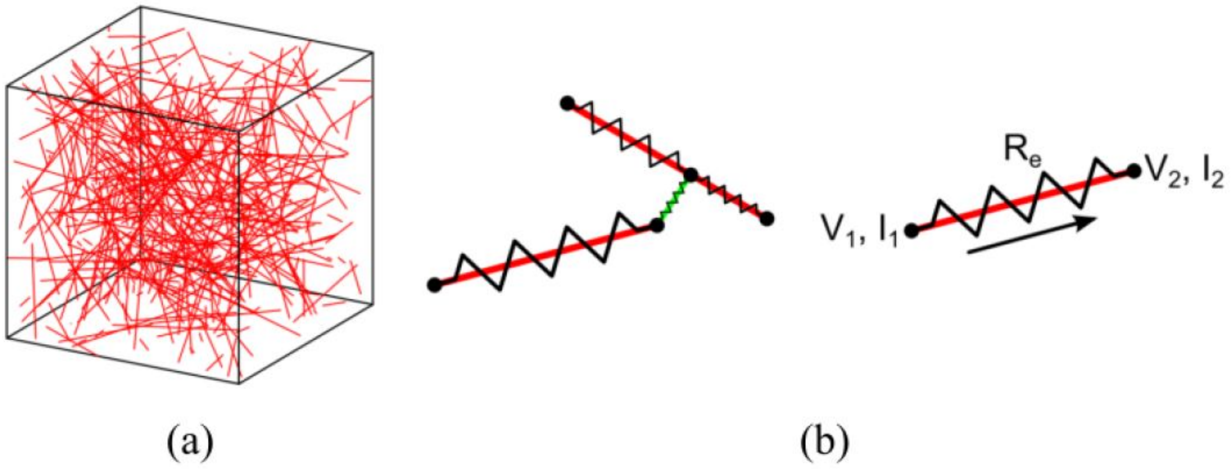

Figure 3.2. (a) Randomly distributed 0.4% CNT volume fraction network. (b) Schematic representation of two nanofiller (shown in red) discretized into resistor elements within tunneling range (shown in green) [100].

For AC transport, the nanofiller network provides different pathways including resistive, capacitive, inductive, and combinations of these ways for current to flow through [101] [102] [103]. As shown in Figure 3.3, Tallman and Hassan [101] showed that the nanofiller network can be discretized into linear circuit elements similar to the cases in DC transport.

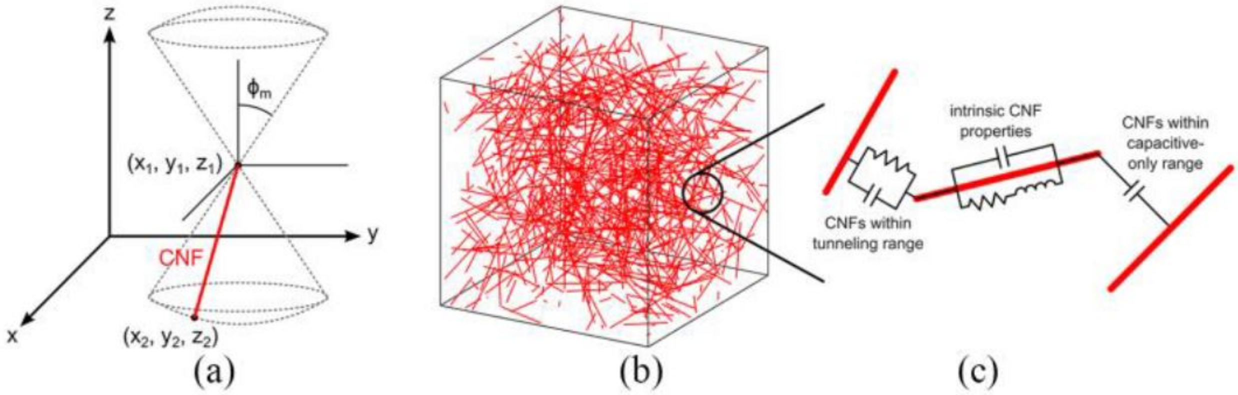

Figure 3.3. (a) CNFs are randomly generated within two spherical cones. (b) Representative CNF network in a domain. (c) CNFs and inter-CNFs junctions can be discretized into AC circuit elements [101].

Additionally, work from Sanli et al. [102] demonstrated that the nanofiller network can be reoriented under tensile strains, resulting in changes in the electrical pathway, as shown in Figure 3.4. These studies show that deformation or damages occurrence in the nanofiller network can affect the electrical pathways, resulting in changes in AC conductivity and contributing to AC piezoresistivity.

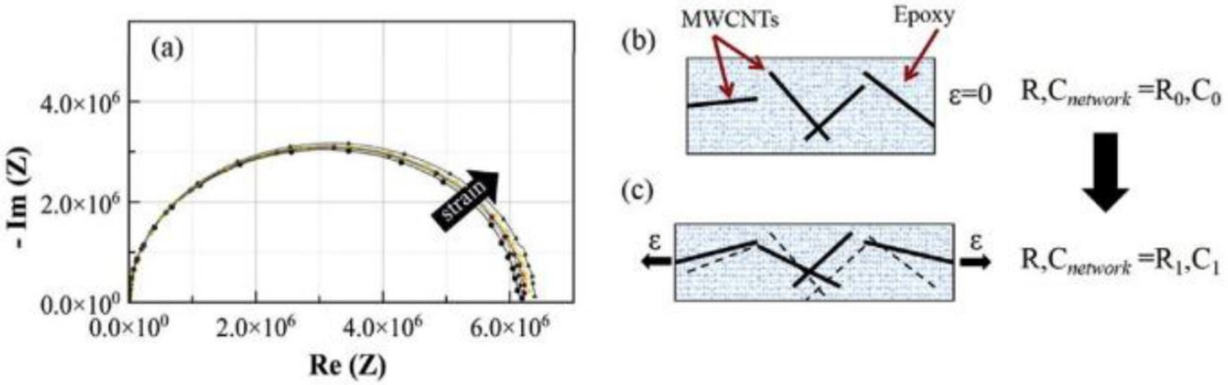

Figure 3.4. (a) Nyquist plot of MWCNT-modified epoxy nanocomposite. Illustration of change in electrical pathway with equivalent circuit elements from (b) unloaded states to (c) tensile strain state [102].

As a few representative examples of this type of piezoresistive self-sensing, cementitious [104] [105] and ceramics [106] [107] [108] materials have been studied in regard to civil applications. Structural polymers [109] [110] [111] are used in medical care (e.g., PMMA bone cement in cemented total joint replacements) and automobile applications. Commonly used conductive filler materials includes CNTs [112] [113], CNFs [114] [115], carbon black (CB) [106], graphene nanoplatelets (GNPs) [116] [117] [97], and silver particles [118] [119] [120]. More economic choices of filler material such as metallic waste power [121] have also been studied.

3.1.2 DC Measurement Techniques

In the current state of art, DC measurement techniques have been much more studied and applied to self-sensing materials. Chung [122] discussed pitfalls in using the two-probe method for resistance measurements and the advantages in using the four-probe method, which decouples specimen resistance from the contact resistance. The two-probe methods, however, are generally much easier implement. As shown in Figure 3.5 in a study of carbon fiber cement-matrix composite [123], done incorrectly, the two-probe method can give wildly inaccurate results. Alternative resistance methods include van der Pauw method [124], which is similar to the four-probe method, and the transmission line method [122] [125], which measures resistances between different pairs of lined up electrodes in various distance to form plot of resistance versus distance between electrode, then uses the slope to find resistivity of the specimen.

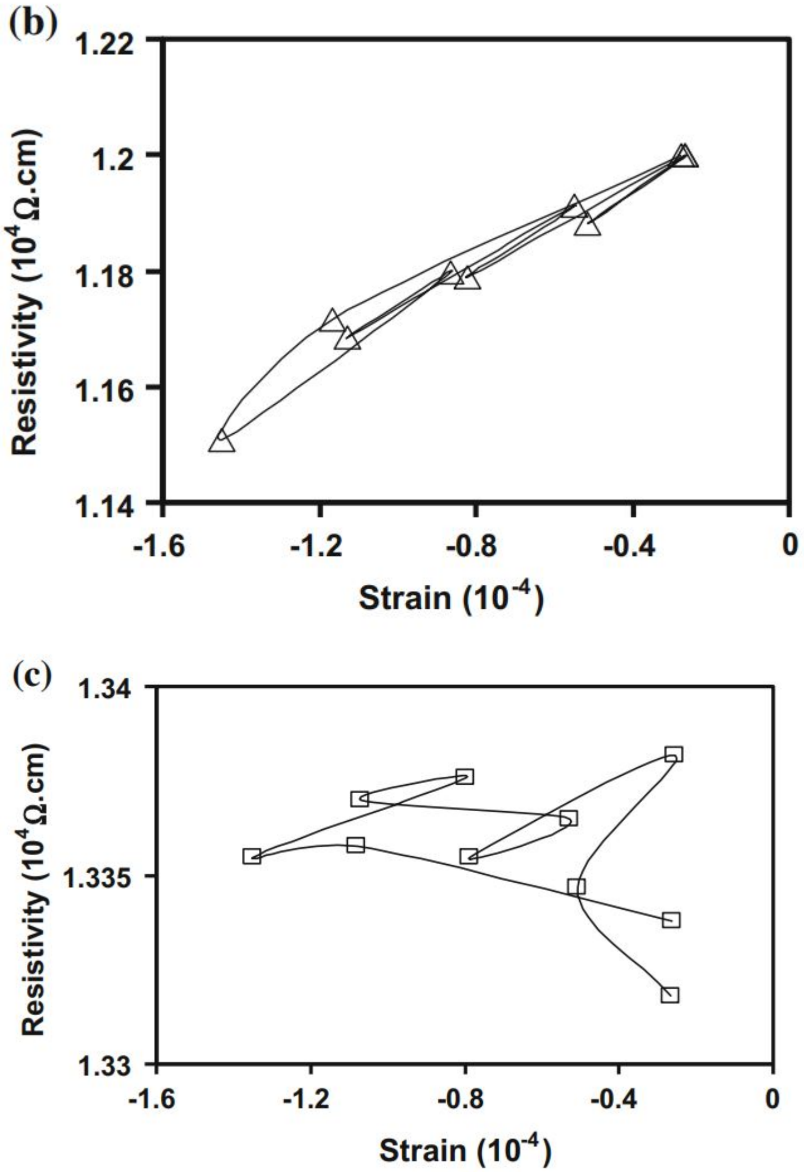

Figure 3.5. Effect of dynamic compressive loading on resistance of short carbon fiber cement-matrix composite. (b) Shows resistivity measured with four-probe method versus peak strain of the cycle, and (c) shows resistivity measured with two-probe method versus peak strain of the cycle. Both data points are connected in chronological order [123].

The two-point probe method is suitable for collecting resistivity data from high resistance specimens (assuming the resistance of the specimen is much less than the input impedance of the measurement device). The resistivity, ρ, is calculated from the drop in voltage, V, and current, I, passing through the specimen. The dimension parameters, A and L_s, refer to the cross-sectional area and the length of the specimens. A diagram of two-probe technique is shown in Figure 3.6.

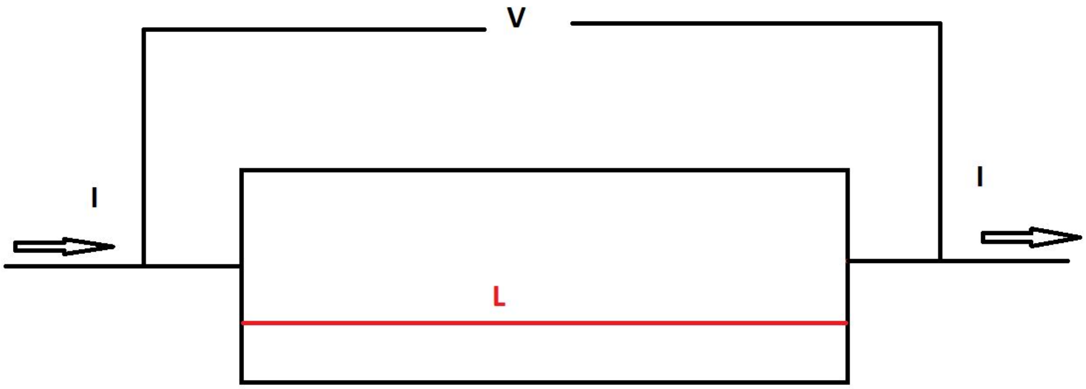

Figure 3.6. Measuring electrical resistivity using two probe method.

Using this method (and assuming the specimen is prismatic), the resistivity can be calculated using equation 3.1 shown below.

$$\rho = \frac{VA}{L_s I} \tag{3.1}$$

The other method, the four-probe technique, is also commonly used in many studies [126] [127]. The advantage of four-point probe method over two-point probe method is its elimination of inaccuracy due to contact impedance, which can be a problem for highly conductive materials. This method lets current flows through outer contacts near the edges of the specimen and measures the potential difference across inner contacts. However, possibility of measurement errors are still present due to the production of heat in the electrodes contact. Therefore, the four-probe technique is preferable to use in low resistance measurements. The technique measures the potential drop across two probes, and instead of using the length of the specimen as measurement distance, the length of gap, D, between the two probes is taken as sample length, as shown in Figure 3.7.

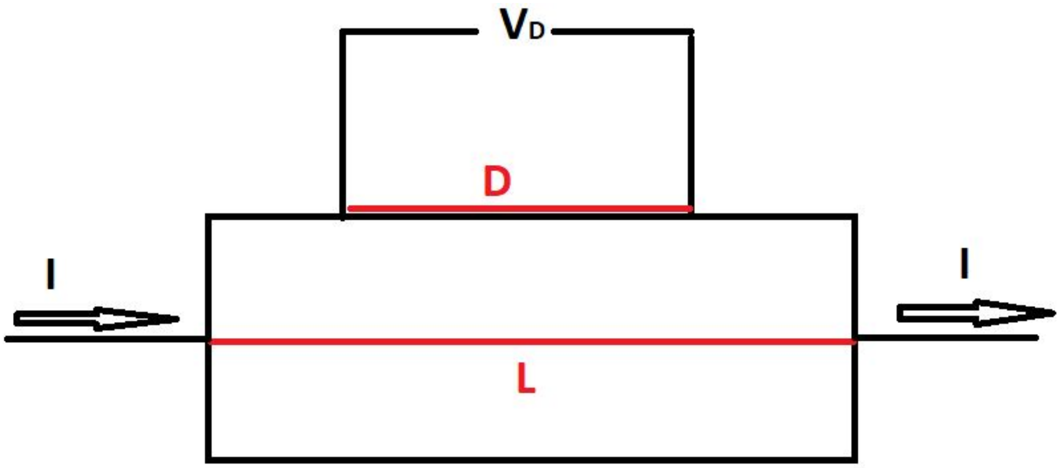

Figure 3.7. Measuring electrical resistivity using four probe method.

The arrows and the line segment below them indicate the current flow direction. The resistivity can be calculated by equation 3.2.

$$\rho = \frac{V_D A}{DI} \tag{3.2}$$

The four-probe method overcomes errors due to DC offsets in the instrument by subtraction. However, other sources, such as self-induced voltage offsets within circuits can cause errors in measurements. Studies that proposed improvements to eliminate possible noise when applying four-point probe method in DC measurements on self-sensing material exist. As an example. Downey et al. [126] presented a biphasic DC measurement approach that sourced a periodic measure/discharge signal in the form of square waves from a signal generator, provided a constant and repeatable measurement over time. Another work from the same author, Downey et al. [128] also discussed the presented biphasic DC measurement approach can remove the electrical drift that commonly attributed to material polarization.

3.1.3 AC Properties

AC-based self-sensing has important potential advantages over DC techniques, as AC carries more information, can be more sensitive [5] [49] [50], and has lower power requirements at high frequencies due to exponential increase in AC conductivity [51]. However, much less work exists in the area of AC transport in nanocomposites. Thus, as a primer for the remainder of this thesis, this section provides a brief summary of nomenclature used to describe macroscale AC transport.

General AC electrical properties of a material are described by the electrical admittivity, ξ, in a relation as shown in equation 3.3. In this equation, σ_{DC} denotes the DC conductivity (as described in the previous section), ω is the angular frequency, ϵ is the permittivity, and j is the imaginary unit shown in equation 3.4. Notice that the permittivity contains real and imaginary parts, as shown in equation 3.5.

$$\xi = \sigma_{DC} + \mathrm{j}\omega\epsilon \tag{3.3}$$

$$\mathrm{j} = \sqrt{-1} \tag{3.4}$$

$$\epsilon = \epsilon^{'} - \mathrm{j}\epsilon^{''} \tag{3.5}$$

Combining the relations shown in equation 3.3 and 3.5, the admittivity relations can be rephrased as shown in equation 3.6, and the AC conductivity, σ_{AC}, can be extracted from the parenthetical term in equation 3.6, as shown in equation 3.7.

$$\xi = \left(\sigma_{DC} + \omega\epsilon^{''}\right) + \mathrm{j}\omega\epsilon^{'} \tag{3.6}$$

$$\sigma_{AC} = \sigma_{DC} + \omega\epsilon^{''} \tag{3.7}$$

A detailed description of AC electrical properties measurement techniques used in this study will be included in the experimental procedure section.

3.2 Electrical Impedance Tomography

3.2.1 Introduction

EIT is an imaging modality for mapping the spatially varying electrical properties of a domain. Because of the piezoresistive effect, EIT has recently seen a surge in attention from the materials community [129] for detecting, localizing, and shaping mechanical effects in self-sensing materials. Later in this thesis, the potential of a new approach to EIT which utilizes frequency-dependent electrical properties is explored. Thus, a brief primer on the theory of EIT, the prevailing approach used by materials practitioners, and the new approach explored in this thesis are presented here. The general formulation of the EIT problem consists of two major parts: the forward problem and the inverse problem. The forward problem involves computationally simulating the diffusion process inside of the domain. The inverse problem then seeks an electrical property distribution of the computational domain that matches the experimental distribution (or change in distribution). There are numerous methods of solving the inverse problem including one-step difference imaging and iterative absolute imaging. The former seeks a change in transport properties to equate two different sets of experimental measurements, whereas the latter endeavors to directly reproduce the actual property distribution at a given time. Due to the ill-posed nature of the EIT inverse problem, difference imaging is most commonly used in practice because errors due to, for example, electrode misplacement, domain shape changes, etc. largely subtract out. Time-difference imaging has been used exclusively by materials practitioners of EIT (i.e., seeking a DC conductivity change correlating a before-damage state to an after-damage state). Biomedical practitioners of EIT, however, make use of frequency-difference methods (i.e., seeking an admittivity change correlating voltage measurements collected at two different frequencies). This is typically a necessity in biomedical EIT since a ‘healthy’ baseline for time-difference imaging does not exist. All EIT code used in the problem formulation in this study was developed in-house using MATLAB.

3.2.2 Forward Problem

The forward problem is described first. The formulation presented below assumes steady-state AC transport. Hence, it is written in terms of the electrical admittivity, ξ. For DC transport, the admittivity can simply be replaced by the DC conductivity. It is also assumed that the AC frequency is small enough that inductive effects can be ignored. Furthermore, an anisotropic formulation is presented for the sake of generality. For anisotropic transport, the admittivity is a symmetric second-order tensor. Isotropic transport can be recovered by letting $\xi_{\mathrm{ij}} = \xi\delta_{\mathrm{ij}}$, where δ_{ij} is the Kronecker-delta. With these clarifications in mind, considering steady-state diffusion in the absence of internal sources, current and domain potential are related by the Laplace's equation shown below in equation 3.8

$$\frac{\partial}{\partial x_{\mathrm{i}}}\xi_{\mathrm{ij}}\frac{\partial u}{\partial x_{\mathrm{j}}} = 0 \tag{3.8}$$

where ξ_{ij} is the (potentially) anisotropic admittivity and u is the domain potential. For AC transport, $u \in \mathbb{C}$, thereby encoding phase information into the potential field. For DC, u is strictly real. The repeated indices imply summation over the dimension of the domain. Laplace's equation is subject to the complete electrode model boundary conditions as shown in equation 3.9

$$\xi_{\mathrm{ij}}\frac{\partial}{\partial x_{\mathrm{i}}}n_{\mathrm{j}} = \frac{1}{z_l}(V_l - u) \tag{3.9}$$

where n_{j} denotes an outward point normal vector, z_l is the contact impedance of the lth electrode, and V_l denotes the voltage of the lth electrode. Note that repeated l subscripts do not imply summation. Enforcing the principle of conservation of charge, the net current through the electrodes is zero, resulting in equation 3.10 shown below

$$\sum_{l=1}^{L}\int_{E_l}\xi_{\mathrm{ij}}\frac{\partial u}{\partial x_{\mathrm{i}}}n_{\mathrm{j}}\,\mathrm{d}E_l = 0 \tag{3.10}$$

where E_l denotes the area of the lth electrode and L is the total number of electrodes. The finite element method is typically used to solve these equations as shown in equation 3.11. In this equation, U is the vector of domain potential, V represents the electrode voltage vector, and I is the injected current vector.

$$\begin{bmatrix} A_M + A_Z & A_W \\ A_W^T & A_D \end{bmatrix} \begin{bmatrix} U \\ V \end{bmatrix} = \begin{bmatrix} 0 \\ I \end{bmatrix} \tag{3.11}$$

The formation of the matrices A_M, A_Z, A_W, and A_D are shown in the following equations (3.12, 3.13, 3.14, 3.15) correspondingly:

$$A^{\mathrm{e}}_{M\mathrm{ij}} = \int_{\Omega_\mathrm{e}} \frac{\partial w_\mathrm{i}}{\partial x_k} \xi_{kl} \frac{\partial w_\mathrm{j}}{\partial x_l} \, \mathrm{d}\Omega_\mathrm{e} \tag{3.12}$$

$$A_{Z\mathrm{ij}} = \sum_{l=1}^{L} \int_{E_l} \frac{1}{z_l} w_\mathrm{i} w_\mathrm{j} \, \mathrm{d}E_l \tag{3.13}$$

$$A_{W\mathrm{ij}} = - \int_{E_l} \frac{1}{z_l} w_\mathrm{i} \, \mathrm{d}E_l \tag{3.14}$$

$$A_D = \mathrm{diag}\left(\frac{1}{z_l}\right) \tag{3.15}$$

Specifically, $A^{\mathrm{e}}_{M\mathrm{ij}}$ denotes the local diffusion stiffness matrix of the eth element. The A_Z, A_W, and A_D matrices account for the additional degrees of freedom introduced by the electrode voltages and the contact impedance between the electrodes and the domain. w_i is the ith finite element interpolation function; linear triangular elements were used in this work. For additional details, interested readers are directed to reference [130].

3.2.3 Inverse Problem

The inverse problem is the process of recovering the distribution of electrical conductivity (in DC) or admittivity (in AC). Methods of solving the EIT inverse problem have been researched for decades. Popular methods include Gauss-Newton minimization [131] [132], back projection [133], total variation regularization [134], and Graz consensus Reconstruction EIT (GREIT) [135]. Herein, a direct extension of a one-step minimization as a difference imaging method was developed and employed. Therefore, despite the existence of other minimization methods for the fdEIT inverse problem, only the formulation of general one-step minimization will be discussed. Several possible alternative algorithms are noted, however, such as the weighted difference method [136] and a constrained least-squares method [137].

Next, a general one-step difference formulation is presented. As will be specified throughout the presentation of this approach, this presentation can be specialized to either time-difference or frequency-difference imaging. The inverse problem begins by defining a voltage difference vector as shown below in equation 3.16.

$$\boldsymbol{V}_d = \boldsymbol{V}_2 - \boldsymbol{V}_1 \tag{3.16}$$

Above, let $\boldsymbol{V}_d$ be the difference between two experimentally collected voltage vectors, $\boldsymbol{V}_2$ and $\boldsymbol{V}_1$, collected at the boundary of the domain and corresponding to two different states. In time-difference imaging, these states correspond to two different times (i.e., after damage at time t_2 and before damage at time t_1). In frequency-difference imaging, these states correspond to two different interrogation frequencies (i.e., $\boldsymbol{V}_2$ collected while the specimen is subject to AC excitation of ω_2 and $\boldsymbol{V}_1$ collected while the specimen is subject to AC excitation of ω_1 such that $\omega_2 > \omega_1$). The inverse problem seeks to replicate this difference using the forward problem as shown in equation 3.17.

$$\boldsymbol{W} = \boldsymbol{F}(\xi_1 + \delta\xi) - \boldsymbol{F}(\xi_1) \tag{3.17}$$

Here, $\boldsymbol{F}$ is a vector of electrode voltages predicted by the forward problem, ξ_1 is the admittivity distribution in state one, and $\delta\xi$ is the change in admittivity between states one and two such that $\xi_2 = \xi_1 + \delta\xi$. To clarify, for fdEIT, these states again correspond to frequencies ω_1 and ω_2. For time-difference imaging, the admittivity would be replaced by the DC conductivity distribution. Else, the approach is the same. This clarification aside, the goal of the inverse problem is to find $\delta\xi$. To do this, a minimization problem can be formulated as shown in equation 3.18 below.

$$\delta\xi^* = \arg\min_{\delta\xi} \left(\|\boldsymbol{W}(\delta\xi) - \boldsymbol{V}_d\|_2^2 \right) \tag{3.18}$$

To solve this, $\boldsymbol{W}(\delta\xi)$ is linearized via a truncated Taylor series expansion centered about $\delta\xi$ as $\boldsymbol{W} \approx \boldsymbol{J}\delta\boldsymbol{\xi}$ where $\boldsymbol{J} = \partial\boldsymbol{F}(\boldsymbol{\xi})/\partial\boldsymbol{\xi}$ is known as the sensitivity matrix. Again for time-difference imaging, $\boldsymbol{J}$ can be analogously be formed by substituting DC conductivity for admittivity (hence, $\boldsymbol{J}$ is strictly real for DC imaging). For AC problems, $\boldsymbol{J}$ is a complex-valued matrix. Note also that the admittivity distribution has been boldfaced in anticipation of discretization by the finite element method in the forward problem. Substituting this approximation for $\boldsymbol{W}$ back into equation 3.18, the following form is obtained.

$$\delta\boldsymbol{\xi}^* = \arg\min_{\delta\xi} \left(\|\boldsymbol{J}\delta\boldsymbol{\xi} - \boldsymbol{V}_d\|_2^2 + \alpha \|\boldsymbol{R}(\delta\boldsymbol{\xi})\|_2^2 \right) \tag{3.19}$$

A regularization term, $\boldsymbol{R}(\delta\boldsymbol{\xi})$, has been added to the above minimization due to the ill-posed nature of the EIT inverse problem. α is a scalar hyperparameter used to control the influence of the regularization. In this work, the discrete Laplace operator is used for regularization due to its ability to filter out highly oscillatory solutions. Lastly, an explicit solution for the minimization-satisfying solution, $\delta\boldsymbol{\xi}^*$, can be written as shown in equation 3.20 below. Again, for the fdEIT problem, the solution vector will be complex. For tdEIT, it will be strictly real.

$$\delta\boldsymbol{\xi}^* = \left(\boldsymbol{J}^T\boldsymbol{J} + \alpha^2\boldsymbol{R}^T\boldsymbol{R} \right)^{-1} \boldsymbol{J}^T\boldsymbol{V}_d \tag{3.20}$$

4. EXPERIMENTAL PROCEDURE

4.1 Introduction

The following sections will present the experimental procedures used in this work. These sections include manufacturing processes for the materials studied, descriptions of how the specimens were damaged, and descriptions of how electrical measurements were taken. CNF-modified glass fiber/epoxy laminates were used as a representative self-sensing material in this study. This particular material system was used due to its manufacturing method being well documented and its electrical properties being well studied through prior work in this research group [138] [99] [139]. Two types of the CNF-modified glass fiber/epoxy specimens were produced – square specimens for DC/AC electrical properties measurements and rectangular specimens for artificial damage testing. Both specimens were produced using the same procedures.

4.2 Specimen Manufacturing

4.2.1 Materials Used

CNF-modified glass fiber specimens were manufactured in two major steps: 1) the preparation of CNF-modified epoxy and 2) the infusion of this epoxy into a glass fiber laminate. For the first part, liquid epoxy resin was modified with Pyrograf III PR 24-XT-HHT CNFs. These were dispersed in Fibre Glast System 2000 epoxy resin with the aid of Triton X-100 surfactant, acetone, and BYK-A 501 air release agent. Per the manufacturer's description, these CNFs were treated at 3000 ℃ to convert the nanofiber to a fully graphitized form and resulted in highly conductive CNFs with low levels of iron content. The average fiber diameter of these CNFs is 0.1 μm, as-produced lengths ranging from 50 to 200 μm, and the surface area is around 41 m^2/g [140]. In the second part of the manufacturing process, the CNF-modified epoxy was used to produce glass fiber laminates. Glass fiber fabrics were purchased from Fibre Glast. These fabrics included uniaxial and biaxial glass fiber fabrics.

4.2.2 Manufacturing Procedure

The experimental procedure began with placing appropriate weights of epoxy resin and CNFs into a glass beaker. Surfactant and acetone were added after. The weight ratio between the surfactant and the CNFs was 0.76:1 and the epoxy resin to acetone volume ratio was 2:1. Adding surfactant to the mixture promotes effective dispersion of CNF, and acetone improves the fluidity of the mixture. The mixture was then mixed for five minutes in a Thinky AR-100 planetary centrifuge and then sonicated for five hours in a Crest Powersonic CP200HT bath sonicator. According to the specification of the manufacturer, the sonicator operates at an average power of 35 W and a frequency of 45 kHz. After the mixture was done sonicating, it was placed on a hot plate magnetic stirrer and stirred for 24 hours at 600 rpm and 60 ℃ to evaporate the acetone. The weight of the mixture was measured before and after the stirring process to ensure complete evaporation of the acetone. After the stirring was completed, the mixture was placed into a flat glass basin filled with a mixture of ice and water to cool it down and prevent premature curing. Once the mixture was cooled down, proper weights of air release agent and curing agent were added. The weight ratio of air release agent to epoxy resin was 0.003:1, and the hardener to epoxy resin weight ratio of 0.27:1 was used. The mixture was then stirred gently for five minutes by hand and degassed in a vacuum chamber for 30 minutes at room temperature. While the mixture was degassed, an aluminum tool was cleaned with acetone and Kim wipes. Then, sealant tape was applied to the perimeter of the tool, and three coats of mold release were applied to the tool at five-minute intervals. The release film was placed onto the tool, and a peel ply was placed on top of the release film. After the mixture was done degassing, six layers of uniaxial glass fabric were stacked in a $[0/90]_6$ stacking sequence. A paint brush and squeegee were used to impregnate each layer of the glass fiber mats with the CNF-modified epoxy mixture. The bagged tool was then vacuumed to find potential unsealed areas, and once the seal was secured, the tool was placed in an oven and cured for five hours at 60 ℃.

For artificial damage testing, five plates were made in an identical fashion. These plates were made with a combination of 0.75 wt.% CNF and uniaxial glass fiber fabric. Each of the plates was cut into three 1.5” × 4.5” rectangular specimens using a wet ceramic tile saw. An additional five plates were made with identical manufacturing procedures with different weight fractions (0.25, 0.35, 0.5, 1.0, and 1.5 wt.% CNFs) with biaxial glass fiber fabric. These plates were cut to 1" × 1" square specimens to measure average in-plane AC conductivity for each weight fraction.

4.3 Specimen Preparation

4.3.1 Electrical Measurements

Basic transport properties were measured for a wide range CNF weight fractions in order to develop basic insight into how CNF concentration affects AC transport. Tested weight fractions include 0.25, 0.35, 0.5, 1.0, and 1.5 wt.% made with biaxial glass fiber. These measurements were done in order to inform later fdEIT simulations. For each weight fraction, a total of 25 1" squares were cut from larger plates as shown in Figure 4.1. Sides of the specimens were cleaned thoroughly with acetone. Two opposite sides were coated with silver paint and copper tape to take in-plane measurements. Measurements of DC conductivity were also collected in order to determine the percolation threshold for this material system. This was done by first measuring the dimensions (length, width, and height) of each specimen with a caliper. A Keysight U1241C hand-held multimeter (DMM) was then used to take resistance measurements. The DC conductivity was then calculated on each specimen via equation 4.1 as shown below:

$$\sigma_{DC} = \frac{L_s}{RA} \tag{4.1}$$

Here, σ_{DC} is the DC conductivity, L_s is the length of the specimens along the measurement direction, R is the measured resistance, and A is the cross-sectional area perpendicular to the measurement direction. The DC conductivity was plotted against the weight fraction as shown in Figure 4.2.

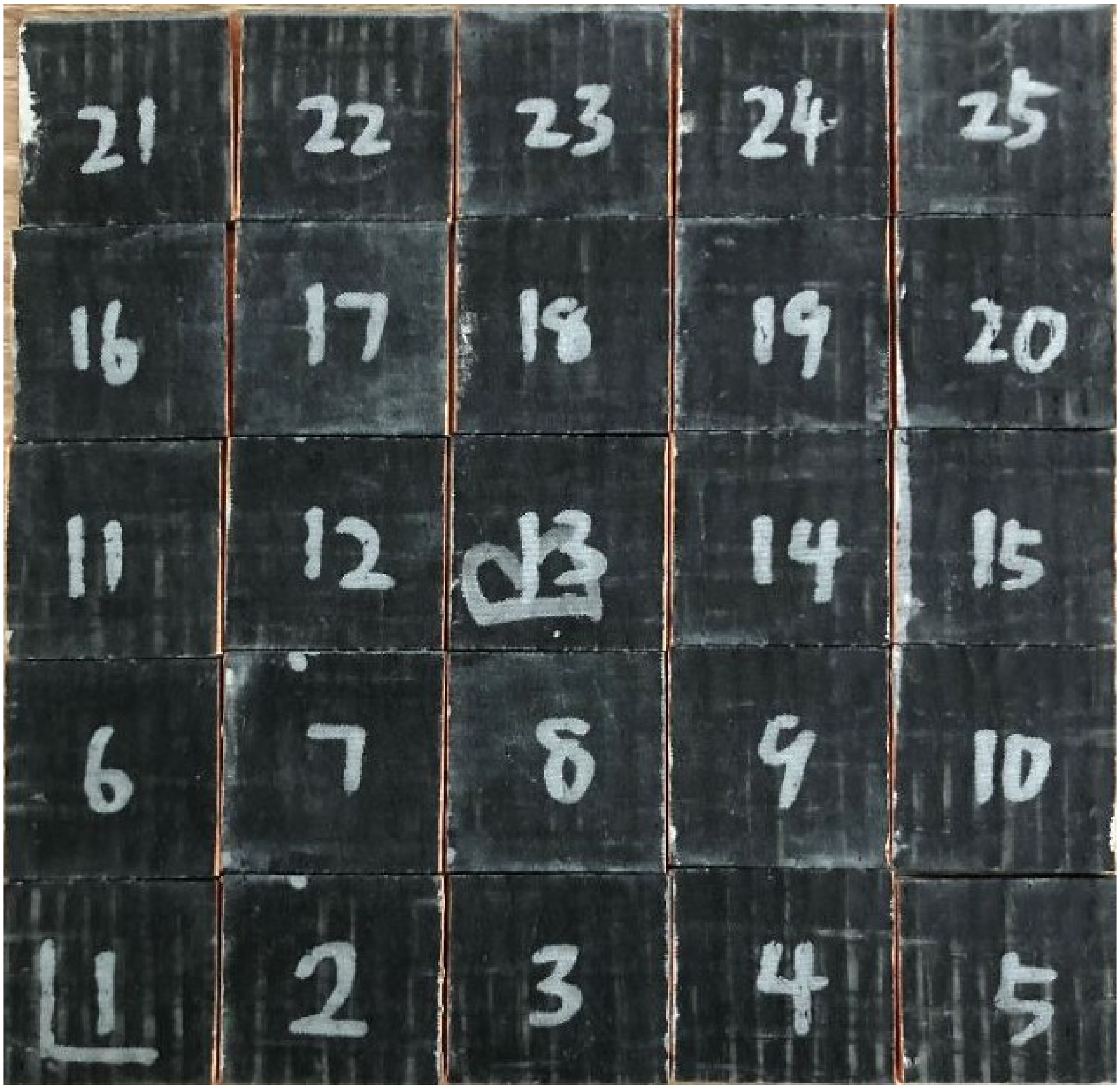

Figure 4.1. 25 0.5 wt.% CNF-modified glass fiber/epoxy 1” × 1” inch square specimens used in AC conductivity measurements.

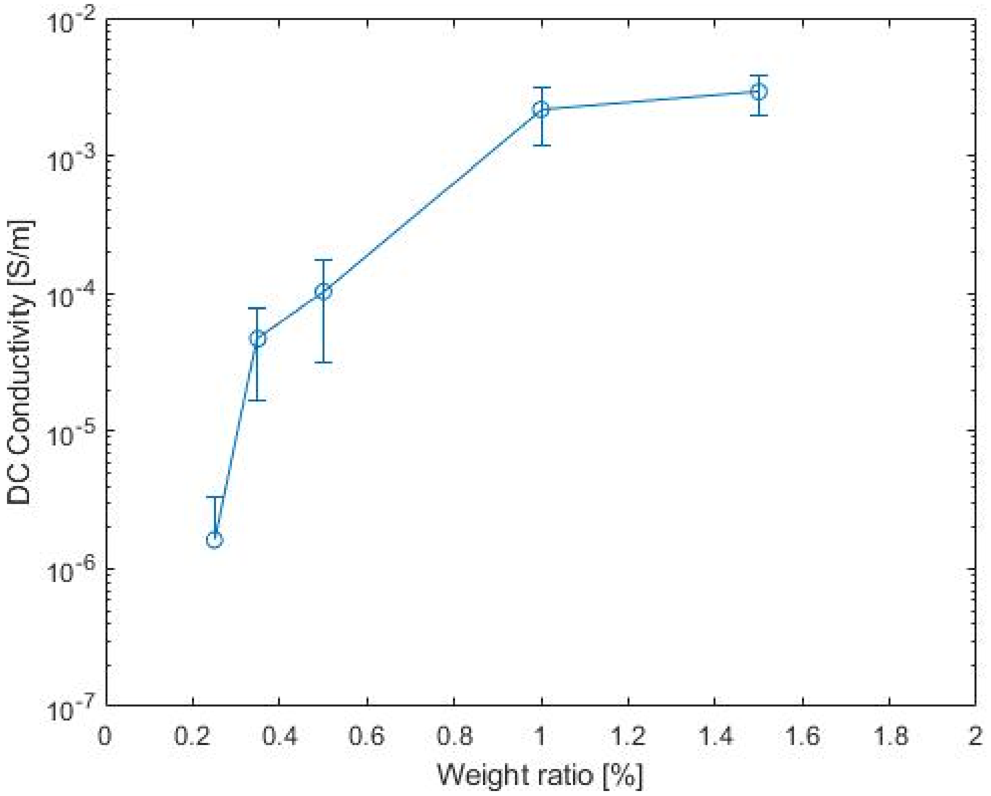

Figure 4.2. DC conductivity for 0.25, 0.35, 0.5, 1.0, 1.5 wt.% CNF-modified biaxial glass fiber/epoxy.

4.3.2 CNF/Epoxy Glass Fiber AC Electrical Properties

After DC electrical measurements were taken, AC measurements were collected to record impedance magnitude, $|Z|$, and phase angle, θ, over a frequency range of 100 Hz to 10 MHz using a Keysight E4990A impedance analyzer. To calculate the AC conductivity, the real part of the impedance was first calculated. In AC, the impedance is a complex-valued quantity, $Z \in \mathbb{C}$, and written as having a real and imaginary part as shown in equation 4.2

$$Z = Z^{'} + \mathrm{j}Z^{''} \tag{4.2}$$

$Z^{'}$ is the real part and $Z^{''}$ is the imaginary part of the impedance. To calculate the real part and the imaginary part of the impedance using the measured impedance magnitude and phase angle, the following equations are used:

$$Z^{'} = |Z| \cos\theta \tag{4.3}$$

$$Z^{''} = |Z| \sin\theta \tag{4.4}$$

The AC conductivity can be calculated as from the real part of the impedance and the specimen dimensions as shown below:

$$\sigma_{AC} = \frac{L_s}{Z^{'}A} \tag{4.5}$$

Experimentally measured AC conductivity values are shown in Figure 4.3. The curve for 0.25 wt.% CNF specimen (Figure 4.3 (a)) was separated to show other weight fraction curves (Figure 4.3 (b)) more clearly. As shown in the Figure 4.3, two distinct regimes are observed: one is the flat portion of the σ_{AC} curve which indicates the frequency independent behavior, referred to as the DC region. The DC region exhibits near constant impedance response, based on the fact that electrical transport through the filler formed conductive network is dominated by filler and inter-filler resistance. The other regime is the exponential increase part of the σ_{AC} curve and indicates the frequency-dependent behavior. The exponential increase of σ_{AC} with interrogation frequency shows the results of filler and inter-filler AC effects, such as formulation of micro-capacitors in the inter-filler regions, or interfacial polarization between the conductive fillers and the non-conductive matrix. Such effects dominate the net electrical transport properties, creating frequency-dependent conductivity change behavior. There is also significant variability in the 0.25 wt.% AC conductivity data. As discussed in other works [101], this is a consequence of poor network connectivity and limited redundancy in the CNF network, which gives rise to highly variable transport.

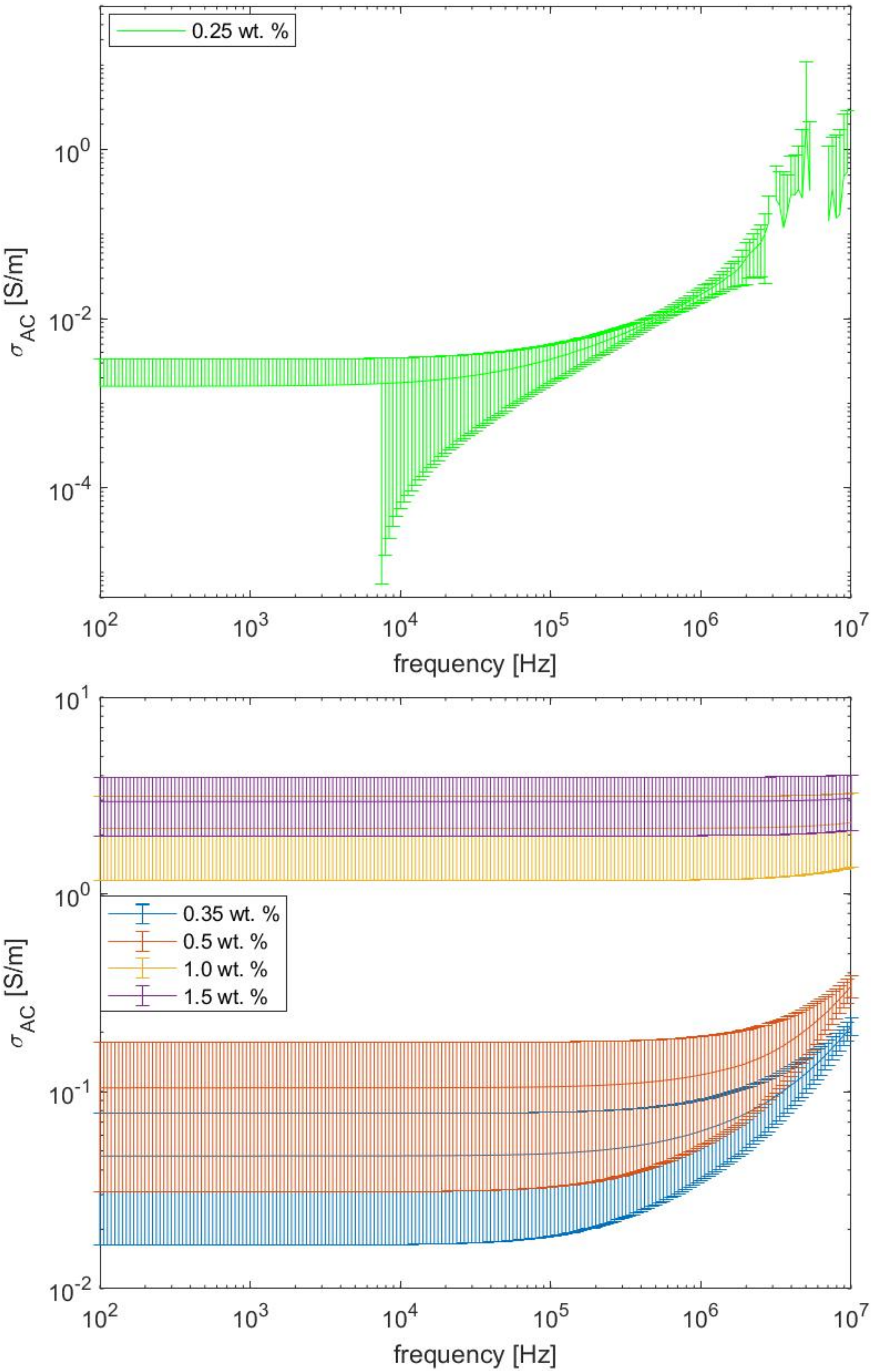

Figure 4.3. AC conductivity curves with error bounds for different weight fraction of CNF-modified biaxial glass fiber/epoxy (a) 0.25 wt.% and (b) 0.35, 0.5, 1.0, 1.5 wt.%.

4.3.3 Artificial Damage Specimens

Two electrodes were attached on the same surface of the artificial damage specimens in the form of 1.5" × 0.5" rectangles each located 0.25" from the edges of the specimen, as shown in the Figure 4.4. The location of the electrodes was chosen such that measurements could be taken along the longitudinal axis of the specimens. The electrodes were formed by first applying TED PELLA fast drying silver paint and then covering the silver paint with 3M 0.5"-wide copper conductive tape. Five types of artificial damages were induced onto these specimens, and three specimens were tested for each damage type. Therefore, in total, 15 specimens were used in this set of experiments. The artificial damages include varying the number of holes, size of holes, number of notches, size of notches, and number of impacts. These are further described below:

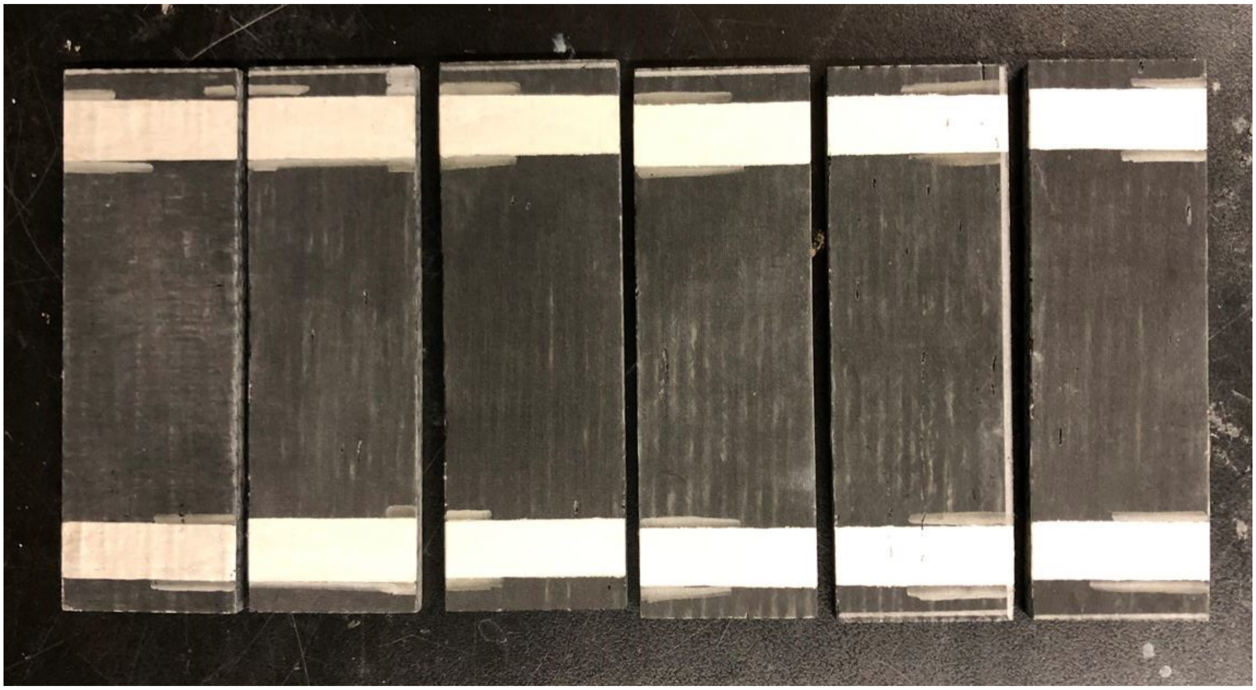

Figure 4.4. 1.5" × 4.5" rectangular specimens for artificial damage experiment paint with quick dried silver paint to form electrodes.

- Number of holes test: The specimens in this category were drilled with three through-holes with diameters of 3/16". The locations of the centers of the holes were at the center line along the longitudinal direction of the specimens, 1.25", 2.25", and 3.25" away from the edge, as shown in Figure 4.5. The locations and diameters were chosen to ensure the holes were large enough to have distinguishable change in impedance measurements. Measurements were taken before damage took place and after each hole was drilled.

- Size of hole test: A through-hole was located at the center of each specimen, 2.25” from the longitudinal edge and 0.75” from the lateral edge, as shown in Figure 4.5. The first hole was drilled with a diameter of 3/16”, then it was enlarged to 1/4”, and lastly enlarged to 5/16”. Measurements were again taken before damage took place and after new hole size.

- Number of notches test: A total of three notches were cut by a tile saw using a DW4764 10” XP4 Porcelain tile blade on the same longitudinal side of the specimens. According to the manufacturer, the tile blade has a thickness of 1/16” [141]. The locations of the center line of notches were the same as the longitudinal locations of the center of the holes from number of holes testing, and the length of the notches was chosen to be 0.25”, as shown in Figure 4.6. Measurements were taken before the first notch was cut and after each notch was added.

- Size of notch test: A single notch was cut into the specimen. The notch was cut at the center mid-length of the specimen and extended further inward with each new damage state. Similar to size of hole testing, electrical measurements were taken once before damage, then again after a 0.25”-long cut was made, once again after the notch was cut to 0.5”, and again after the notch size was increased to 0.75”, as shown in Figure 4.6.

- Number of impact test: An Instron impact machine was used to induce impact damage to the specimens. The intended impact location is right at the center of the specimens, as shown in Figure 4.7. The energy levels were chosen to be 25 J, 30 J, and 35 J, and the specimens were impacted at each of these energy levels five times. Electrical measurements were taken before the first impact and again after each new impact.

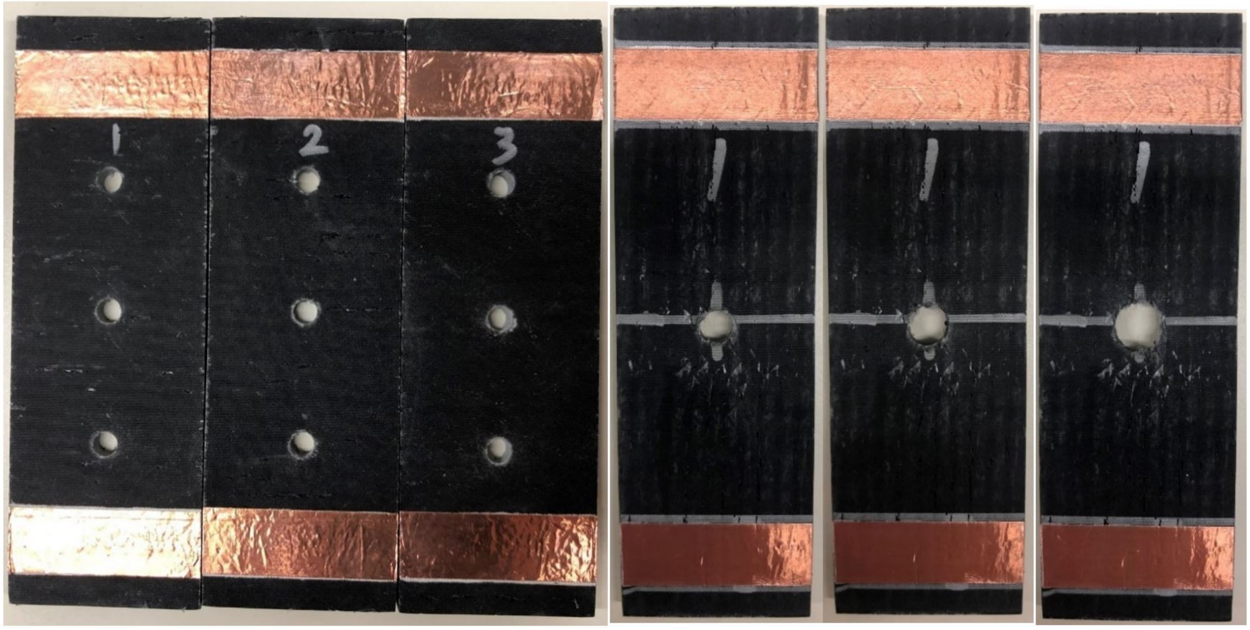

Figure 4.5. Specimens used for numbers of hole testing (left) and increasing hole size testing (right).

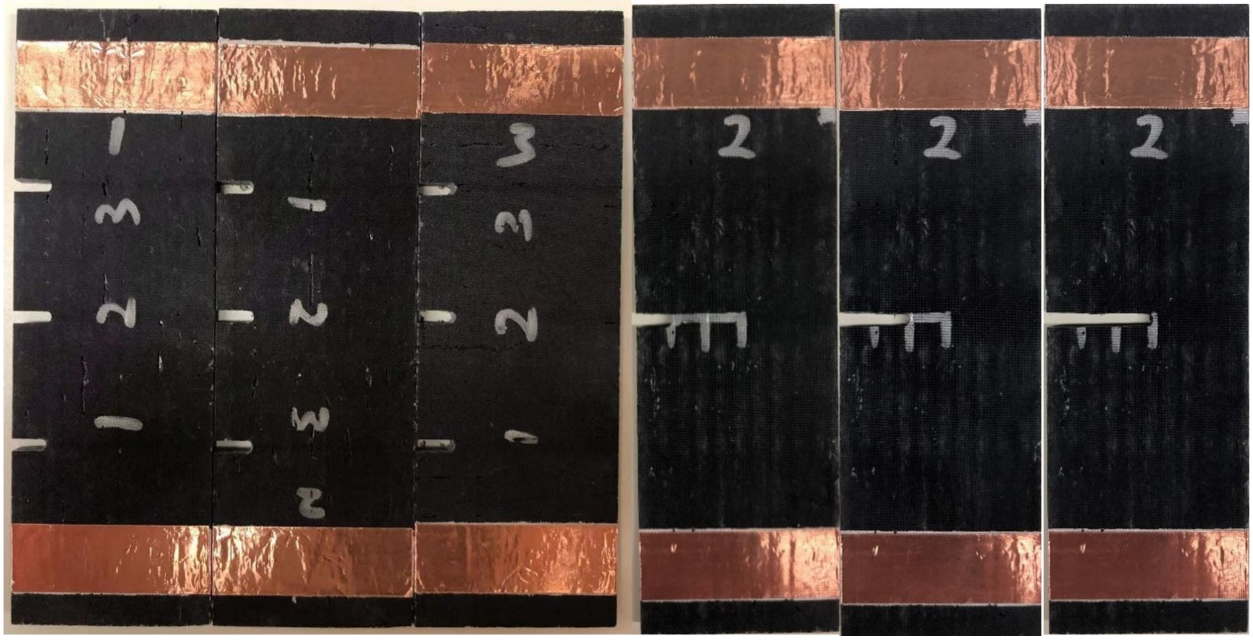

Figure 4.6. Specimens used for number of notches testing (left) and increasing notch size testing (right).

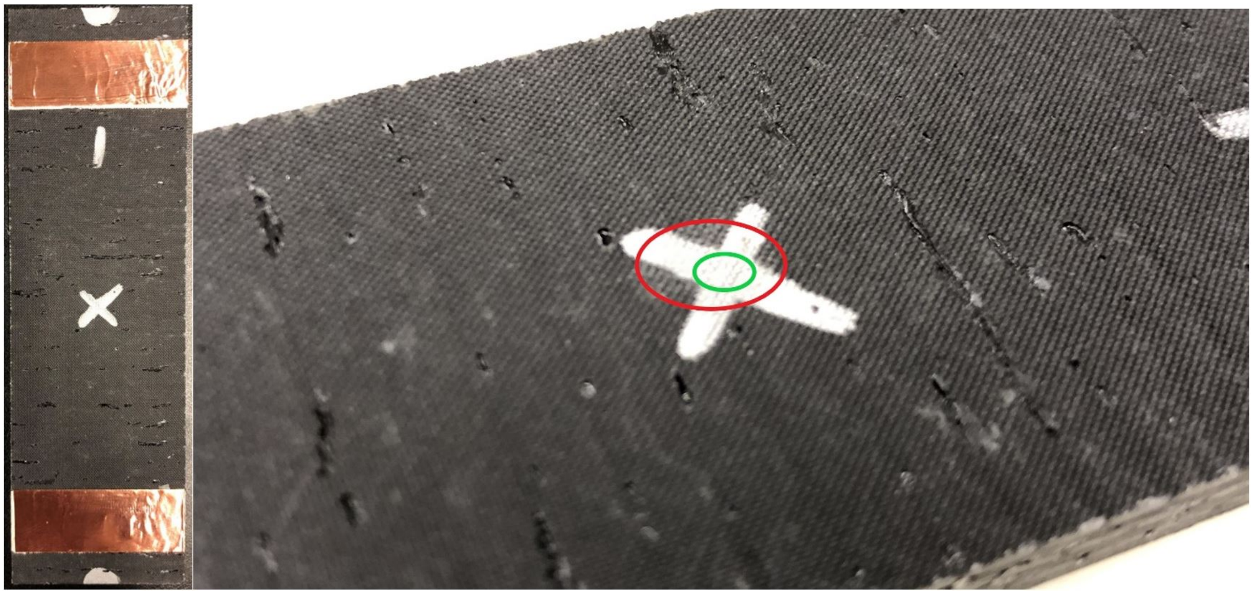

Figure 4.7. One of the specimens used for number of impact test with intended impact location (left) and actual impact location (right). Green circle marks the planned center of impact, and red circle marks the actual impact area.

4.3.4 EIT Simulations

The previously described AC conductivity measurements were used to inform the fdEIT simulations. Based on the measured AC conductivity, it was decided to simulate 0.5 wt.% CNF-modified glass fiber/epoxy. This weight fraction was selected because it displayed fairly consistent transport properties and exhibited a clear change in AC conductivity at relatively modest frequencies (which is a requirement for fdEIT). More specifically, two frequencies ($\omega_1/2\pi = 1$ MHz, $\omega_2/2\pi = 10$ MHz) were selected for this material. As shown in Figure 4.8, an exponential equation was fit to the average of the experimental data and was used to approximate the AC conductivities at these two frequencies. The fitting function was based on the universal dynamic response (UDR) relations or Jonscher's power law [142], where the AC conductivity can be expressed with DC conductivity, σ_{DC}, angular frequency, ω, and fitting constants K and n, as shown in equation 4.6. After fitting the equation to the curve, as shown in equation 4.7, the AC conductivity at the two frequencies were $\sigma_{\omega_1} = 0.12$ S/m and $\sigma_{\omega_2} = 0.34$ S/m.

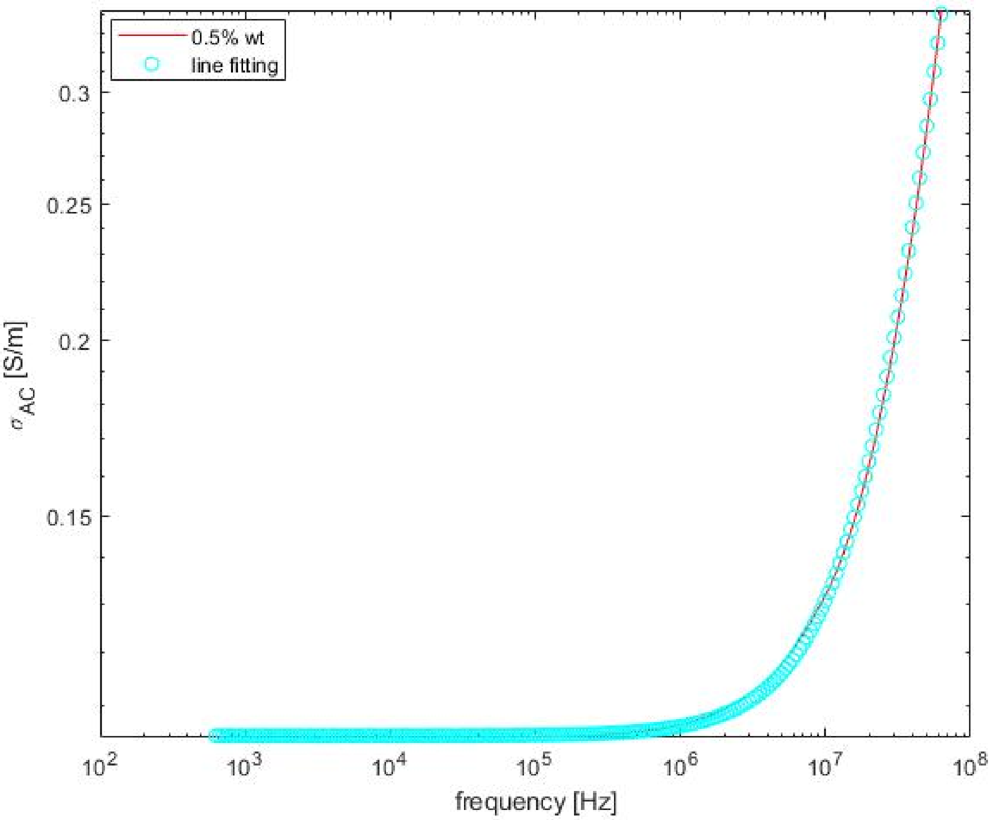

Figure 4.8. The AC conductivity of 0.5 wt.% CNF-modified glass fiber/epoxy was fit to Jonscher's power law in order to estimate the conductivity at the frequencies of interest.

$$\sigma_{AC} = \sigma_{DC} + K\omega^n \tag{4.6}$$

$$\sigma_{AC} = 0.1047 + 1.017 \times 10^{-10}\omega^{1.201} \tag{4.7}$$

The relative permittivity of a polymeric CNF composite was estimated from experimental literature as shown in Figure 4.9 as $\epsilon'_{\omega_1} = 88.59$ and $\epsilon'_{\omega_2} = 52.22$. The actual permittivity is obtained by the product of the relative and the permittivity of free space. Therefore, the result admittivities used to inform the fdEIT simulations were shown as $\xi_{\omega_1} = 0.12 +$

1.11×10^{-4}j S/m and $\xi_{\omega_2} = 0.34 + 6.56 \times 10^{-5}$j S/m. The injection current magnitude in the simulation was set to 1 mA.

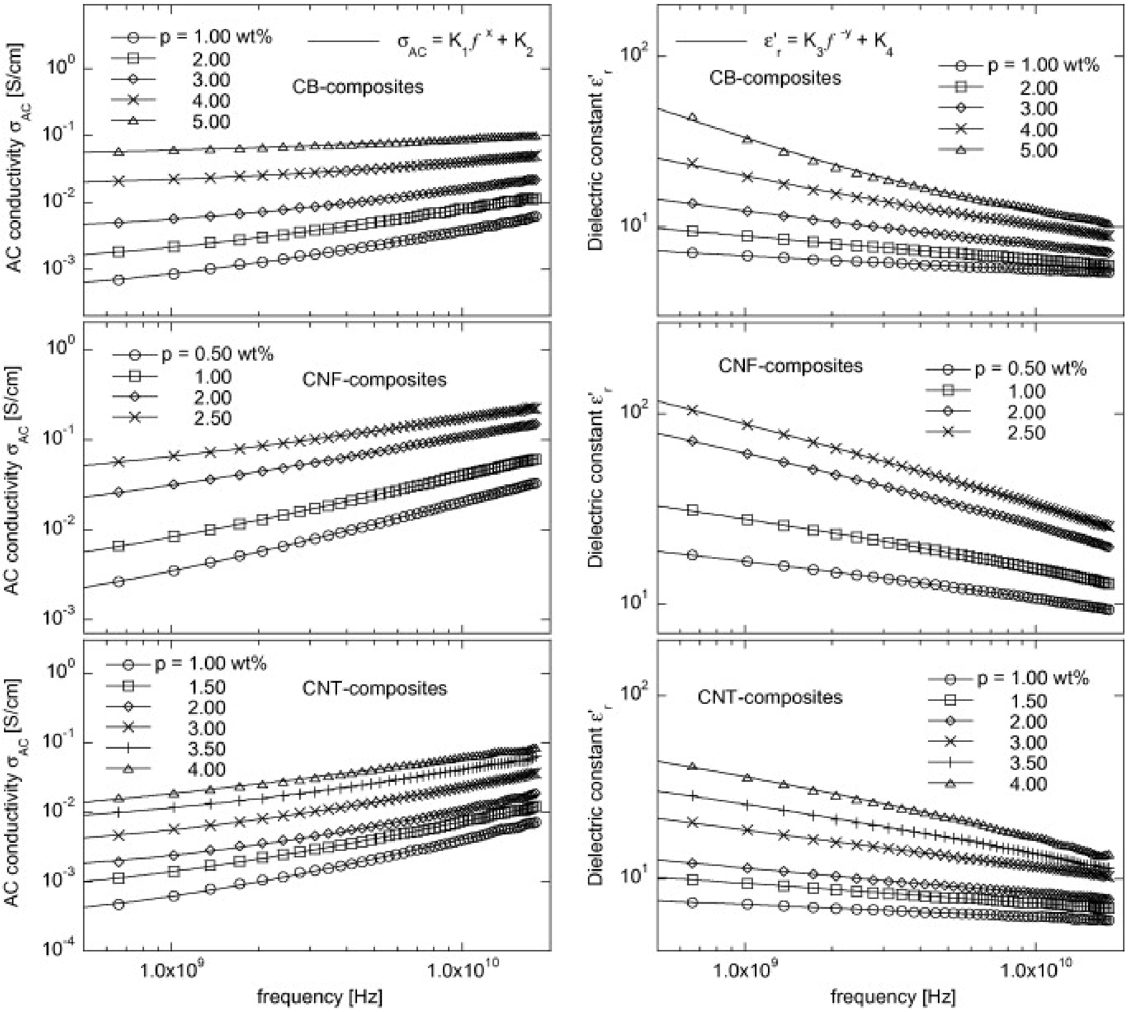

Figure 4.9. AC electric conductivity and dielectric constant of the E-glass fabric/epoxy composite laminates containing carbon nanomaterials [143].

A simple state of damage was simulated on a finite element mesh and the image reconstruction was completed on a different mesh. A planar mesh comprised of linear triangle elements was used, as shown in Figure 4.10. In this study, the forward problem discussed in theory section was used to predict the voltage-current response on the damage mesh, and the fdEIT inverse problem was used to reconstruct the damage state on the other mesh. The size of the computational domain was set to 12.7 cm × 12.7 cm (5” × 5”). The damage was simulated as a square through-hole, centered at $x = 5$ cm, $y = 9$ cm with the size of 1.4 cm ×

1.4 cm (0.5" × 0.5"). The simulation used 16 electrodes with four equally spaced electrodes on each side of the domain. An adjacent injection and measurement scheme, shown in Figure 4.11, was used in this work.

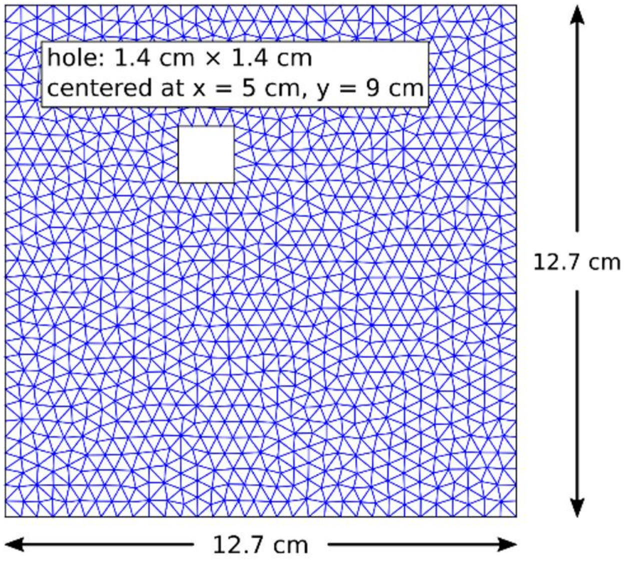

Figure 4.10. The image of the damage simulation mesh used in this study.

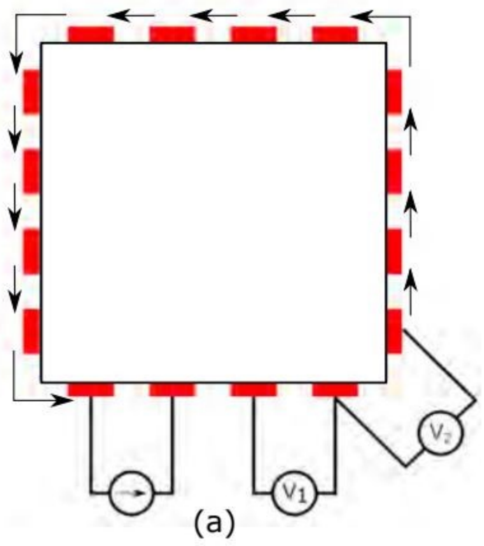

Figure 4.11. Schematic representation of edge-mounted electrodes with adjacent injection pattern. Measurements are taken in counterclockwise direction [144].

5. EXPERIMENTAL RESULTS

5.1 Introduction

The following sections will present the results obtained through this thesis work. The results sections will be organized as follows. First, the raw data is presented. Next, results from damage sensing experiments will be presented corresponding to each type of artificial damage in the order of two through-hole experiments, two notch experiments, and finally, the impact experiments in terms of EIS curves. And third, the simulations results using fdEIT formulations discussed previously will be presented.

5.2 Raw Data

Recall from the procedure section, in order to investigate the effects of artificial damages on the AC transport in the material, AC electrical measurements were taken before and after each damage. These measurements included impedance magnitude and phase angle from 100 Hz up to 10 MHz. The intents of these tests were to develop basic insight into the effect of different representative damage types on AC transport. The raw data from those measurements can be found in the following figures, 5.1-5.5. More specifically, the effect of increasing hole size is shown in Figure 5.1, the effect of increasing number of holes in Figure 5.2, the effect of increasing notch size in Figure 5.3, the effect of increasing number of notches in Figure 5.4, and the effect of increasing number of impacts in Figure 5.5. Recall also that three specimens, named A-C in these plots, were tested per damage type.

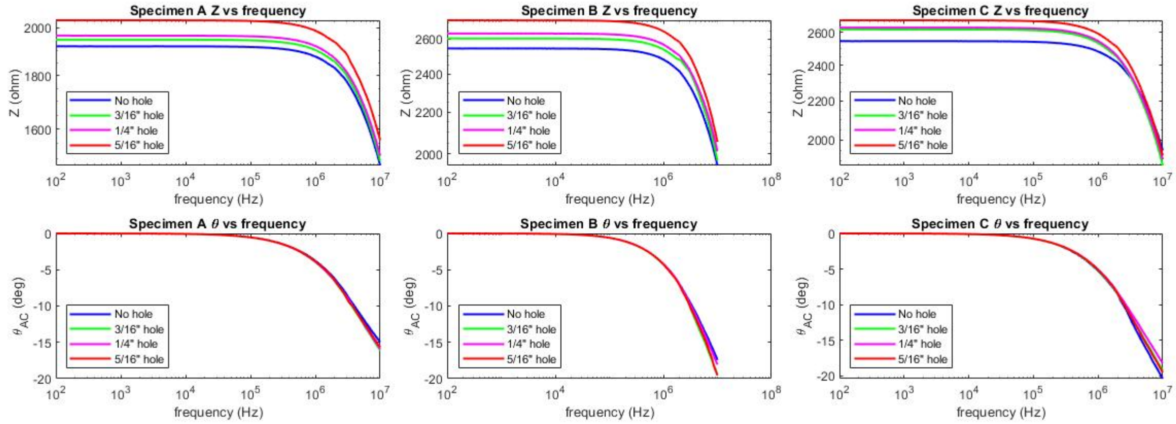

Figure 5.1. Impedance and phase angle data for increasing hole size damages specimens.

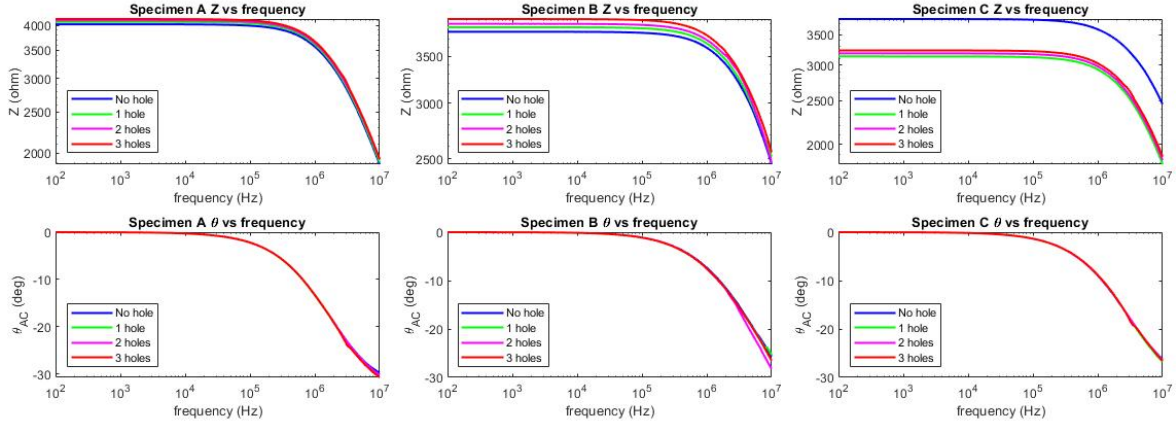

Figure 5.2. Impedance and phase angle data for multiple hole damages specimens.

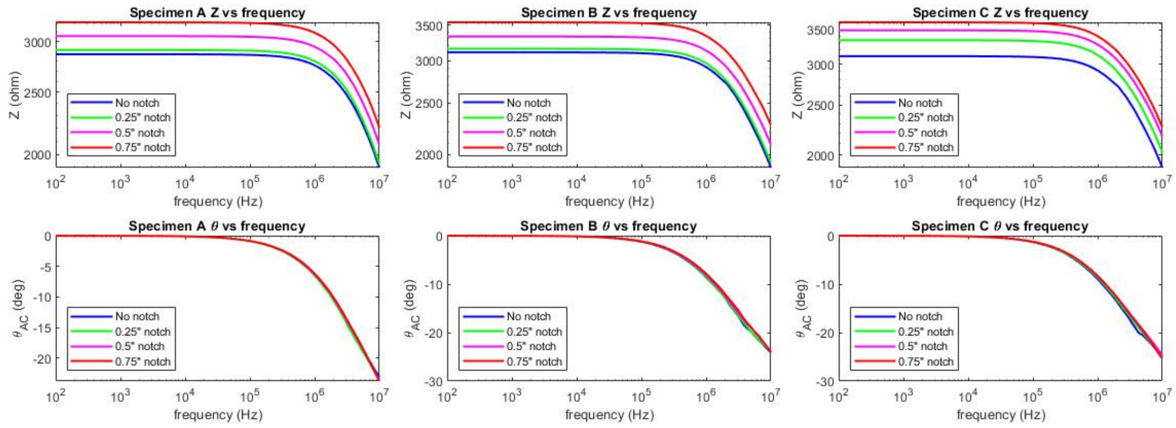

Figure 5.3. Impedance and phase angle data for increasing notch size damages specimens.

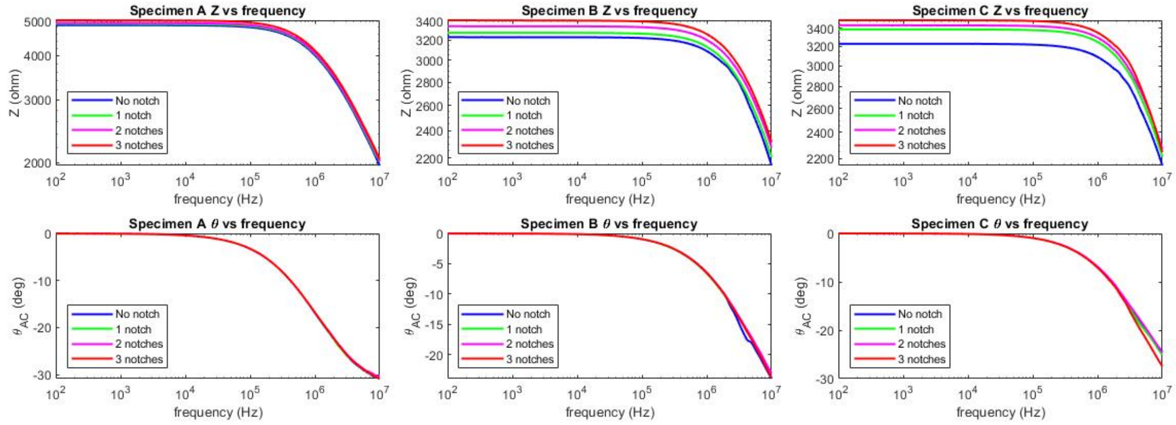

Figure 5.4. Impedance and phase angle data for multiple notch damages specimens.

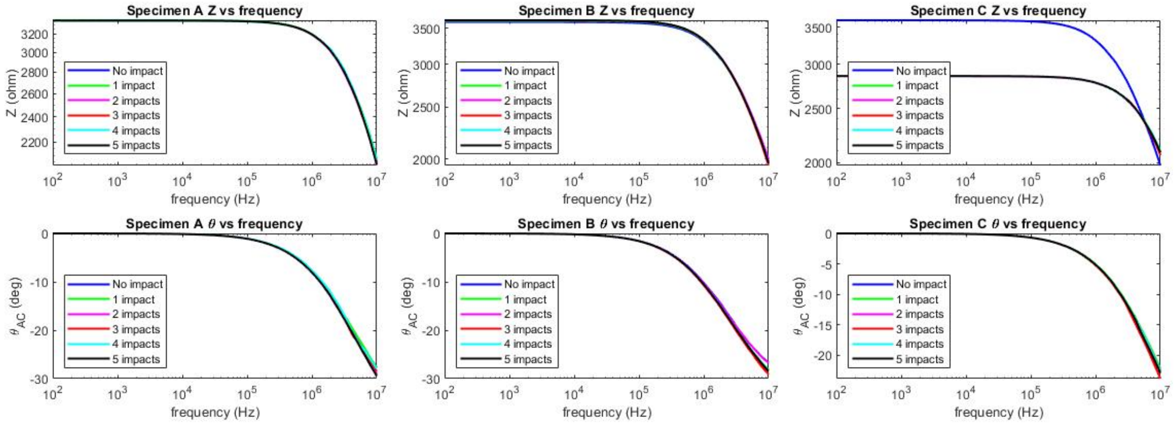

Figure 5.5. Impedance and phase angle data for multiple impact damages specimens.

It can be noticed from the raw data figures that the impedance magnitude for each specimen generally increases as the number or size of the damage increases. However, the phase angle does not show such a noticeable trend. Thus, it is difficult to arrive at meaningful conclusions from these plots. In order to utilize these data sets and more clearly find the effect of damages on AC transport, EIS plots were generated from the raw data. The following sections will include further discussion regarding the EIS plots for each damage type.

5.3 Damage Sensing

As mentioned previously, the specimens used for damage sensing experiments were measured at pre-damage states and after each damage was induced. The electrical measurements were taken using an impedance analyzer, and impedance magnitude and phase angle data were collected. The AC response for each damage type is plotted in EIS plots. EIS plots present the parametric relationship between real and imaginary impedance as a function of interrogation frequency. In the EIS plots, the real part of the impedance is plotted on the x-axis and the negative imaginary part of the impedance is plotted on the y-axis. Plotting the data in this way allows better visualization of the tradeoff between the real and imaginary portions of the impedance as a function of frequency and for different damage states. The low-frequency impedances measured at the pre-damage states were used to normalize both real and imaginary parts of the impedance vector for each specimen (i.e., the lowest frequency measurement for each undamaged state is at one on the horizontal axis). Normalizing the data in this way allows us to more directly compare different specimens. For CNF-modified composite materials, EIS plots typically take the form of semicircles, with low-frequency data at the bottom-right and higher frequencies advancing in the counter clock-wise direction.

5.3.1 Through-hole Damages

Recall that two types of through-hole damage were induced – increasing size of a single through-hole and increasing number of identically sized through-holes. For through-hole damages, the EIS plots for multiple hole damages are shown in Figure 5.6. The EIS plots for increasing hole size damages are shown in Figure 5.8. As a reminder, three specimens were tested for each case. These are referred to as specimens A, B, and C in the forthcoming.

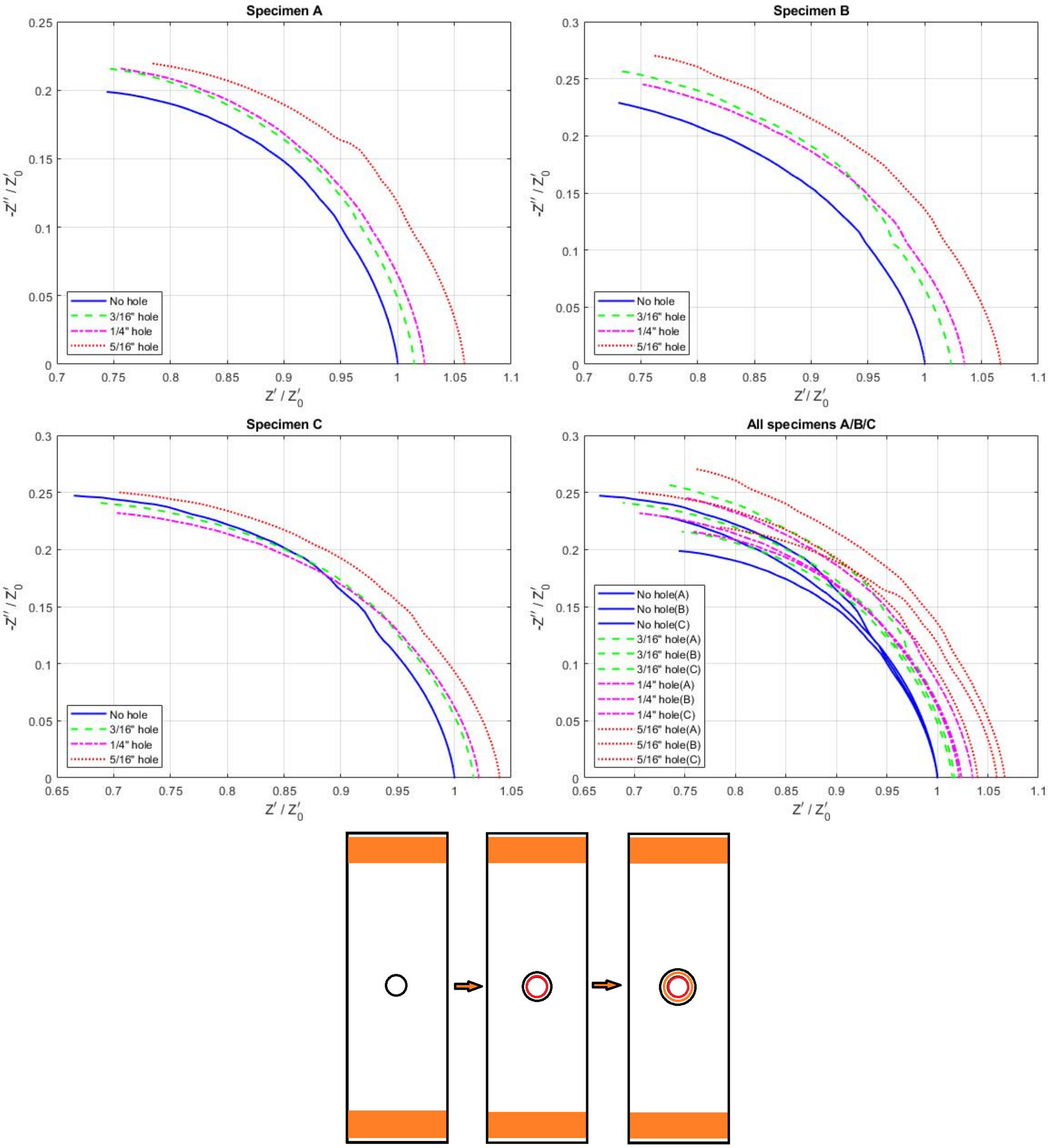

Figure 5.6. EIS data from increasing hole size damages tests (top) and damage state schematic (bottom). Different colors of circle were used in the schematic to indicate previous holes. Orange rectangular boxes at the two sides of the specimens represent electrodes.

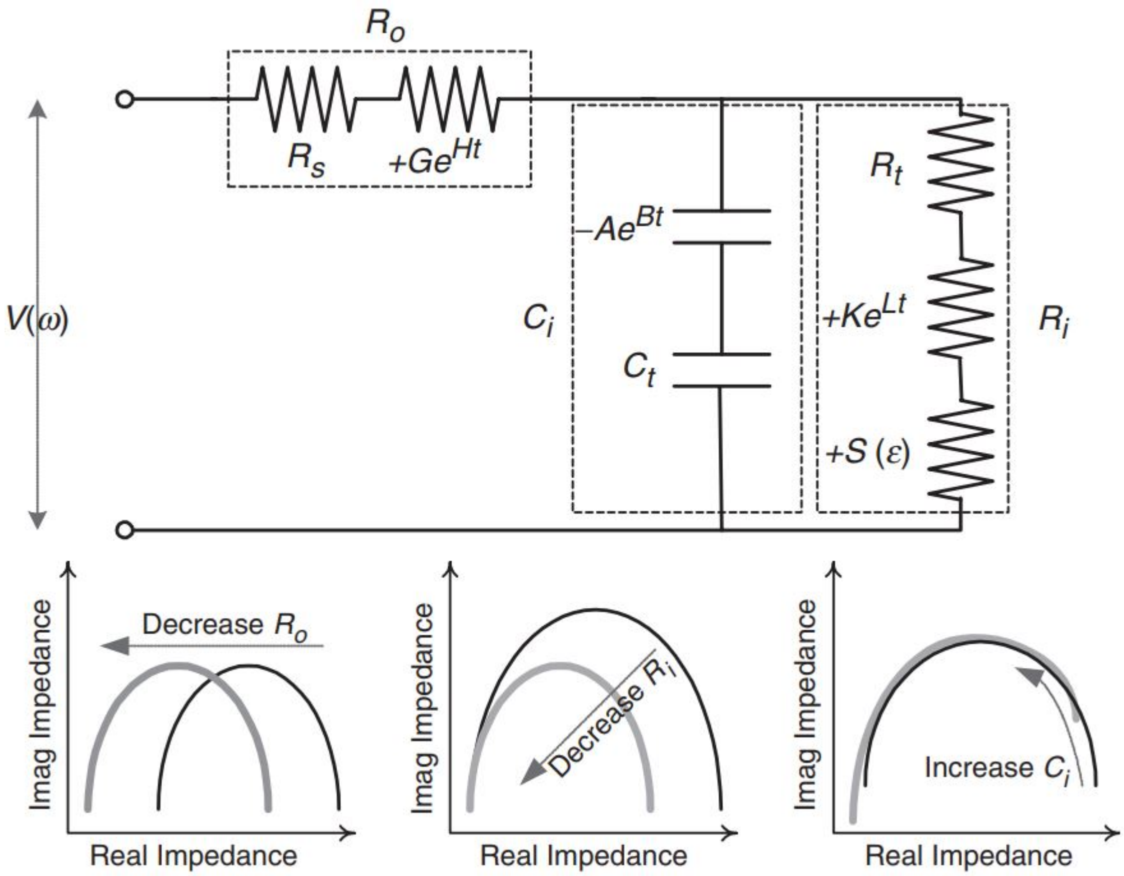

Figure 5.7. Changes in EIS curves due to variations in equivalent circuit element parameters [145].

Consider first Figure 5.6, which shows the effect of increasing through-hole size. A major observation can be made from these plots, that the EIS curves appear to shift outward (i.e., increasing radius) and rightward as the hole size increases. To better understand what these shifts mean with regard to AC transport characteristics, consider prior work by Loh et al. [145]. In this prior work, Loh et al. discretized the semi-circular EIS arc that is characteristic of carbonaceous nanocomposites into an equivalent macroscale circuit consisting of a resistor, R_o, in series with a parallel resistor-capacitor, R_i and C_i, respectively as shown in Figure 5.7. Even though their model had time-dependent parameters to account for viscoelastic effects, an important observation of this work is the effect of each circuit parameter on the EIS curve, as also illustrated in Figure 5.7. This figure shows that when the arc shifts inward and leftward, there is a decrease in resistance of the R_i component. This indicates that the shifting outward and rightward, as observed in the data shown in Figure 5.6, represents an increase in resistance of the specimen as the hole size increases. It also appears that increasing the hole size shifts the curves to the right. In terms of the equivalent circuit, this is akin to increasing the series resistor (i.e., increasing the amount of real impedance in the system).

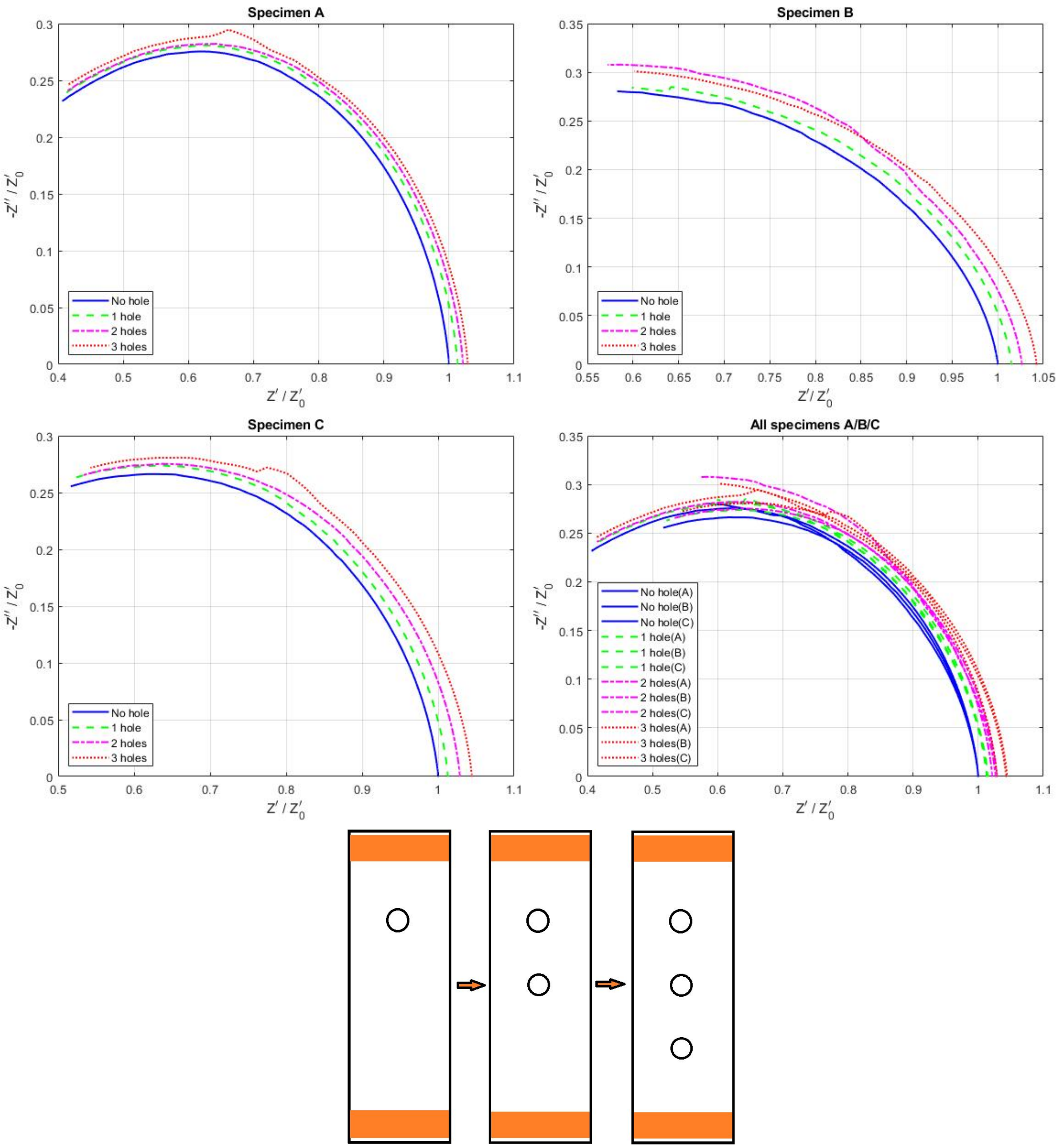

Figure 5.8. EIS data from multiple hole damages tests (top) and damage state schematic (bottom). Black circles were used in the schematic to indicate increasing number of holes.

Next, consider Figure 5.8. These plots show the effect of increasing through-hole numbers on EIS curves. Qualitatively, the results for the increasing number of through-holes (i.e., Figure 5.8) seem to match those for increasing through-hole size (i.e., Figure 5.6). Both damage types show a similar effect on electrical transport in the material. As observed in the low-frequency data region, the arcs in all figures shown in Figure 5.8 again shift outward and rightward as the number of through-holes increases. Recall from the previous discussion on the work of Loh et al. [145], this indicates an increase in the number of damages also shows an increase in the resistance of the material – both in the strictly real sense (i.e., the R_o resistor in series) and in the coupled imaginary sense (i.e., the R_i resistor in parallel with a capacitor). Third, when comparing the Specimen-A plot to the other two specimen plots, it can be observed that the completeness in arc shape of the EIS curve is higher than the ones shown in the other two plots. Based on works presented by Loh et al. [145] and Hassan and Tallman [101], the completeness of the EIS arc is a consequence of the amount of capacitive transport in the material; as the EIS arc extends further in the counter clockwise direction, the total capacitance in the material increases. This suggests that this particular specimen has more inter-filler junctions thereby giving rise to more overall capacitance.

Comparing the two sets of EIS data, one additional observation can be made. It can be noticed that the shifting magnitudes shown in Figure 5.8 increase at a seemly constant rate (i.e., each new hole shifts the curves further to the right by a relatively constant amount), while the results in Figure 5.6 are obviously different (i.e., the rightward shift is not constant for increasing hole size). A possible mechanism for this observation is discussed further at the end of this section.

5.3.2 Notch Damages

Next, recall that notch-type damage testing was done. Two types of notch damages were considered – the effect of increasing notch size and the increasing number of notches. These results are shown in Figures 5.9 and 5.10, respectively.

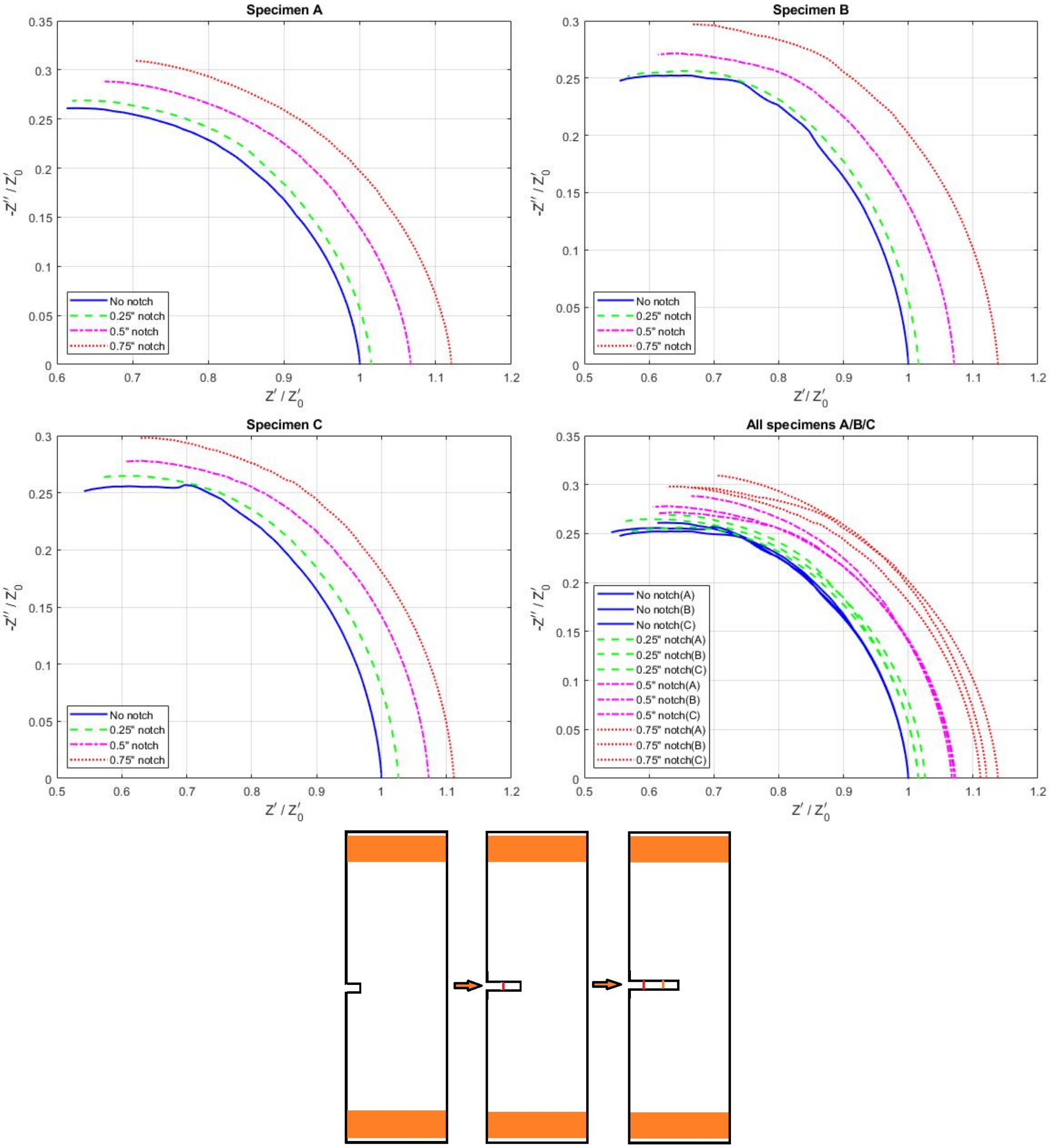

Figure 5.9. EIS data from increasing notch size damages tests (top) and damage state schematic (bottom). Different colors of line segments were used in the schematic to indicate increasing notch sizes.

Consider the effect of notch size first. An obvious observation from these plots is that the EIS curves show a similar trend to those noted from hole damage plots (i.e., Figure 5.6 and 5.8) that the arcs in Figure 5.9 also shift outward and rightward as the size of the notches increase. Recall from the circuit model presented in Figure 5.7; this indicates that the increase in damage size increases the resistance in the series and parallel resistor circuit elements circuit elements.

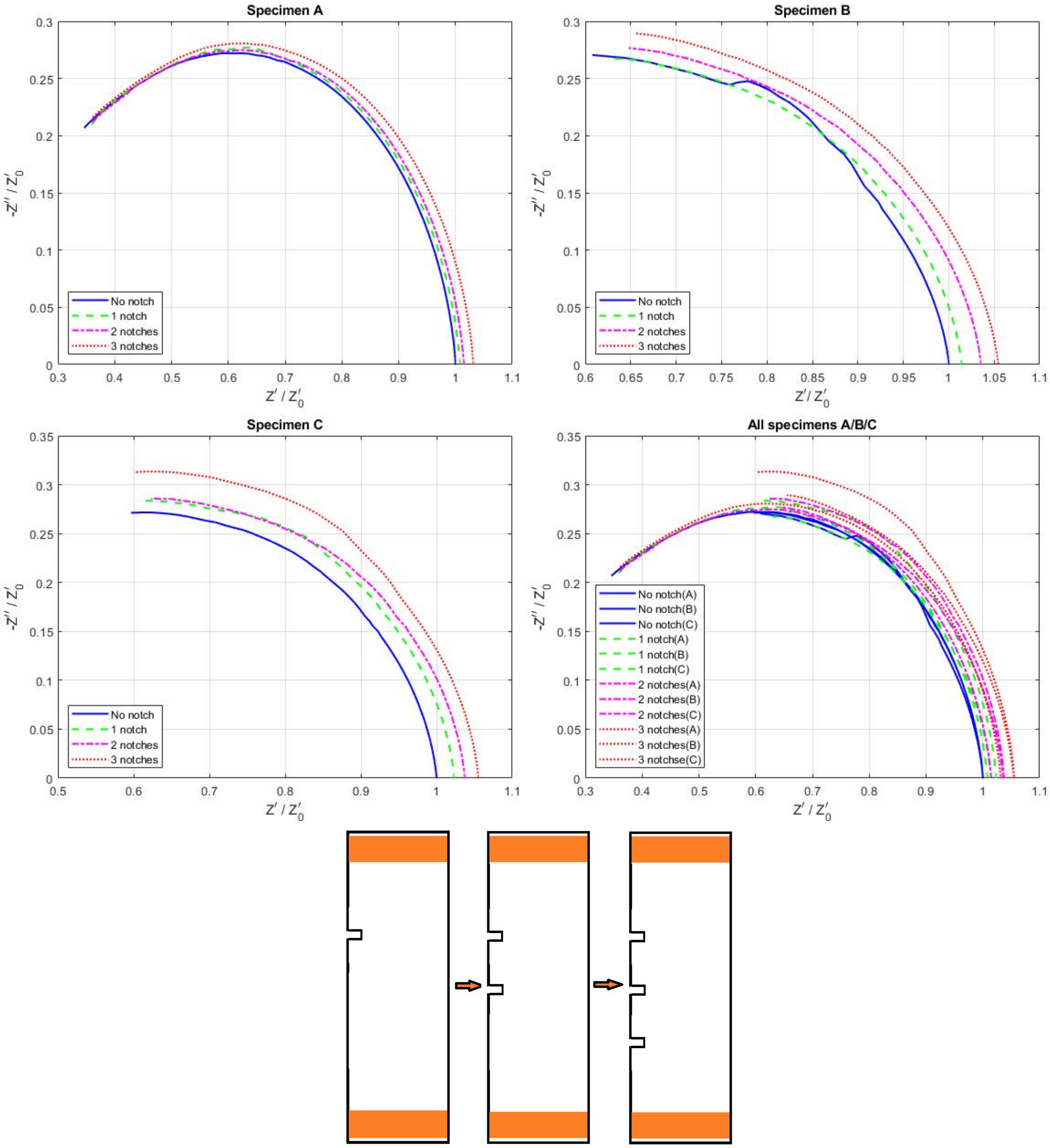

Figure 5.10. EIS data from multiple notch size damages tests (top) and damage state schematic (bottom).

Next, consider the effect of an increasing number of notches on EIS data, as shown in Figure 5.10. One interesting observation can be made in these plots: the curves shown in the Specimen A plot have much higher completeness than those shown in the other two specimen plots. This is similar to what has been observed in the multiple hole damages plots, as shown in Figure 5.8. Recall from the circuit model shown in Figure 5.7, the extension in arcs in a counter clock-wise direction indicates an increase in the capacitance. Again, a shift in outward and rightward can be observed from these plots as the number of notch damage increases.

5.3.3 Impact Damages

Even though the through-hole and notch damages tests help develop some basic insights into how damages affect the frequency-dependent electrical transport properties in self-sensing composites, these damage types are not representative of realistic damages for this material system. Therefore, a set of impact tests were conducted with a drop tower-style impact machine. Recall that three energy levels, 25 J, 30 J, and 35 J, of impacts were conducted five times each on three specimens, and all the impact damages on one specimen were induced at the exact location, which is at the center of the specimen. The results of AC electrical measurements taken before and after each damage can be shown in 5.11.

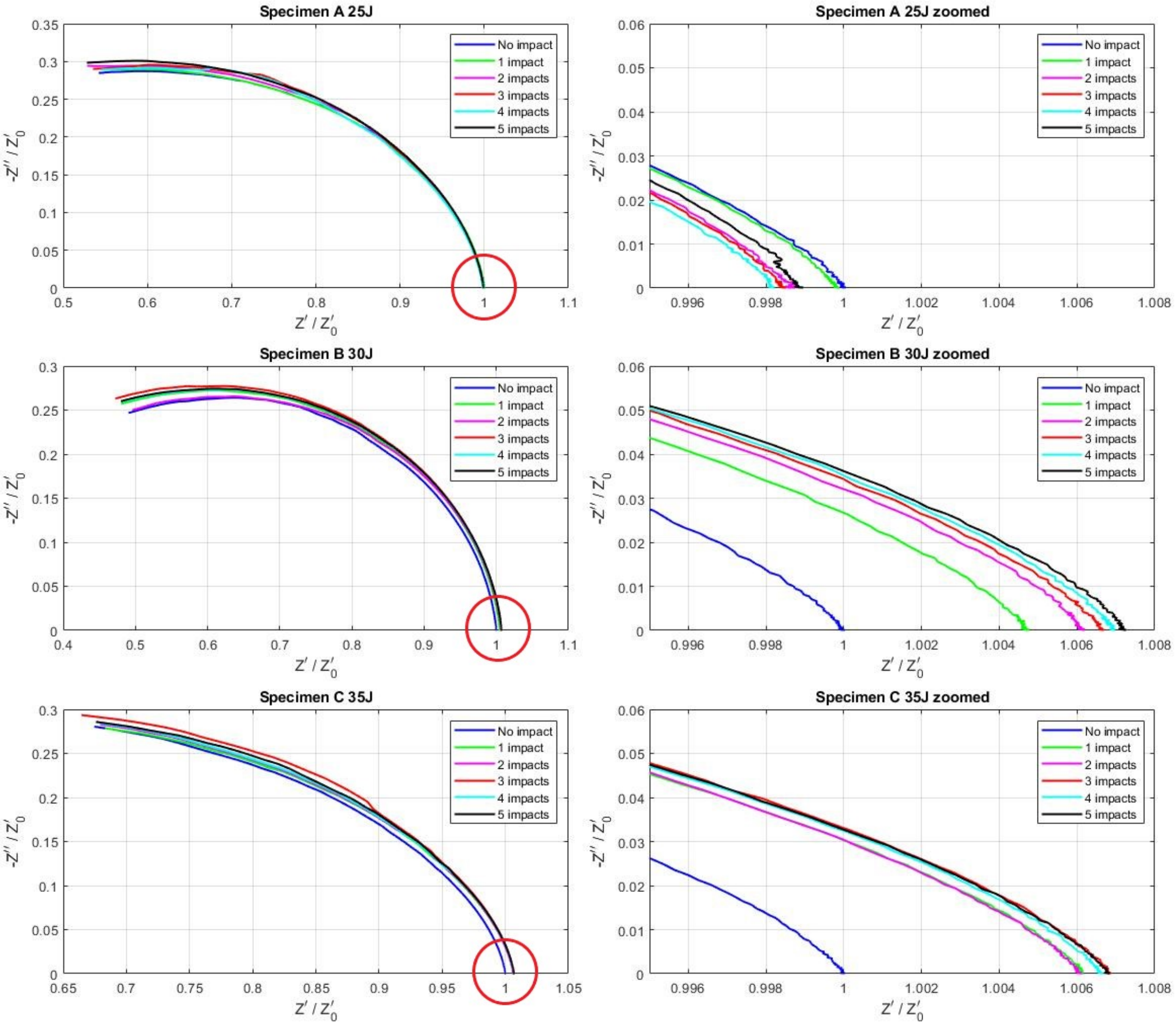

Figure 5.11. EIS data for multiple impact damages specimen. In left column, Specimen A (top) was impacted by 25 J energy, Specimen B (middle) was impacted by 30 J energy, and Specimen C (bottom) was impacted by 35 J energy. Right column shows zoom-in images for impact Specimen A (top), Specimen B (middle), and Specimen C (bottom) at x-intercept.

Several interesting observations can be made from the EIS curves for impact testing. First, it can be seen that the rightward shifts of these curves (due to an increase in resistive transport) are much less pronounced than the previous cases of through-holes and notches. In fact, considering a close-up of the low-frequency regime (i.e., the bottom-right portion of the EIS curves), the curves show an incredibly small rightward shift. An exception to this trend seems to be the 35 J impact load, wherein an increase in resistance can be seen between the un-impacted case and all impacted cases. But even within the impacted cases for the 35 J load, there is extremely tight packing (i.e., the low-frequency portions of the 35 J impacted EIS curves are very close to each other). Building on this first observation, it can secondly be observed that there is much more distinguishability among the EIS curves at high frequencies (i.e., in the top-left portions of the EIS curves). These two observations are noteworthy because together they suggest that high-frequency methods may be better suited for detecting and tracking low-velocity impact damage to self-sensing composites.

5.4 Comparison of Results

Comparing all the EIS plots together, the following observations can be made. First, regardless of the damage type (multiple damages, increasing damage size, and impact damages) or the damage shape (notch and hole), with increasing number or size of the damage, there tends to be an increasing real part and imaginary part of impedance, except the curves shown in Specimen A, Figure 5.8. Also, notably, the impact results showed a much lesser resistance increase. As this study does not develop equivalent AC circuits models for all these damage types, the effects of these damages on equivalent circuit behavior cannot be quantified. Nonetheless, worthwhile qualitative observations can be made. Compared to the circuit model presented by Loh et al. [145], as shown in Figure 5.7, it can be inferred that the parts of the nanofiller network that are equivalent to resistor elements in a circuit were affected by the damages. The equivalent circuit consists of a series resistor, R_o, and a parallel resistor-capacitor, R_i and C_i. Recall also that this model has time-dependent terms to account for viscoelastic effects. Herein, however, we are not concerned with viscoelasticity. As such, the time-dependent terms can be dropped such that the model reduces to simply a resistor in series with a parallel resistor-capacitor. From this configuration, the complex impedance can be derived as shown below.

$$Z_{\mathrm{eq}}(\omega) = R_o + \frac{R_\mathrm{i}}{\omega^2 C_\mathrm{i} + R_\mathrm{i}} - \mathrm{j}\frac{\omega C_\mathrm{i}}{\omega^2 C_\mathrm{i} + R_\mathrm{i}} \tag{5.1}$$

As shown in equation 5.1, $R_o + \frac{R_\mathrm{i}}{\omega^2 C_\mathrm{i} + R_\mathrm{i}}$ is the real part of the impedance, $Z_{eq}(\omega)$, while $\frac{\omega C_\mathrm{i}}{\omega^2 C_\mathrm{i} + R_\mathrm{i}}$ is the imaginary part of the impedance. According to Figure 5.7, shifting the whole

EIS arc leftward indicates a decrease in component R_o, shrinking the arc inward represents a decrease in R_i, and extending in counter clock-wise direction of the arc shows increase in C_i. Based on the previous discussion, with the increasing number or size of the damage, the arcs in damage types that involve material removal all show shifting outward and rightward. According to the equation, the real part of the impedance is affected by all three components in the circuit, while the imaginary part of the impedance is affected by R_i and C_i. Combining the observations and Figure 5.7, using equation 5.1, it can be noted that the increase in R_o and R_i increase both parts of the impedance. From the impact results, the curves are shifting outward, resulting in increase in R_i. According to equation 5.1, this means an increase in both parts of the impedance, however, the increase in the real part of the impedance will be significantly less than the one in other damage types, which agrees with the observation from Figure 5.11.

Looking at Figure 5.6, it can be observed that the shifting magnitudes between small (3/16”) and medium (1/4”) hole curves are much smaller than the ones between no hole and the smallest hole. Similar observation can be made comparing the shifting magnitude between the latter pair of curves to the ones between medium and large (5/16”) holes. Considering that the volume of material removed from the specimen increases between each damage state, the magnitude of change in low-frequency impedance may be a consequence of the different amounts of material removed. Comparing the shifting magnitudes shown in Figure 5.6 and 5.9, it can be noticed that the magnitudes in the increase size notch are greater than the ones in the increase size hole. This may again be due to the amount of material removed in these two damage types being different.

In order to better visualize and quantify the effect of material removal on the low-frequency impedance, estimated volume calculations were made. The average thickness of the specimens is approximately 4.32 mm. Assuming the removed hole can be regarded as a cylinder, the volume of each hole damage can be calculated. For the notch damages, based on the width of the tile saw blade (1/16”) used to cut the notches informed in the procedure section, the assumption that the cut-out notch is in the shape of a rectangular box, an estimation of the volumes can also be calculated. With that information, a plot showing the relationship between volume removed in material and the normalized low-frequency (i.e., 100 Hz) real impedance is shown below in Figure 5.12.

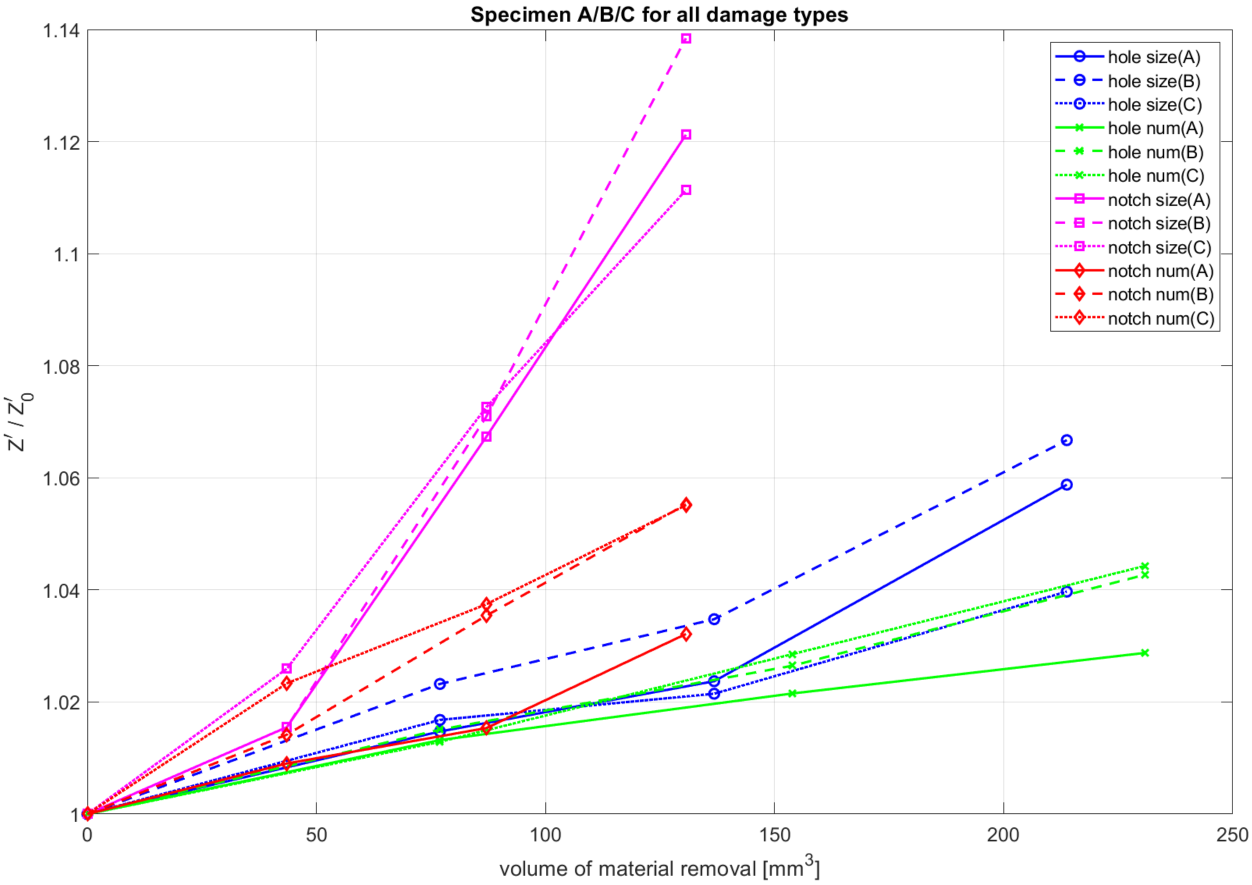

Figure 5.12. Normalized impedance against material removal volume for all specimens.

As shown in the figure, the volume difference between the 1/4" and 5/16" hole in hole size damage curves is more significant than the ones between the 3/16" and 1/4" hole, hence the rightward shifting magnitude of the EIS curves is different. Additionally, the volume difference between the medium and large holes (pair A) is the same as the ones between no hole and small hole (pair B). Assuming the volume of removed material is linearly related to the shifting magnitude, it is expected to see the shifting magnitudes in pair A and pair B to be the same. However, this is not observed in Figures 5.6 and 5.12.

Comparing the curves for increase hole size damages and multiple hole damages, it can be noticed that the multiple hole damage curves show a more linear relation between removed material and normalized real impedance than the increase hole size damage curves do. This is because the volume of removed material of increase hole size damage increased non-linearly, while the volume of removed material of multiple hole damage increased at a constant rate. This may indicate a possible relationship between material removal and AC response. It can also be noticed that multiple hole damages remove more material than increased hole size damages, but increase less in low-frequency impedance. This suggests that removing more material does not mean more increase in low-frequency impedance.

A similar observation can be made when comparing all the curves in Figure 5.12. It can be observed that the volume of removed material for increasing size notch (purple) and multiple notches (red) curves are much smaller than those in increase size hole (blue) and multiple holes (green) curves. However, when comparing the increased magnitude of normalized real impedance, it can be noticed that the values from the increase size notch are greater than those from the increase size hole. Similarly, the values from multiple notches are greater than those from multiple holes. This also indicates that the volume of removed material may not be the only cause that affects the shifting magnitude in EIS curves. Recall from the DC conductivity formula shown in equation 4.5; another possible factor that may affect the shifting magnitude is the cross-sectional area at the damage location. Based on the previous assumptions and estimated dimensions, normalized real impedance is plotted as a function of the cross-sectional area at the damage location of the increase size notch and hole damages, as shown in Figure 5.13 below.

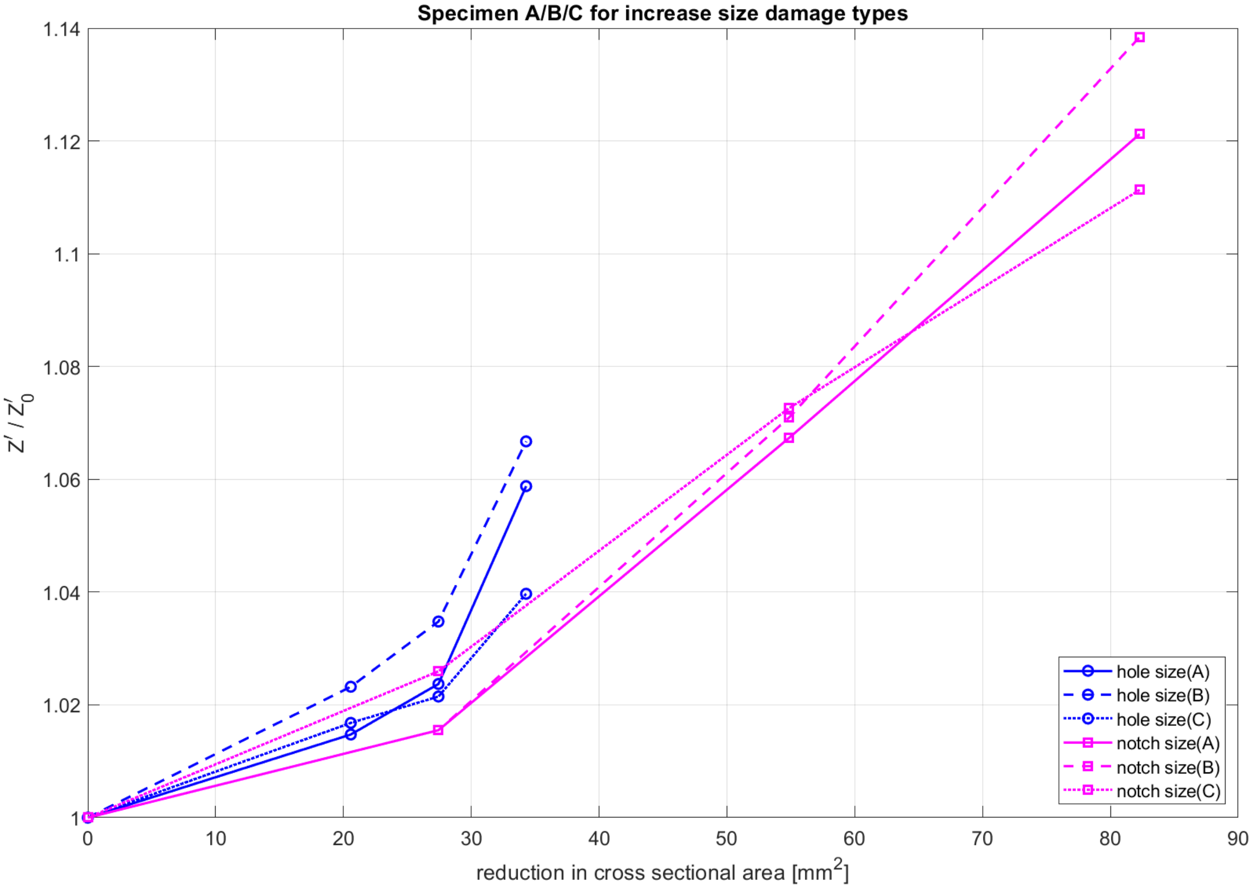

Figure 5.13. Normalized impedance against material removal volume for all increase size hole and notch specimens.

According to Figure 5.13, it can be observed that the notch size curves have a greater magnitude of increase in both normalized real impedance and removed cross-sectional area than the hole size curves do at each damage state. Looking at the first damage state, it is noticed that the increased magnitudes in normalized real impedance do not show much of a difference between the two damage types. From the second damage state, the increased magnitudes of the normalized real impedance of notch size damage are much greater than the hole size damage. It can also be noticed that the increased magnitudes of the removed cross-sectional area of notch size damage are more significant than the ones of hole size damage. These observations raise the possibility that the amount of decrease in cross-sectional area at the damage location does affect the amount of increase in normalized real impedance.

In addition, notice that even though the magnitudes of change in removed cross-sectional area are the same between the three damage states, the curves of hole size damage shown in Figure 5.13 do not show a linear increase. Recall that the volume of removed material in hole size damages increases non-linearly. These observations raise the discussion that material removal and decrease in the cross-sectional area affect electrical transport in the material. These two parameters may be used as references when investigating damages in self-sensing material.

Building on the previous discussion of the shifting behavior in damage types that involve material removal, a second discussion can be made on the impact damages. Unlike the previous four damage types, the impact damages affect the material in the sense of internal damages, such as fiber breakage. Recall from the observations based on Figure 5.11 that the EIS curves in impact damage do not show noticeable shifting rightward but do have notable outward shifting in the high-frequency regime. Compared to plots from other damage types, which consistently show increases in resistance as the damage size or number increases, it can be interpreted that the internal damages caused by impact do not show significant contributions to the increase in resistance. This concludes that material removal damages can shift the EIS arc rightward and outward. The volume of removed material and the removed cross-sectional area affect their magnitudes of shifting. The EIS arcs will likely shift outward if the damages do not involve material removal like impacts. Measuring AC electrical properties at higher frequencies seems to be favorable for detecting damages caused by low-velocity impacts in self-sensing materials.

5.5 fdEIT Simulation

Next, we look at the effect of using frequency-difference methods in EIT for baseline-free damage detection. Using the one-step minimization fdEIT approach as previously described, the through-hole damage simulated on a mesh, as shown in Figure 4.10, was reconstructed as shown in Figure 5.14. As mentioned previously, this simulation was informed by the experimentally measured AC conductivity of the 0.5 wt.% CNF/epoxy-modified biaxial glass fiber, due to this weight fraction showing fairly consistent transport properties and exhibiting a clear change in AC conductivity at relatively modest frequencies. The two AC conductivity values were chosen at frequencies of $\omega_1/2\pi = 1$ MHz and $\omega_2/2\pi = 10$ MHz. Equation 4.7 was used to find the AC conductivities, and the relative permittivity was estimated from experimental literature as shown in Figure 4.10. The resulting admittivities used to inform the simulation were $\xi_{\omega_1} = 0.12 + 1.11 \times 10^{-4}\text{j}$ S/m and $\xi_{\omega_2} = 0.34 + 6.56 \times 10^{-5}\text{j}$ S/m. Next, the forward problem formulation shown in the theory section was used to predict the voltage-current response on the damage mesh, and the fdEIT inverse problem was used to reconstruct the damage imaging on the other mesh, as shown in Figure 5.14 below. Note that both plots were normalized such that the maximum change in magnitude is one. The image on the left shows the real part of the change in admittivity, and the image on the right shows the change in the imaginary part of the admittivity.

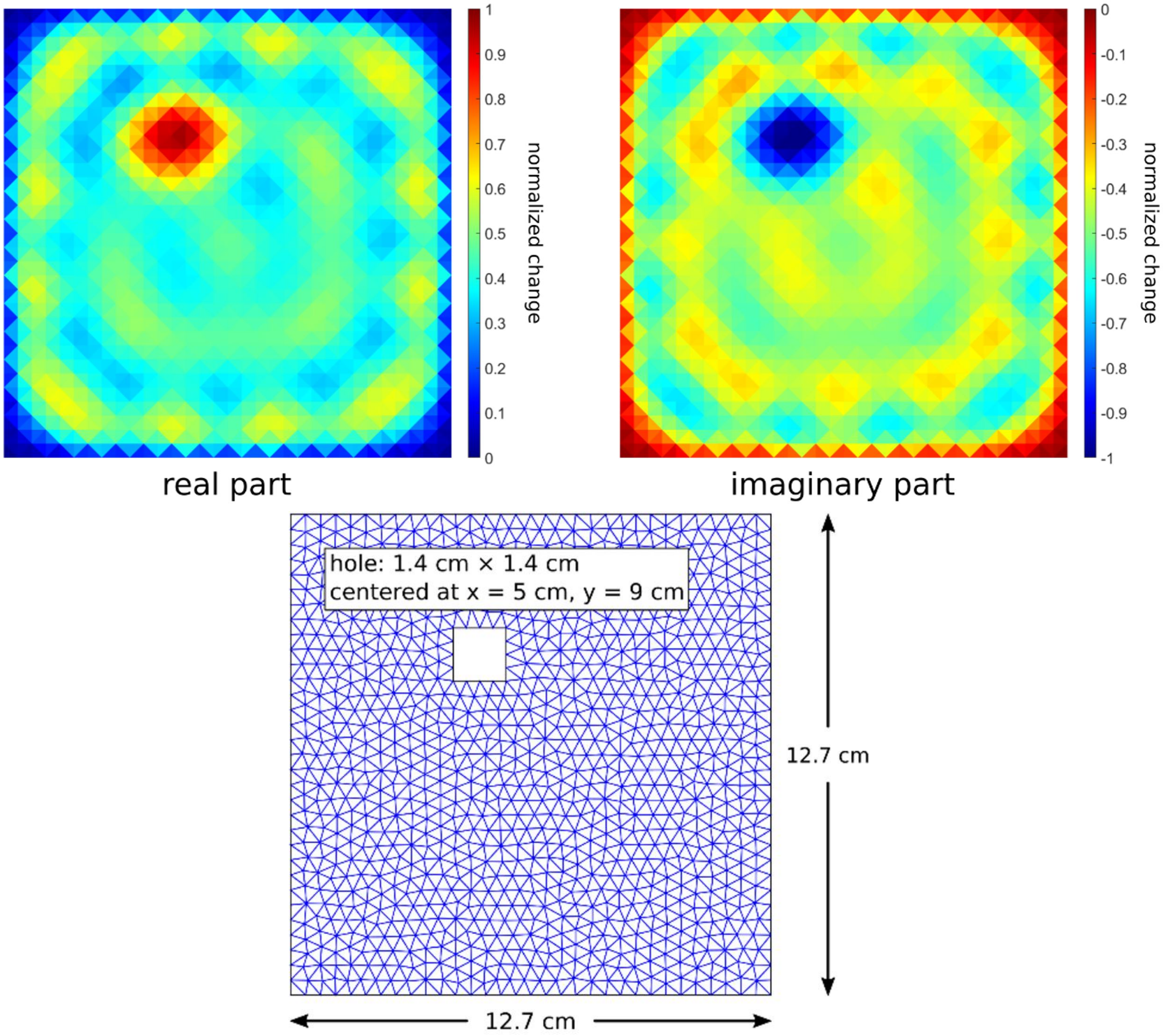

Figure 5.14. The damage reconstruction from fdEIT with real part (left) and imaginary part (right) of the admittivity change. Damage mesh from Figure 4.10 is attached (bottom) for comparison.

Several notable observations can be made from Figure 5.14. First, the simulated damage can be seen clearly in both the real and imaginary parts of the fdEIT-predicted admittivity change. As shown in Figure 5.14, real part of admittivity shows a region with high color contrast compared to the surrounding background, marking the damage area. Similar observation can be made from imaginary part of admittivity image. In addition, the size and location of the damage in Figure 5.14 show good agreement with the actual size and location shown in Figure 4.10.

Second, a positive change of admittivity can be observed away from the hole in the real part of the image, and a negative change of admittivity can be observed away from the hole in the imaginary part of image. A positive change in the real part of admittivity is expected since $\Re\left(\xi(\omega_1)\right) < \Re\left(\xi(\omega_2)\right)$, where $\Re$ indicates the real portion of the admittivity. Similarly, a negative change in the imaginary part of admittivity is expected since $\Im\left(\xi(\omega_1)\right) > \Im\left(\xi(\omega_2)\right)$, where $\Im$ represents the imaginary part of the admittivity. Thus, the predictions of the fdEIT algorithm agree with our expectations away from the damage region.

Third, recall that the damage was simulated to be through-hole damage (i.e., there is no material at the damage location). Thus, we expect the fdEIT-predicted admittivity change to be zero at the hole location. But this is not observed in the results.

Lastly, zero admittivity changes were observed at the boundaries of both images, forming so-called boundary artifacts. Other artifacts can also be observed in the two images. The real part image shows distributed zones with increases in admittivity change in the background, and similar observations can be made from the imaginary image. The exact reasons for these last two observations are not fully known at this point. However, it is speculated that this may be a consequence of this particular fdEIT formulation and the artifacts to be imaged. That is, in most EIT applications, a concreted region of non-zero conductivity change is sought from a background of zero change. But it is the opposite in this work; a concentrated region of zero change (i.e., the damage) is sought from a background of constant change. Overcoming this challenge may require new regularization formulations that account for the nature of this expected solution. Another option is to explore voltage normalization techniques commonly used in biomedical multi-frequency methods of EIT [136] [146] [147].

6. SUMMARY, CONCLUSIONS, AND RECOMMENDATIONS FOR FUTURE WORK

6.1 Summary

In summary, this thesis studied the effect of different damage types on AC transport in a representative self-sensing composite and also explored the potential of frequency-difference methods to eliminate the need for a baseline in EIT. This work was motivated by the potential of self-sensing materials in diverse and far-reaching technological areas (e.g., healthcare, robotics, SHM and NDE, etc.), the potential of AC methods to improve state-of-the-art DC methods, and the comparative dearth of studies on AC-based self-sensing. This is important as AC has greater data density, higher sensitivity through electrodynamic effects, and lower power requirements. Therefore, this research was conducted to provide contributions to overcome this gap in state of the art.

Specimens were made with 0.25, 0.35, 0.5, 1.0, 1.5 wt.% CNF/epoxy with biaxial glass fiber fabric for baseline AC electrical transport measurements. For electrical measurements, these specimens were cut into small squares for DC and AC conductivity measurements. A DC conductivity curve of this material system was produced, and the admittivity values used to inform the fdEIT simulation were selected based on the AC conductivity curves.

For artificial damage testing, 0.75 wt.% CNF-modified unidirectional glass fiber/epoxy rectangular specimens were induced with five different damage types, including increasing size through-holes, multiple through-holes, increasing size notches, multiple notches, and multiple impacts at three energy levels. In these tests, impedance magnitude and phase angle measurements were taken before and after the damages were induced. The electrodes were placed on the two edges across the length. Using the collected data from these tests, EIS curves were generated to better visualize the effect of damages on the electrical properties, specifically the effect on real and imaginary impedance. For all the EIS curves, except the ones for impact damage, an increase in both real and imaginary parts of the impedance can be observed. For increasing notch size damage, EIS curves show a greater change in magnitude of both real and imaginary parts of the complex impedance. More changes in the imaginary part of impedance can be noticed in the high-frequency region than in the low-frequency region in the impact damage EIS plots. Thus, high-frequency methods may be better suited for detecting and tracking impact-type damage, whereas low-frequency methods may be better suited for detecting and tracking damage that removes material from the specimen (e.g., notches and holes).

The AC conductivity values used to inform the fdEIT simulations were supplemented with relative permittivity values for a CNF nanocomposite from experimental literature. Damage was simulated on one finite element mesh with through-hole damage and reconstructed on another mesh. The EIT forward problem was used to predict voltage-current response on the damage mesh. Several observations were made based on the reconstruction images showing the real and imaginary parts of admittivity change. First, simulated damages can be clearly seen, and the size and location of the predicted damage show good agreement with the actual damage location. Second, the direction of change in admittivity agrees with expectations away from the damaged area. Third, no admittivity change at the damaged area was expected. This was not observed in the fdEIT results presented in this work. Lastly, zero change of admittivity was observed at the boundary of both real and imaginary fdEIT plots, forming boundary artifacts. The source of these last two observations requires further investigation.

6.2 Conclusions

We can arrive at several conclusions from the work presented in this thesis. First, recall the AC conductivity measurements for each weight fraction were taken from 100 Hz to 10 MHz. Based on the data collected, it can be inferred that at a higher weight fraction, the AC transport in this material system is more likely to be dominated by filler and inter-filler resistance in this range of frequency. This is evident by the frequency-independent plateau of the AC conductivity curves extending to higher frequencies for the higher CNF weight fraction specimens. On the other hand, as the CNF weight fraction decreases, the AC transport shows more frequency-dependent behavior (i.e., AC conductivity increase as frequency increase at a lower frequency range). This observation was used to determine the weight fraction for specimens in the two sets of experiments, but it can also provide a guideline for future work in these material systems. That is, for frequency-dependent behavior to be exploited, the material must be produced at a filler weight fraction such that frequency effects are appreciable in the frequency range of interest. For example, in this work, 0.5 wt.% specimens were used to inform the fdEIT simulations, and 0.75 wt.% specimens were manufactured to conduct damage sensing experiments.

Second, recall that from the comparison of the results presented for artificial damages and impact damage, a major difference of note is the magnitude of change in the real part of impedance in the low-frequency regime. Based on the circuit model presented by Loh. et al. [145] shown in Figure 5.7 and the equation derived for an equivalent circuit shown in equation 5.1, the rightward shift indicates an increase in the series resistance, while outward shifting represents an increase in the parallel resistance. Observations have been made that EIS curves for material removal damages show clear outward and rightward shifting, while impact damage curves only show noticeable shifting in the high-frequency regime. This implies that damages that removed material in the specimen can induce effects on both parts of the complex impedance, while internal damages caused by low-velocity impacts may only affect the imaginary part of the impedance (i.e., little-to-no change in the series resistance of the system). In addition, based on the observations of impact results in both low and high-frequency regimes, it can be noted that measuring AC electrical properties in higher frequencies may be more suitable for detecting and tracking damages caused by low-velocity impacts in self-sensing material. More work is needed to determine if this trend continues for other types of damage that does not result in material loss (e.g., fiber breakage).

Lastly, fdEIT was able to successfully locate and roughly size damage in the experimentally informed simulation environment. As the fdEIT formulation presented only uses the data at two different frequencies both of which are for the damaged state rather than time-difference data, this success hints at potential for a path towards baseline free EIT. Despite this promising result, the resulting images also suffer from boundary artifacts and unexpected changes in admittivity in the damaged area. The cause of these observations are not fully understood at this time; however, they could be a consequence of this particular inverse formulation. Alternative solutions include applying voltage normalization techniques commonly used in biomedical multi-frequency methods of EIT. Nonetheless, even this preliminary success seems to merit more work in the area of materials based EIT outside the area of just nanocomposites.

6.3 Recommendations for Future Work

Based on the results of this work, several recommendations for future work are made. First, the damage sensing tests presented in this work were conducted under different types of artificial damage that involved a relatively large amount of material removal. However, components in real life are rarely damaged in such ways. Therefore, it is vital that more realistic damage types such as impacts and fatigue loading should be looked into for future damage sensing testing.

Second, it is recommended to develop more accurate models of an equivalent circuit to better quantify the effect of damages on AC transport in this material system, similar to the methodology present in work from Loh et al. [145]. This method of approach is vital for developing damage detection techniques using AC electrical measurements and has been well applied in prior work in this research group [99] [138] [139] [148].

Third, while the fdEIT simulation presented in this work has successfully localized and sized through-hole damage, much work remains to make this a viable non-destructive modality. 1) Imaging artifacts (boundary and counter-intuitive changes at the hole location) need to be addressed. As suggested previously, new regularization formulations and voltage normalization techniques used in biomedical multi-frequency methods of EIT [136] [146] [147] can be explored to help solve the problem. 2) As the next step for fdEIT is to conduct tests on actual specimens, it is crucial to take experimental procedures into consideration. As a significant part of the fdEIT tests, methods and systems designed for electrical measurements in the biomedical multi-frequency methods of EIT may not be suitable for high-frequency measurements in other cases. Therefore, new methods of electrical measurements need to be designed for fdEIT experiments. 3) To expand the potential of fdEIT in detecting damage, it is essential to include more physical constraints into the inverse problem formulations. Sannamani [144] has developed three different sensitivity matrix formulations with physical constraints such as in-plane and through-thickness DC conductivity and successfully detected impact damages in an airfoil shape specimen. This suggests physical constraints in terms of AC conductivity and permittivity changes are needed for future work in fdEIT.

REFERENCES

[1] R. I. Ponder, M. Safaei, and S. R. Anton, "Validation of impedance-based structural health monitoring in a simulated biomedical implant system," in *Smart Materials, Adaptive Structures and Intelligent Systems*, American Society of Mechanical Engineers, vol. 51951, 2018, V002T05A008.

[2] E. L. Ribolla and P. Rizzo, "Modeling the electromechanical impedance technique for the assessment of dental implant stability," *Journal of biomechanics*, vol. 48, no. 10, pp. 1713–1720, 2015.

[3] J. L. Abot, Y. Song, M. S. Vatsavaya, S. Medikonda, Z. Kier, C. Jayasinghe, N. Rooy, V. N. Shanov, and M. J. Schulz, "Delamination detection with carbon nanotube thread in self-sensing composite materials," *Composites Science and Technology*, vol. 70, no. 7, pp. 1113–1119, 2010.

[4] A. A. Eddib and D. Chung, "First report of capacitance-based self-sensing and in-plane electric permittivity of carbon fiber polymer-matrix composite," *Carbon*, vol. 140, pp. 413–427, 2018.

[5] X. Fu, E. Ma, D. Chung, and W. Anderson, "Self-monitoring in carbon fiber reinforced mortar by reactance measurement," *Cement and concrete research*, vol. 27, no. 6, pp. 845–852, 1997.

[6] J. Han, J. Pan, J. Cai, and X. Li, "A review on carbon-based self-sensing cementitious composites," *Construction and Building Materials*, vol. 265, p. 120 764, 2020.

[7] M. Saafi, L. Tang, J. Fung, M. Rahman, F. Sillars, J. Liggat, and X. Zhou, "Graphene/fly ash geopolymeric composites as self-sensing structural materials," *Smart materials and structures*, vol. 23, no. 6, p. 065 006, 2014.

[8] H. Deng, Y. Gao, R. Hu, S. Zhao, G. Han, X. Lian, M. Ma, and X. Zhong, "Self-sensing automotive magnetorheological dampers for low frequency vibration," *Smart Materials and Structures*, vol. 30, no. 11, p. 115 015, 2021.

[9] A. Badel, J. Qiu, and T. Nakano, "Self-sensing force control of a piezoelectric actuator," *IEEE transactions on ultrasonics, ferroelectrics, and frequency control*, vol. 55, no. 12, pp. 2571–2581, 2008.

[10] C. Chen and W.-H. Liao, "A self-sensing magnetorheological damper with power generation," *Smart Materials and Structures*, vol. 21, no. 2, p. 025 014, 2012.

[11] *Total artificial knee replacement surgery (arthroplasty) in thailand.* [Online]. Available: https://www.thaimedicalvacation.com/knee-replacement-in-thailand-overview-with-costs-alternatives/.

[12] C.-Y. Lo, Y. Zhao, C. Kim, Y. Alsaid, R. Khodambashi, M. Peet, R. Fisher, H. Marvi, S. Berman, D. Aukes, *et al.*, "Highly stretchable self-sensing actuator based on conductive photothermally-responsive hydrogel," *Materials Today*, vol. 50, pp. 35–43, 2021.

[13] T. Hainsworth, L. Smith, S. Alexander, and R. MacCurdy, "A fabrication free, 3d printed, multi-material, self-sensing soft actuator," *IEEE Robotics and Automation Letters*, vol. 5, no. 3, pp. 4118–4125, 2020.

[14] D. Zhou, W. Zuo, X. Tang, J. Deng, and Y. Liu, "A multi-motion bionic soft hexapod robot driven by self-sensing controlled twisted artificial muscles," *Bioinspiration & Biomimetics*, vol. 16, no. 4, p. 045 003, 2021.

[15] H. Choi, S. Choi, and H. Cha, "Structural health monitoring system based on strain gauge enabled wireless sensor nodes," in *2008 5th International Conference on Networked Sensing Systems*, IEEE, 2008, pp. 211–214.

[16] I. Bayane and E. Brühwiler, "Structural condition assessment of reinforced-concrete bridges based on acoustic emission and strain measurements," *Journal of Civil Structural Health Monitoring*, vol. 10, no. 5, pp. 1037–1055, 2020.

[17] G. C. Kahandawa, J. Epaarachchi, H. Wang, and K. Lau, "Use of fbg sensors for shm in aerospace structures," *Photonic Sensors*, vol. 2, no. 3, pp. 203–214, 2012.

[18] S. Minakuchi and N. Takeda, "Recent advancement in optical fiber sensing for aerospace composite structures," *Photonic Sensors*, vol. 3, no. 4, pp. 345–354, 2013.

[19] B. Lin and V. Giurgiutiu, "Modeling and testing of pzt and pvdf piezoelectric wafer active sensors," *Smart Materials and Structures*, vol. 15, no. 4, p. 1085, 2006.

[20] R. Rajamani and J. K. Hedrick, "Adaptive observers for active automotive suspensions: Theory and experiment," *IEEE Transactions on control systems technology*, vol. 3, no. 1, pp. 86–93, 1995.

[21] D. Bühler, T. Oxland, and L.-P. Nolte, "Design and evaluation of a device for measuring three-dimensional micromotions of press-fit femoral stem prostheses," *Medical engineering & physics*, vol. 19, no. 2, pp. 187–199, 1997.

[22] R. DeLong and W. H. Douglas, "An artificial oral environment for testing dental materials," *IEEE Transactions on Biomedical Engineering*, vol. 38, no. 4, pp. 339–345, 1991.

[23] A. Goswami, A. Quaid, and M. Peshkin, "Identifying robot parameters using partial pose information," *IEEE Control Systems Magazine*, vol. 13, no. 5, pp. 6–14, 1993.

[24] J. Olivera, M. González, R. Varga, A. Zhukov, J. J. Anaya, *et al.*, "An embedded stress sensor for concrete shm based on amorphous ferromagnetic microwires," *Sensors*, vol. 14, no. 11, pp. 19 963–19 978, 2014.

[25] M. Saafi, K. Andrew, P. L. Tang, D. McGhon, S. Taylor, M. Rahman, S. Yang, and X. Zhou, "Multifunctional properties of carbon nanotube/fly ash geopolymeric nanocomposites," *Construction and Building Materials*, vol. 49, pp. 46–55, 2013.

[26] K. Aono, H. Hasni, O. Pochettino, N. Lajnef, and S. Chakrabartty, "Quasi-self-powered piezo-floating-gate sensing technology for continuous monitoring of large-scale bridges," *Frontiers in Built Environment*, vol. 5, p. 29, 2019.

[27] M. Sarwary, G. Yıldırım, A. Al-Dahawi, Ö. Anıl, K. A. Khiavi, K. Toklu, and M. Şahmaran, "Self-sensing of flexural damage in large-scale steel-reinforced mortar beams," *ACI Materials Journal*, vol. 116, no. 4, pp. 209–221, 2019.

[28] A. D'Alessandro, M. Rallini, F. Ubertini, A. L. Materazzi, and J. M. Kenny, "Investigations on scalable fabrication procedures for self-sensing carbon nanotube cement-matrix composites for shm applications," *Cement and Concrete Composites*, vol. 65, pp. 200–213, 2016.

[29] S. Ahmed, S. Doshi, T. Schumacher, E. T. Thostenson, and J. McConnell, "Novel self-sensing carbon nanotube-based composites for rehabilitation of structural steel members," in *AIP conference proceedings*, AIP Publishing LLC, vol. 1706, 2016, p. 120 004.

[30] W. Dong, W. Li, Z. Luo, Y. Guo, and K. Wang, "Effect of layer-distributed carbon nanotube (cnt) on mechanical and piezoresistive performance of intelligent cement-based sensor," *Nanotechnology*, vol. 31, no. 50, p. 505 503, 2020.

[31] Z. Tian, Y. Li, J. Zheng, and S. Wang, "A state-of-the-art on self-sensing concrete: Materials, fabrication and properties," *Composites Part B: Engineering*, vol. 177, p. 107 437, 2019.

[32] A. Todoroki, K. Suzuki, Y. Mizutani, and R. Matsuzaki, "Durability estimates of copper plated electrodes for self-sensing cfrp composites," *Journal of Solid Mechanics and Materials Engineering*, vol. 4, no. 6, pp. 610–620, 2010.

[33] A. K. Das, D. K. Mishra, J. Yu, and C. K. Leung, "Smart self-healing and self-sensing cementitious composites—recent developments, challenges, and prospects," *Advances in Civil Engineering Materials*, vol. 8, no. 3, pp. 554–578, 2019.

[34] J. Zhu, S. Wei, J. Ryu, M. Budhathoki, G. Liang, and Z. Guo, "In situ stabilized carbon nanofiber (cnf) reinforced epoxy nanocomposites," *Journal of Materials Chemistry*, vol. 20, no. 23, pp. 4937–4948, 2010.

[35] S. Sasmal, N. Ravivarman, B. Sindu, and K. Vignesh, "Electrical conductivity and piezoresistive characteristics of cnt and cnf incorporated cementitious nanocomposites under static and dynamic loading," *Composites Part A: Applied Science and Manufacturing*, vol. 100, pp. 227–243, 2017.

[36] J. H. Kang, C. Park, J. A. Scholl, A. H. Brazin, N. M. Holloway, J. W. High, S. E. Lowther, and J. S. Harrison, "Piezoresistive characteristics of single wall carbon nanotube/polyimide nanocomposites," *Journal of Polymer Science Part B: Polymer Physics*, vol. 47, no. 10, pp. 994–1003, 2009.

[37] A. Sanli, A. Benchirouf, C. Müller, and O. Kanoun, "Piezoresistive performance characterization of strain sensitive multi-walled carbon nanotube-epoxy nanocomposites," *Sensors and Actuators A: Physical*, vol. 254, pp. 61–68, 2017.

[38] P. Sikora, E. Horszczaruk, K. Cendrowski, and E. Mijowska, "The influence of nano-fe3o4 on the microstructure and mechanical properties of cementitious composites," *Nanoscale Research Letters*, vol. 11, no. 1, pp. 1–9, 2016.

[39] A. M. Rashad, "A synopsis about the effect of nano-al2o3, nano-fe2o3, nano-fe3o4 and nano-clay on some properties of cementitious materials–a short guide for civil engineer," *Materials & Design (1980-2015)*, vol. 52, pp. 143–157, 2013.

[40] M. Amin, S. El-Gamal, and F. Hashem, "Effect of addition of nano-magnetite on the hydration characteristics of hardened portland cement and high slag cement pastes," *Journal of thermal analysis and calorimetry*, vol. 112, no. 3, pp. 1253–1259, 2013.

[41] A. Al-Dahawi, M. H. Sarwary, O. Öztürk, G. Yıldırım, A. Akın, M. Şahmaran, and M. Lachemi, "Electrical percolation threshold of cementitious composites possessing self-sensing functionality incorporating different carbon-based materials," *Smart Materials and Structures*, vol. 25, no. 10, p. 105 005, 2016.

[42] Y. Fang, L.-Y. Li, and S.-H. Jang, "Calculation of electrical conductivity of self-sensing carbon nanotube composites," *Composites Part B: Engineering*, vol. 199, p. 108 314, 2020.

[43] D. Chung, "Structural health monitoring by electrical resistance measurement," *Smart materials and structures*, vol. 10, no. 4, p. 624, 2001.

[44] A. K. Cholker and M. Tantray, "Electrical resistance-based health monitoring of structural smart concrete," *Materials Today: Proceedings*, vol. 43, pp. 3774–3779, 2021.

[45] Y. Mao, Y. Yu, D. Wu, and X. Yang, “Monitoring failure behaviour of pultruded cfrp composites by electrical resistance measurement,” *Carbon letters*, vol. 5, no. 1, pp. 18–22, 2004.

[46] S. Datta, R. K. Neerukatti, and A. Chattopadhyay, “Buckypaper embedded self-sensing composite for real-time fatigue damage diagnosis and prognosis,” *Carbon*, vol. 139, pp. 353–360, 2018.

[47] I. Y. Lee, H. D. Roh, and Y.-B. Park, “Novel structural health monitoring method for cfrps using electrical resistance based probabilistic sensing cloud,” *Composites Science and Technology*, vol. 213, p. 108 812, 2021.

[48] H. D. Roh, S. Y. Oh, and Y.-B. Park, “Self-sensing impact damage in and non-destructive evaluation of carbon fiber-reinforced polymers using electrical resistance and the corresponding electrical route models,” *Sensors and Actuators A: Physical*, vol. 332, p. 112 762, 2021.

[49] T. Tallman, “Damage detection in nanofiller-modified composites with external circuitry via resonant frequency shifts,” in *Smart Materials, Adaptive Structures and Intelligent Systems*, American Society of Mechanical Engineers, vol. 51951, 2018, V002T05A007.

[50] J. Abry, Y. Choi, A. Chateauminois, B. Dalloz, G. Giraud, and M. Salvia, “In-situ monitoring of damage in cfrp laminates by means of ac and dc measurements,” *Composites science and technology*, vol. 61, no. 6, pp. 855–864, 2001.

[51] X. Lu, A. Zhang, O. Dubrunfaut, D. He, L. Pichon, and J. Bai, “Numerical modeling and experimental characterization of the ac conductivity and dielectric properties of cnt/polymer nanocomposites,” *Composites Science and Technology*, vol. 194, p. 108 150, 2020.

[52] L. Helseth, “Electrical impedance spectroscopy of multiwall carbon nanotube–pdms composites under compression,” *Materials Research Express*, vol. 5, no. 10, p. 105 002, 2018.

[53] T. N. Tallman and D. J. Smyl, “Structural health and condition monitoring via electrical impedance tomography in self-sensing materials: A review,” *Smart Materials and Structures*, vol. 29, no. 12, p. 123 001, 2020.

[54] S. Gupta, J. G. Gonzalez, and K. J. Loh, “Self-sensing concrete enabled by nano-engineered cement-aggregate interfaces,” *Structural Health Monitoring*, vol. 16, no. 3, pp. 309–323, 2017.

[55] T. N. Tallman and K.-W. Wang, “Damage and strain identification in multifunctional materials via electrical impedance tomography with constrained sine wave solutions,” *Structural Health Monitoring*, vol. 15, no. 2, pp. 235–244, 2016.

[56] T. Tallman, S. Gungor, K. Wang, and C. E. Bakis, “Damage detection and conductivity evolution in carbon nanofiber epoxy via electrical impedance tomography,” *Smart Materials and Structures*, vol. 23, no. 4, p. 045 034, 2014.

[57] T. Tallman and J. Hernandez, “The effect of error and regularization norms on strain and damage identification via electrical impedance tomography in piezoresistive nanocomposites,” *NDT & E International*, vol. 91, pp. 156–163, 2017.

[58] R. P. Henderson and J. G. Webster, “An impedance camera for spatially specific measurements of the thorax,” *IEEE Transactions on Biomedical Engineering*, no. 3, pp. 250–254, 1978.

[59] R. Harikumar, R. Prabu, and S. Raghavan, “Electrical impedance tomography (eit) and its medical applications: A review,” *Int. J. Soft Comput. Eng*, vol. 3, no. 4, pp. 193–198, 2013.

[60] H. S. Tapp, A. Peyton, E. K. Kemsley, and R. H. Wilson, “Chemical engineering applications of electrical process tomography,” *Sensors and Actuators B: Chemical*, vol. 92, no. 1-2, pp. 17–24, 2003.

[61] R. Tomasz, K. Grzegorz, C. Tomasz, and K. Edward, “Application of a neural eit system to control the processes,” in *2018 Applications of Electromagnetics in Modern Techniques and Medicine (PTZE)*, IEEE, 2018, pp. 216–219.

[62] T.-C. Hou, K. J. Loh, and J. P. Lynch, “Electrical impedance tomography of carbon nanotube composite materials,” in *Sensors and Smart Structures Technologies for Civil, Mechanical, and Aerospace Systems 2007*, International Society for Optics and Photonics, vol. 6529, 2007, p. 652 926.

[63] W. Fan, H. Wang, and Z. Cui, “Damage detection of cfrp composites using open electrical impedance tomography,” in *2015 IEEE International Instrumentation and Measurement Technology Conference (I2MTC) Proceedings*, IEEE, 2015, pp. 1377–1381.

[64] T.-C. Hou, K. J. Loh, and J. P. Lynch, “Spatial conductivity mapping of carbon nanotube composite thin films by electrical impedance tomography for sensing applications,” *Nanotechnology*, vol. 18, no. 31, p. 315 501, 2007.

[65] T. N. Tallman, S. Gungor, K. Wang, and C. E. Bakis, “Damage detection via electrical impedance tomography in glass fiber/epoxy laminates with carbon black filler,” *Structural Health Monitoring*, vol. 14, no. 1, pp. 100–109, 2015.

[66] L. Miao, Y. Ma, X. Xiong, X. Chen, T. Han, P. Cai, P. Qin, and X. Ji, “A new symmetric semi-parallel electrical impedance tomography (eit) system-i: The design,” in *2016 IEEE International Conference on Imaging Systems and Techniques (IST)*, IEEE, 2016, pp. 19–23.

[67] M. Kranjc, B. Markelc, F. Bajd, M. Čemažar, I. Serša, T. Blagus, and D. Miklavčič, "In situ monitoring of electric field distribution in mouse tumor during electroporation," *Radiology*, vol. 274, no. 1, pp. 115–123, 2015.

[68] V. Cherepenin, A. Karpov, A. Korjenevsky, V. Kornienko, A. Mazaletskaya, D. Mazourov, and D. Meister, "A 3d electrical impedance tomography (eit) system for breast cancer detection," *Physiological measurement*, vol. 22, no. 1, p. 9, 2001.

[69] Y. Zou and Z. Guo, "A review of electrical impedance techniques for breast cancer detection," *Medical engineering & physics*, vol. 25, no. 2, pp. 79–90, 2003.

[70] S. Hong, K. Lee, U. Ha, H. Kim, Y. Lee, Y. Kim, and H.-J. Yoo, "A 4.9 mΩ-sensitivity mobile electrical impedance tomography ic for early breast-cancer detection system," *IEEE Journal of Solid-State Circuits*, vol. 50, no. 1, pp. 245–257, 2014.

[71] Z. Zhao, I. Frerichs, S. Pulletz, U. Müller-Lisse, and K. Möller, "The influence of image reconstruction algorithms on linear thorax eit image analysis of ventilation," *Physiological measurement*, vol. 35, no. 6, p. 1083, 2014.

[72] V. Cherepenin, A. Karpov, A. Korjenevsky, V. Kornienko, Y. Kultiasov, A. Mazaletskaya, and D. Mazourov, "Preliminary static eit images of the thorax in health and disease," *Physiological measurement*, vol. 23, no. 1, p. 33, 2001.

[73] A. Adler, M. B. Amato, J. H. Arnold, R. Bayford, M. Bodenstein, S. H. Böhm, B. H. Brown, I. Frerichs, O. Stenqvist, N. Weiler, *et al.*, "Whither lung eit: Where are we, where do we want to go and what do we need to get there?" *Physiological measurement*, vol. 33, no. 5, p. 679, 2012.

[74] B. Brown, D. Barber, A. Leathard, L. Lu, W. Wang, R. Smallwood, and A. Wilson, "High frequency eit data collection and parametric imaging," *Innovation et technologie en biologie et médecine*, vol. 15, pp. 1–8, 1994.

[75] B. McDermott, M. O'Halloran, J. Avery, and E. Porter, "Bi-frequency symmetry difference eit—feasibility and limitations of application to stroke diagnosis," *IEEE journal of biomedical and health informatics*, vol. 24, no. 8, pp. 2407–2419, 2019.

[76] N. Chauveau, B. Ayeva, B. Rigaud, and J. Morucci, "A multifrequency serial eit system," *Physiological measurement*, vol. 17, no. 4A, A7, 1996.

[77] C. Wu and M. Soleimani, "Frequency difference eit with localization: A potential medical imaging tool during cancer treatment," *IEEE Access*, vol. 7, pp. 21 870–21 878, 2019.

[78] A. Borsic, B. M. Graham, A. Adler, and W. R. Lionheart, "Total variation regularization in electrical impedance tomography," 2007.

[79] G.-H. Feng and J.-W. Tsai, “3d omnidiectional contollable elastic ipmc tweezer with self-sensing and adjustable clamping force abilities for biomedical applications,” in *2011 16th International Solid-State Sensors, Actuators and Microsystems Conference*, IEEE, 2011, pp. 1725–1728.

[80] A. A. Basheer, “Advances in the smart materials applications in the aerospace industries,” *Aircraft Engineering and Aerospace Technology*, vol. 92, no. 7, pp. 1027–1035, 2020.

[81] M. Arena, L. Vertuccio, G. Barra, M. Viscardi, and L. Guadagno, “Dynamic performance of self-sensing epoxy resin for aerospace structures,” in *AIP Conference Proceedings*, AIP Publishing LLC, vol. 1981, 2018, p. 020 066.

[82] S. Rana, P. Subramani, R. Fangueiro, and A. G. Correia, “A review on smart self-sensing composite materials for civil engineering applications,” *AIMS Materials Science*, vol. 3, no. 2, pp. 357–379, 2016.

[83] D. L. Castañeda-Saldarriaga, J. Alvarez-Montoya, V. Martínez-Tejada, and J. Sierra-Pérez, “Toward structural health monitoring of civil structures based on self-sensing concrete nanocomposites: A validation in a reinforced-concrete beam,” *International Journal of Concrete Structures and Materials*, vol. 15, no. 1, pp. 1–18, 2021.

[84] M. Abdullah, L. Khuan, N. Madzhi, M. Masrie, and A. Ahmad, “Development of a transduction circuit for piezoresistive mems sensor for biosensing,” in *2009 IEEE Symposium on Industrial Electronics & Applications*, IEEE, vol. 2, 2009, pp. 679–683.

[85] C.-Y. Wang, P. Sundaram, and R. E. Goodman, “Electrical resistivity changes in rocks during frictional sliding and fracture,” in *Rock Friction and Earthquake Prediction*, Springer, 1978, pp. 717–731.

[86] C. Vipulanandan and K. Ali, “Smart portland cement curing and piezoresistive behavior with montmorillonite clay soil contamination,” *Cement and Concrete Composites*, vol. 91, pp. 42–52, 2018.

[87] C. Grimaldi, P. Ryser, and S. Strässler, “Longitudinal and transverse piezoresistive response of granular metals,” *Physical review B*, vol. 64, no. 6, p. 064 201, 2001.

[88] R. Gaska, M. Shur, A. Bykhovski, J. Yang, M. Khan, V. Kaminski, and S. Soloviov, “Piezoresistive effect in metal–semiconductor–metal structures on p-type gan,” *Applied Physics Letters*, vol. 76, no. 26, pp. 3956–3958, 2000.

[89] M. Knight, “Effect of structure on the piezoresistive properties of thin metal films,” *Journal of Vacuum Science and Technology*, vol. 6, no. 4, pp. 706–710, 1969.

[90] X. Wang and D. Chung, "Short-carbon-fiber-reinforced epoxy as a piezoresistive strain sensor," *Smart Materials and Structures*, vol. 4, no. 4, p. 363, 1995.

[91] H. Montazerian, A. Dalili, A. Milani, and M. Hoorfar, "Piezoresistive sensing in chopped carbon fiber embedded pdms yarns," *Composites Part B: Engineering*, vol. 164, pp. 648–658, 2019.

[92] A. Biabangard Oskouyi, "Conductive filler modified polymers for structural health monitoring applications," 2015.

[93] H. Ahmadimoghaddamseighalani, "A stochastic finite element analysis framework for the multiple physical modeling of filler modified polymers," 2021.

[94] R. Riedel, L. Toma, E. Janssen, J. Nuffer, T. Melz, and H. Hanselka, "Piezoresistive effect in sioc ceramics for integrated pressure sensors," *Journal of the American Ceramic Society*, vol. 93, no. 4, pp. 920–924, 2010.

[95] E. Ricohermoso III, F. Rosenburg, F. Klug, N. Nicoloso, H. F. Schlaak, R. Riedel, and E. Ionescu, "Piezoresistive carbon-containing ceramic nanocomposites–a review," *Open Ceramics*, vol. 5, p. 100 057, 2021.

[96] S. Sun, B. Han, S. Jiang, X. Yu, Y. Wang, H. Li, and J. Ou, "Nano graphite platelets-enabled piezoresistive cementitious composites for structural health monitoring," *Construction and Building Materials*, vol. 136, pp. 314–328, 2017.

[97] W. Dong, W. Li, K. Wang, and S. P. Shah, "Physicochemical and piezoresistive properties of smart cementitious composites with graphene nanoplates and graphite plates," *Construction and Building Materials*, vol. 286, p. 122 943, 2021.

[98] A. Dehghani and F. Aslani, "Piezoresistive sensing of cementitious composites reinforced with shape memory alloy, steel, and carbon fibres," *Construction and Building Materials*, vol. 267, p. 121 046, 2021.

[99] G. m. Koo, *On the development of macroscale modeling strategies for ac/dc transport-deformation coupling in self-sensing piezoresistive materials*, 2020. DOI: 10.25394/PGS.13108172.v1. [Online]. Available: https://hammer.purdue.edu/articles/thesis/On_the_development_of_Macroscale_Modeling_Strategies_for_AC_DC_Transport-Deformation_Coupling_in_Self-Sensing_Piezoresistive_Materials/13108172/1.

[100] T. Tallman and K. Wang, "The influence of nanofiller alignment on transverse percolation and conductivity," *Nanotechnology*, vol. 26, no. 2, p. 025 501, 2014.

[101] T. N. Tallman and H. Hassan, "A computational exploration of the effect of alignment and aspect ratio on alternating current conductivity in carbon nanofiber–modified epoxy," *Journal of Intelligent Material Systems and Structures*, vol. 31, no. 5, pp. 756–770, 2020.

[102] A. Sanli, C. Müller, O. Kanoun, C. Elibol, and M. F.-X. Wagner, "Piezoresistive characterization of multi-walled carbon nanotube-epoxy based flexible strain sensitive films by impedance spectroscopy," *Composites Science and Technology*, vol. 122, pp. 18–26, 2016.

[103] H. Hassan, F. Semperlotti, K.-W. Wang, and T. N. Tallman, "Enhanced imaging of piezoresistive nanocomposites through the incorporation of nonlocal conductivity changes in electrical impedance tomography," *Journal of Intelligent Material Systems and Structures*, vol. 29, no. 9, pp. 1850–1861, 2018.

[104] Y. Wang, X. Zhao, and Y. Zhao, "Piezoresistivity of cement matrix composites incorporating multiwalled carbon nanotubes due to moisture variation," *Advances in Civil Engineering*, vol. 2020, 2020.

[105] A. Meoni, A. D'Alessandro, A. Downey, E. García-Macías, M. Rallini, A. L. Materazzi, L. Torre, S. Laflamme, R. Castro-Triguero, and F. Ubertini, "An experimental study on static and dynamic strain sensitivity of embeddable smart concrete sensors doped with carbon nanotubes for shm of large structures," *Sensors*, vol. 18, no. 3, p. 831, 2018.

[106] A. O. Monteiro, P. B. Cachim, and P. M. Costa, "Self-sensing piezoresistive cement composite loaded with carbon black particles," *Cement and Concrete Composites*, vol. 81, pp. 59–65, 2017.

[107] J. Cho, A. R. Boccaccini, and M. S. Shaffer, "Ceramic matrix composites containing carbon nanotubes," *Journal of Materials Science*, vol. 44, no. 8, pp. 1934–1951, 2009.

[108] V. T. Rathod, J. S. Kumar, and A. Jain, "Polymer and ceramic nanocomposites for aerospace applications," *Applied Nanoscience*, vol. 7, no. 8, pp. 519–548, 2017.

[109] G. Wang, J. Yan, X. Yang, and X. Qing, "A flexible pressure sensor based on composite piezoresistive layer," *IEEE Sensors Journal*, vol. 22, no. 1, pp. 405–411, 2021.

[110] S. T. A. Hamdani and A. Fernando, "The application of a piezo-resistive cardiorespiratory sensor system in an automobile safety belt," *Sensors*, vol. 15, no. 4, pp. 7742–7753, 2015.

[111] K. Park, P. Tran, N. Deaton, and J. P. Desai, "Multi-walled carbon nanotube (mwcnt)/pdms-based flexible sensor for medical applications," in *2019 International Symposium on Medical Robotics (ISMR)*, IEEE, 2019, pp. 1–8.

[112] S. Bao and S. C. Tjong, "Mechanical behaviors of polypropylene/carbon nanotube nanocomposites: The effects of loading rate and temperature," *Materials Science and Engineering: A*, vol. 485, no. 1-2, pp. 508–516, 2008.

[113] S. C. Tjong, G. Liang, and S. Bao, "Electrical behavior of polypropylene/multiwalled carbon nanotube nanocomposites with low percolation threshold," *Scripta Materialia*, vol. 57, no. 6, pp. 461–464, 2007.

[114] S. Gong, D. Wu, Y. Li, M. Jin, T. Xiao, Y. Wang, Z. Xiao, Z. Zhu, and Z. Li, "Temperature-independent piezoresistive sensors based on carbon nanotube/polymer nanocomposite," *Carbon*, vol. 137, pp. 188–195, 2018, ISSN: 0008-6223. DOI: https://doi.org/10.1016/j.carbon.2018.05.029. [Online]. Available: https://www.sciencedirect.com/science/article/pii/S0008622318304883.

[115] S. Mondal, L. Nayak, M. Rahaman, A. Aldalbahi, T. K. Chaki, D. Khastgir, and N. C. Das, "An effective strategy to enhance mechanical, electrical, and electromagnetic shielding effectiveness of chlorinated polyethylene-carbon nanofiber nanocomposites," *Composites Part B: Engineering*, vol. 109, pp. 155–169, 2017, ISSN: 1359-8368. DOI: https://doi.org/10.1016/j.compositesb.2016.10.049. [Online]. Available: https://www.sciencedirect.com/science/article/pii/S1359836816307284.

[116] M. A. Rafiee, J. Rafiee, I. Srivastava, Z. Wang, H. Song, Z.-Z. Yu, and N. Koratkar, "Fracture and fatigue in graphene nanocomposites," *small*, vol. 6, no. 2, pp. 179–183, 2010.

[117] K. M. Shahil and A. A. Balandin, "Graphene–multilayer graphene nanocomposites as highly efficient thermal interface materials," *Nano letters*, vol. 12, no. 2, pp. 861–867, 2012.

[118] Z. Zhang, L. Zhang, S. Wang, W. Chen, and Y. Lei, "A convenient route to polyacrylonitrile/silver nanoparticle composite by simultaneous polymerization–reduction approach," *Polymer*, vol. 42, no. 19, pp. 8315–8318, 2001.

[119] K. Takei, Z. Yu, M. Zheng, H. Ota, T. Takahashi, and A. Javey, "Highly sensitive electronic whiskers based on patterned carbon nanotube and silver nanoparticle composite films," *Proceedings of the National Academy of Sciences*, vol. 111, no. 5, pp. 1703–1707, 2014.

[120] H. Jiang, K.-s. Moon, Y. Li, and C. Wong, "Surface functionalized silver nanoparticles for ultrahigh conductive polymer composites," *Chemistry of Materials*, vol. 18, no. 13, pp. 2969–2973, 2006.

[121] S. Nayak and S. Das, "Spatial damage sensing ability of metallic particulate-reinforced cementitious composites: Insights from electrical resistance tomography," *Materials & Design*, vol. 175, p. 107 817, 2019.

[122] D. Chung, “A critical review of piezoresistivity and its application in electrical-resistance-based strain sensing,” *Journal of Materials Science*, vol. 55, no. 32, pp. 15 367–15 396, 2020.

[123] S. Wen and D. Chung, “Piezoresistivity-based strain sensing in carbon fiber-reinforced cement,” *ACI materials journal*, vol. 104, no. 2, p. 171, 2007.

[124] Y. Yao, X. Duan, J. Luo, and T. Liu, “Two-probe versus van der pauw method in studying the piezoresistivity of single-wall carbon nanotube thin films,” *Nanotechnology*, vol. 28, no. 44, p. 445 501, 2017.

[125] D. K. Schroder, *Semiconductor material and device characterization.* John Wiley & Sons, 2015.

[126] A. Downey, A. D’Alessandro, F. Ubertini, S. Laflamme, and R. Geiger, “Biphasic dc measurement approach for enhanced measurement stability and multi-channel sampling of self-sensing multi-functional structural materials doped with carbon-based additives,” *Smart Materials and Structures*, vol. 26, no. 6, p. 065 008, 2017.

[127] A. Al-Dahawi, G. Yıldırım, O. Öztürk, and M. Şahmaran, “Assessment of self-sensing capability of engineered cementitious composites within the elastic and plastic ranges of cyclic flexural loading,” *Construction and Building Materials*, vol. 145, pp. 1–10, 2017.

[128] A. Downey, E. Garcia-Macias, A. D’Alessandro, S. Laflamme, R. Castro-Triguero, and F. Ubertini, “Continuous and embedded solutions for shm of concrete structures using changing electrical potential in self-sensing cement-based composites,” in *Nondestructive Characterization and Monitoring of Advanced Materials, Aerospace, and Civil Infrastructure 2017*, International Society for Optics and Photonics, vol. 10169, 2017, 101691G.

[129] A. Adler and D. Holder, *Electrical impedance tomography: methods, history and applications.* CRC Press, 2021.

[130] T. N. Tallman, “Conductivity-based nanocomposite structural health monitoring via electrical impedance tomography.,” Ph.D. dissertation, 2015.

[131] M. Cheney, D. Isaacson, J. C. Newell, S. Simske, and J. Goble, “Noser: An algorithm for solving the inverse conductivity problem,” *International Journal of Imaging systems and technology*, vol. 2, no. 2, pp. 66–75, 1990.

[132] T. J. Yorkey, J. G. Webster, and W. J. Tompkins, “Comparing reconstruction algorithms for electrical impedance tomography,” *IEEE Transactions on Biomedical Engineering*, no. 11, pp. 843–852, 1987.

[133] D. Barber and B. Brown, “Applied potential tomography.,” *Journal of the British Interplanetary Society*, vol. 42, no. 7, pp. 391–393, 1989.

[134] Z. Zhou, G. S. dos Santos, T. Dowrick, J. Avery, Z. Sun, H. Xu, and D. S. Holder, "Comparison of total variation algorithms for electrical impedance tomography," *Physiological measurement*, vol. 36, no. 6, p. 1193, 2015.

[135] A. Adler, J. H. Arnold, R. Bayford, A. Borsic, B. Brown, P. Dixon, T. J. Faes, I. Frerichs, H. Gagnon, Y. Gärber, *et al.*, "Greit: A unified approach to 2d linear eit reconstruction of lung images," *Physiological measurement*, vol. 30, no. 6, S35, 2009.

[136] S. C. Jun, J. Kuen, J. Lee, E. J. Woo, D. Holder, and J. K. Seo, "Frequency-difference eit (fdeit) using weighted difference and equivalent homogeneous admittivity: Validation by simulation and tank experiment," *Physiological measurement*, vol. 30, no. 10, p. 1087, 2009.

[137] A. Thomas, J. Kim, T. Tallman, and C. Bakis, "Damage detection in self-sensing composite tubes via electrical impedance tomography," *Composites Part B: Engineering*, vol. 177, p. 107 276, 2019.

[138] H. Hassan, "On the use of metaheuristic algorithms for solving conductivity-to-mechanics inverse problems in structural health monitoring of self-sensing composites," Ph.D. dissertation, Purdue University Graduate School, 2021.

[139] I. T. Karnik and T. Tallman, "The effect of fatigue loading on electrical impedance in open-hole carbon nanofiber-modified glass fiber/epoxy composites," in *Smart Materials, Adaptive Structures and Intelligent Systems*, American Society of Mechanical Engineers, vol. 84027, 2020, V001T05A001.

[140] Jetpack, *Pr-24-xt-hht*. [Online]. Available: https://apsci.com/product/pr-24-xt-hht/.

[141] *Homepage*. [Online]. Available: https://www.dewalt.com/.

[142] A. K. Jonscher, "The 'universal'dielectric response," *nature*, vol. 267, no. 5613, pp. 673–679, 1977.

[143] J.-B. Kim and C.-G. Kim, "Study on the semi-empirical model for the complex permittivity of carbon nanocomposite laminates in microwave frequency band," *Composites science and technology*, vol. 70, no. 12, pp. 1748–1754, 2010.

[144] M. S. Sannamani, "The role of sensitivity matrix formulation on damage detection via eit in non-planar cfrp laminates with surface-mounted electrodes," Ph.D. dissertation, Purdue University Graduate School, 2021.

[145] K. J. Loh, J. P. Lynch, B. Shim, and N. Kotov, "Tailoring piezoresistive sensitivity of multilayer carbon nanotube composite strain sensors," *Journal of intelligent material systems and structures*, vol. 19, no. 7, pp. 747–764, 2008.

[146] Z. Chen, J. Xiang, P. Bagnaninchi, and Y. Yang, “Mmv-net: A multiple measurement vector network for multi-frequency electrical impedance tomography,” *arXiv preprint arXiv:2105.12474*, 2021.

[147] H. Wu, Y. Yang, and J. Jia, “A simplified calibration method for multi-frequency eit system,” *ELECTRICAL IMPEDANCE TOMOGRAPHY!*, p. 64, 2017.

[148] I. T. Karnik and T. N. Tallman, “An experimental study on the effect of fatigue loading on electrical impedance in open-hole carbon nanofiber-modified glass fiber/epoxy composites,” *Composite Structures*, vol. 276, p. 114 463, 2021.

A. DETAILED FORWARD PROBLEM FORMULATION

This appendix will detail the finite element formulation of the forward problem of EIT as shown in the Theory chapter. Note that all notations used in the previous chapters have been dropped. All the derivations shown in the appendix are referenced from [130].

A.1 Steady State Diffusion Weak Form and Discretization

The steady state diffusion equation is given in the following equation.

$$-\frac{\partial j_{\mathrm{i}}}{\partial x_{\mathrm{i}}} = \frac{\partial}{\partial x_{\mathrm{j}}} \xi_{\mathrm{ij}} \frac{\partial u}{\partial x_{\mathrm{j}}} = f \tag{A.1}$$

In the equation, j_{i} is the current density vector, ξ_{ij} is the (potentially) anisotropic admittivity tensor, u is the domain potential, and f is the internal current source. For anisotropic transport, the admittivity is a symmetric second-order tensor. Isotropic transport can be recovered by letting $\xi_{\mathrm{ij}} = \xi \delta_{\mathrm{ij}}$, where δ_{ij} is the Kronecker-delta. Assuming the current only flows through electrodes, and no current flows through the boundaries without electrodes. In addition, enforce the principle of conservation of charge that the net current through the electrodes is zero. The boundary conditions can be shown in the following equations.

$$\int_{E_l} \xi_{\mathrm{ij}} \frac{\partial u}{\partial x_{\mathrm{i}}} n_{\mathrm{j}} \, \mathrm{d}S_l = I_l \tag{A.2}$$

$$\xi_{\mathrm{ij}} \frac{\partial u}{\partial x_{\mathrm{i}}} n_{\mathrm{j}} = 0 \text{ off} \bigcup_{l=1}^{L} E_l \tag{A.3}$$

$$\sum_{l=1}^{L} I_l = 0 \tag{A.4}$$

In the equations above, n_{j} is the outward pointing normal and L is the total number of electrodes in the domain. Next, the weak form of steady state diffusion equation shown in equation A.1 is formulated by multiplying it by a weighting function ϕ that satisfies the Dirichlet boundary conditions and integrating the result over the domain.

$$\int_{\Omega} \psi \frac{\partial}{\partial x_{\mathrm{j}}} \xi_{\mathrm{ij}} \frac{\partial u}{\partial x_{\mathrm{j}}} \, \mathrm{d}\Omega = \int_{\Omega} \psi f \, \mathrm{d}\Omega \tag{A.5}$$

Assuming the internal sources is absence, $f = 0$, and apply Green's second identity along with the vector identity to equation A.5, the equation becomes

$$\int_{\Omega} \frac{\partial}{\partial x_{\mathrm{j}}} \psi \xi_{\mathrm{ij}} \frac{\partial u}{\partial x_{\mathrm{i}}} \, \mathrm{d}\Omega - \int_{\Omega} \frac{\partial \psi}{\partial x_{\mathrm{i}}} \xi_{\mathrm{ij}} \frac{\partial u}{\partial x_{\mathrm{j}}} \, \mathrm{d}\Omega = 0 \tag{A.6}$$

Applying the divergence theorem to equation A.6, it becomes

$$\int_{\Omega} \frac{\partial \psi}{\partial x_{\mathrm{i}}} \xi_{\mathrm{ij}} \frac{\partial u}{\partial x_{\mathrm{j}}} \, \mathrm{d}\Omega = \int_{\partial\Omega} \psi \xi_{\mathrm{ij}} \frac{\partial u}{\partial x_{\mathrm{i}}} n_{\mathrm{j}} \, \mathrm{d}S = \int_{\Gamma} \xi_{\mathrm{ij}} \frac{\partial u}{\partial x_{\mathrm{j}}} n_{\mathrm{j}} \psi \, \mathrm{d}S \tag{A.7}$$

Here, $\Gamma = \cup_l E_l$ is the union of the electrodes. Substituting equation 3.9 into equation A.7 results in the equation shown below.

$$\int_{\Omega} \frac{\partial \psi}{\partial x_{\mathrm{i}}} \xi_{\mathrm{ij}} \frac{\partial u}{\partial x_{\mathrm{j}}} \, \mathrm{d}\Omega = \sum_{l=1}^{L} \int_{E_l} \frac{1}{z_l} \left(V_l - u\right) \psi \, \mathrm{d}S_l \tag{A.8}$$

Equation A.8 is discretized by partitioning the domain Ω into disjoint subsets Ω_{e} so that it can be expressed as an assembly of subsets as shown in equation A.9 below.

$$\sum_{\mathrm{e}} \int_{\Omega_{\mathrm{e}}} \frac{\partial \psi_{\mathrm{e}}}{\partial x_{\mathrm{i}}} \xi_{\mathrm{ij}} \frac{\partial u_{\mathrm{e}}}{\partial x_{\mathrm{j}}} \, \mathrm{d}\Omega_{\mathrm{e}} = \sum_{\mathrm{e}} \sum_{l=1}^{L} \int_{\partial\Omega_{\mathrm{e}}} \frac{1}{z_l} \left(V_l - u_{\mathrm{e}}\right) \psi_{\mathrm{e}} \, \mathrm{d}S_{\mathrm{e}} \tag{A.9}$$

The u_{e} and ψ_{e} can be expressed element-wise as shown below.

$$u_{\mathrm{e}} = \sum_{A=1}^{N} w^A d_{\mathrm{e}}^A \tag{A.10}$$

$$\psi_{\mathrm{e}} = \sum_{A=1}^{N} w^A c_{\mathrm{e}}^A \tag{A.11}$$

In the equation above, d_{e}^A is the solution to the forward problem at the Ath node of the eth element and c_{e}^A is the variation of the Ath node of the eth element. Equation A.10 is the interpolation of the nodal solutions over the eth element and summed over N nodes per element.

A.2 Formulation of Finite Element Matrices

Substitute equation A.10 and A.11 back into equation A.9, the result equation can be shown below.

$$\int_{\Omega_\mathrm{e}} \frac{\partial \psi_\mathrm{e}}{\partial x_\mathrm{i}} \xi_\mathrm{ij} \frac{\partial u_\mathrm{e}}{\partial x_\mathrm{j}} \, \mathrm{d}\Omega_\mathrm{e} = \sum_{A=1}^{N} \sum_{B=1}^{N} c_\mathrm{e}^A \int_{\Omega_\mathrm{e}} \frac{\partial w^A}{\partial x_\mathrm{i}} \xi_\mathrm{ij} \frac{\partial w^B}{\partial x_\mathrm{j}} \, \mathrm{d}\Omega_\mathrm{e} d_\mathrm{e}^B \tag{A.12}$$

The c_e^A and d_e^A can be pulled out of the integral as they are both constants. The interpolation functions are then defined on an isoparametric domain given as

$$x_\mathrm{i} = \sum_{A=1}^{N} w^A(\zeta) x_\mathrm{i}^A \tag{A.13}$$

where x_i^A refers to the i-coordinate of the Ath node. Using the chain rule of differentiation, the gradient of the interpolation functions can be formed as

$$\frac{\partial w^A}{\partial x_\mathrm{i}} = \frac{\partial w^A}{\partial \zeta_\mathrm{j}} \frac{\partial \zeta_\mathrm{j}}{\partial x_\mathrm{i}} \tag{A.14}$$

The $\partial \zeta_\mathrm{i} / \partial x_\mathrm{j}$ is the inverse of $\partial x_\mathrm{i} / \partial \zeta_\mathrm{j}$. This is formed by differentiation equation A.13. Equation A.12 can be rewritten as the equation shown below.

$$\int_{\Omega_\mathrm{e}} \frac{\partial \psi_\mathrm{e}}{\partial x_\mathrm{i}} \xi_\mathrm{ij} \frac{\partial u_\mathrm{e}}{\partial x_\mathrm{j}} \mathrm{d}\Omega_\mathrm{e} = \sum_{A=1}^{N} \sum_{B=1}^{N} c_\mathrm{e}^A \int_{\Omega_\mathrm{e}} \frac{\partial w^A}{\partial \zeta_k} \frac{\partial \zeta_k}{\partial x_\mathrm{i}} \xi_\mathrm{ij} \frac{\partial w^B}{\partial \zeta_l} \frac{\partial \zeta_l}{\partial x_\mathrm{j}} \, \mathrm{d}\Omega_\mathrm{e} d_\mathrm{e}^B \tag{A.15}$$

Due the the isoparametric domain was used, the integrals can be exactly calculated using the numerical quadrature with appropriately selected Lagrange polynomials. The linear 2D triangle elements used in this thesis are gives as $w^1 = \zeta_1$, $w^2 = \zeta_2$, and $w^3 = 1 - \zeta_1 - \zeta_2$. To express equation A.15 in the isoparametric domain, it is mutiply by $\det|\partial x_\mathrm{i}/\partial \zeta_\mathrm{j}|$, and the result equation can be shown below.

$$\int_{\Omega_\mathrm{e}} \frac{\partial \psi_\mathrm{e}}{\partial x_\mathrm{i}} \xi_\mathrm{ij} \frac{\partial u_\mathrm{e}}{\partial x_\mathrm{j}} \, \mathrm{d}\Omega_\mathrm{e} = \sum_{A=1}^{N} \sum_{B=1}^{N} c_\mathrm{e}^A \int_{\Omega_{\mathrm{e}_\zeta}} \frac{\partial w^A}{\partial \zeta_k} \frac{\partial \zeta_k}{\partial x_\mathrm{i}} \xi_\mathrm{ij} \frac{\partial w^B}{\partial \zeta_l} \frac{\partial \zeta_l}{\partial x_\mathrm{j}} \det |\frac{\partial x_m}{\partial \zeta_n}| \, \mathrm{d}\Omega_{\mathrm{e}_\zeta} d_\mathrm{e}^B \tag{A.16}$$

The $\Omega_{\mathrm{e}_\zeta}$ in the above equation is the integral of the eth element in the isoparametric domain. Equation A.16 can now be evaluated as a sum of weighted polynomials evaluated at quadrature points as shown below.

$$\int_{\Omega_{\mathrm{e}_\zeta}} p(\zeta_l) \mathrm{d}\Omega_{\mathrm{e}_\zeta} = \sum_{m}^{M} a_m p(\zeta_m) \tag{A.17}$$

In the equation above, the summation runs over the number of quadrature points and a_m is the mth weight. Then, the elemental diffusion stiffness matrix can be formed as shown below.

$$\int_{\Omega_\mathrm{e}} \frac{\partial \psi_\mathrm{e}}{\partial x_\mathrm{i}} \xi_\mathrm{ij} \frac{\partial u_\mathrm{e}}{\partial x_\mathrm{j}} \, \mathrm{d}\Omega_\mathrm{e} = \sum_{A=1}^{N} \sum_{B=1}^{N} c_\mathrm{e}^A k_\mathrm{e}^{AB} d_\mathrm{e}^B = \begin{bmatrix} c_\mathrm{e}^1 & c_\mathrm{e}^2 & \dots & c_\mathrm{e}^N \end{bmatrix} \mathbf{k}_\mathrm{e} \begin{bmatrix} d_\mathrm{e}^1 \\ d_\mathrm{e}^2 \\ \vdots \\ d_\mathrm{e}^N \end{bmatrix} \tag{A.18}$$

Here, k_e^{AB} is the local diffusion matrix of the eth element and is assembled into the global diffusion matrix $\mathbf{A}_M$. The local stiffness matrix for the eth 2D triangle element is

$$\begin{aligned} \mathbf{k}_\mathrm{e} = \frac{1}{2} \begin{bmatrix} 1 & 0 \\ 0 & 1 \\ -1 & -1 \end{bmatrix} \begin{bmatrix} x_1^\mathrm{e} - x_3^\mathrm{e} & x_2^\mathrm{e} - x_3^\mathrm{e} \\ y_1^\mathrm{e} - y_3^\mathrm{e} & y_2^\mathrm{e} - y_3^\mathrm{e} \end{bmatrix}^{-1} \begin{bmatrix} \xi_{11} & \xi_{12} \\ \xi_{21} & \xi_{22} \end{bmatrix} \dots \\ \dots \begin{bmatrix} x_1^\mathrm{e} - x_3^\mathrm{e} & x_2^\mathrm{e} - x_3^\mathrm{e} \\ y_1^\mathrm{e} - y_3^\mathrm{e} & y_2^\mathrm{e} - y_3^\mathrm{e} \end{bmatrix}^{-T} \begin{bmatrix} 1 & 0 \\ 0 & 1 \\ -1 & -1 \end{bmatrix}^T \det \left| \begin{bmatrix} x_1^\mathrm{e} - x_3^\mathrm{e} & x_2^\mathrm{e} - x_3^\mathrm{e} \\ y_1^\mathrm{e} - y_3^\mathrm{e} & y_2^\mathrm{e} - y_3^\mathrm{e} \end{bmatrix} \right| \end{aligned} \tag{A.19}$$

The area of the triangle element is then

$$A^{\mathrm{e}} = \frac{1}{2}\det\begin{bmatrix} x_1^{\mathrm{e}} - x_3^{\mathrm{e}} & x_2^{\mathrm{e}} - x_3^{\mathrm{e}} \\ y_1^{\mathrm{e}} - y_3^{\mathrm{e}} & y_2^{\mathrm{e}} - y_3^{\mathrm{e}} \end{bmatrix} \tag{A.20}$$

Looking at equation A.9, $\mathbf{A}_Z$, $\mathbf{A}_W$, and $\mathbf{A}_D$ can be formed by evaluating the right hand side of the equation.

$$\sum_{\mathrm{e}} \int_{\partial\Omega_{\mathrm{e}}} \frac{1}{z_l}\left(V_l - u_{\mathrm{e}}\right)\psi_{\mathrm{e}}\,\mathrm{d}S_{\mathrm{e}} = \sum_{\mathrm{e}}\left(-\int_{\partial\Omega_{\mathrm{e}}}\frac{1}{z_l}u_{\mathrm{e}}\psi_{\mathrm{e}}\,\mathrm{d}S_{\mathrm{e}} + \int_{\partial\Omega_{\mathrm{e}}}\frac{1}{z_l}V_l\psi_{\mathrm{e}}\,\mathrm{d}S_{\mathrm{e}}\right) \tag{A.21}$$

The $\mathbf{A}_Z$ and $\mathbf{A}_W$ here are formed using interpolation functions one degree lower than the dimension of the domain. That is, $w^1 = 1/2(1-\zeta)$ and $w^2 = 1/2(1+\zeta)$ are used for domain functions of $w^1 = \zeta_1$, $w^2 = \zeta_2$, and $w^3 = 1 - \zeta_1 - \zeta_2$ to form $\mathbf{A}_Z$ and $\mathbf{A}_W$. The right hand side of equation A.21 is moved to the left hand side of equation A.9. The expressions from equation A.10 and A.11 are substituted into the equation.

For $\mathbf{A}_Z$, the first integral on the right hand side of equation A.21 is used and the eth element of the lth electrode are considered.

$$\int_{\Omega_{\mathrm{e}}}\frac{1}{z_l}u_{\mathrm{e}}\psi_{\mathrm{e}}\,\mathrm{d}S_{\mathrm{e}} = \sum_{A=1}^{N}\sum_{B=1}^{N} c_{\mathrm{e}}^{A}\int_{\Omega_{\mathrm{e}}}\frac{1}{z_l}w^A w^B\,\mathrm{d}S_{\mathrm{e}} d_{\mathrm{e}}^{B} = \begin{bmatrix} c_{\mathrm{e}}^1 & c_{\mathrm{e}}^2 & \dots & c_{\mathrm{e}}^N \end{bmatrix} \mathbf{A}_Z^{\mathrm{el}} \begin{bmatrix} d_{\mathrm{e}}^1 \\ d_{\mathrm{e}}^2 \\ \vdots \\ d_{\mathrm{e}}^N \end{bmatrix} \tag{A.22}$$

The the equation above can be evaluated to find $\mathbf{A}_Z^{el}$ matrix of the eth element of the lth electrode. The $\mathbf{A}_Z^{el}$ matrix of the eth linear triangle element of the lth electrode is

$$\mathbf{A}_Z^{\mathrm{el}} = \int_{-1}^{1}\frac{h^{\mathrm{e}}}{8z_l}\begin{bmatrix} 1 - 2\zeta + \zeta^2 & 1 - \zeta^2 \\ 1 - \zeta^2 & 1 + 2\zeta + \zeta^2 \end{bmatrix}\mathrm{d}\zeta = \frac{h^{\mathrm{e}}}{6z_l}\begin{bmatrix} 2 & 1 \\ 1 & 2 \end{bmatrix} \tag{A.23}$$

where h^{e} is the length of line element. $\mathbf{A}_Z^{el}$ is formed for every element part of the electrode and then assembled to form global $\mathbf{A}_Z$.

Matrix $\mathbf{A}_W$ relates the domain voltage to the electrode voltages. It is formed using the second integral on the right hand side of equation A.21 and consider the eth element of the lth electrode.

$$-\int_{\Omega_\mathrm{e}} \frac{1}{z_l} V_l \psi_\mathrm{e} \, \mathrm{d}S_\mathrm{e} = -\sum_{A=1}^{N} c_\mathrm{e}^A \int_{\Omega_\mathrm{e}} \frac{1}{z_l} w^A \, \mathrm{d}S_\mathrm{e} V_l = \begin{bmatrix} c_\mathrm{e}^1 & c_\mathrm{e}^2 & \dots & c_\mathrm{e}^N \end{bmatrix} \mathbf{A}_W^{\mathrm{e}l} V_l \tag{A.24}$$

The V_l is pulled out of the integral as the voltage is assumed to be constant on each electrode. From equation A.24, the $\mathbf{A}_W^{\mathrm{e}l}$ column vector of the eth linear line element of the lth electrode in 2D can be shown below.

$$\mathbf{A}_W^{\mathrm{e}l} = -\int_{-1}^{1} \frac{h^\mathrm{e}}{2z_l} \begin{bmatrix} \frac{1}{2}(1-\zeta) \\ \frac{1}{2}(1+\zeta) \end{bmatrix} \, \mathrm{d}\zeta = -\frac{h^\mathrm{e}}{2z_l} \begin{bmatrix} 1 \\ 1 \end{bmatrix} \tag{A.25}$$

The formation of $\mathbf{A}_D$ can be shown below. The current through the lth electrode is

$$I_l = \int_{E_l} \frac{1}{z_l}(V_l - u) \, \mathrm{d}S = \frac{1}{z_l} E_l V_l - \int_{E_l} \frac{1}{z_l} u \, \mathrm{d}S \tag{A.26}$$

Assuming the contact impedance and electrode voltage are constants, the first term on the right hand side of the equation above relates electrode current to the voltage by E_l/z_l, forming $\mathbf{A}_D$. The second term on the right hand side can be related to equation A.24 but with the nodal solution instead of the nodal variation. This accounts for the coupling of the domain voltage to the electrode voltage by $\mathbf{A}_W$.

B. SENSITIVITY MATRIX FORMULATION

Forming the sensitivity matrix is similar to the formulation of the finite element stiffness matrix discussed in Appendix A. In this section, the exact form of the sensitivity matrix entries for linear triangle elements that were unitized in this thesis will be derived.

B.1 Evaluation of Sensitivity Matrix Entries

The formation of the sensitivity matrix for anisotropic conductivity can be shown in the equation below. For the isotropic case, the equation can be simplified by substituting δ_{ij} for ξ_{ij}. Also note that QR has now being used as an index of the sensitivity matrix instead of the previously used MN. This was done to avoid using the same indices used to sum over the number of nodes per element.

$$J_{QR\mathrm{e}} = -\int_{\Omega_\mathrm{e}} \frac{\partial u^Q}{\partial x_\mathrm{i}} \xi_{\mathrm{ij}} \frac{\partial \bar{u}^R}{\partial x_\mathrm{j}} \,\mathrm{d}\Omega_\mathrm{e} \tag{B.1}$$

Substituting equation A.10 in equation B.1, the result equation can be shown below.

$$J_{QR\mathrm{e}} = -\int_{\Omega_\mathrm{e}} \frac{\partial u^Q}{\partial x_\mathrm{i}} \xi_{\mathrm{ij}} \frac{\partial \bar{u}^R}{\partial x_\mathrm{j}} \,\mathrm{d}\Omega_\mathrm{e} = -\sum_{A=1}^{N}\sum_{B=1}^{N} d_\mathrm{e}^{AQ} \int_{\Omega_\mathrm{e}} \frac{\partial w^A}{\partial x_\mathrm{i}} \xi_{\mathrm{ij}} \frac{\partial w^B}{\partial x_\mathrm{j}} \,\mathrm{d}\Omega_\mathrm{e} \bar{d}_\mathrm{e}^{BR} \tag{B.2}$$

The d_e^{AQ} in the equation above refers to the Ath nodal solution of the eth element due to the Qth injection, and $\bar{d}_\mathrm{e}^{BR}$ refers to the Bth nodal solution of the eth solution of the eth element due to a unit current injection by the Rth electrode measurement pair. The gradients of the interpolation function can now be evaluated via the chain rule. On integration in the isoparametric domain, the result equation can be shown below.

$$-\int_{\Omega_\mathrm{e}} \frac{\partial u^Q}{\partial x_\mathrm{i}} \xi_{\mathrm{ij}} \frac{\partial \bar{u}^R}{\partial x_\mathrm{j}} \,\mathrm{d}\Omega_\mathrm{e} = -\sum_{A=1}^{N}\sum_{B=1}^{N} d_\mathrm{e}^{AQ} \int_{\Omega_\mathrm{e}} \frac{\partial w^A}{\partial \zeta_k} \frac{\partial \zeta_k}{\partial x_\mathrm{i}} \xi_{\mathrm{ij}} \frac{\partial w^B}{\partial \zeta_l} \frac{\partial \zeta_l}{\partial x_\mathrm{j}} \det\left|\frac{\partial x_m}{\partial \zeta_n}\right| \mathrm{d}\Omega_\mathrm{e} \bar{d}_\mathrm{e}^{BR} \tag{B.3}$$

Using linear algrebra to express the summations, the result can be shown as

$$-\int_{\Omega_{\mathrm{e}}} \frac{\partial u^Q}{\partial x_{\mathrm{i}}} \xi_{\mathrm{ij}} \frac{\partial \bar{u}^R}{\partial x_{\mathrm{j}}} \,\mathrm{d}\Omega_{\mathrm{e}} = \sum_{A=1}^{N} \sum_{B=1}^{N} d_{\mathrm{e}}^{AQ} j_{\mathrm{e}}^{AB} d_{\mathrm{e}}^{BR} = \begin{bmatrix} d_{\mathrm{e}}^{1Q} & d_{\mathrm{e}}^{2Q} & \dots & d_{\mathrm{e}}^{NQ} \end{bmatrix} \mathbf{j}_{\mathrm{e}} \begin{bmatrix} \bar{d}_{\mathrm{e}}^{1R} \\ \bar{d}_{\mathrm{e}}^{2R} \\ \vdots \\ \bar{d}_{\mathrm{e}}^{NR} \end{bmatrix} \tag{B.4}$$

Evaluating $\mathbf{j}_{\mathrm{e}}$ for 2D triangle elements, the result can be shown below.

$$\begin{aligned} \mathbf{j}_{\mathrm{e}} = -\frac{1}{2} \begin{bmatrix} 1 & 0 \\ 0 & 1 \\ -1 & -1 \end{bmatrix} \begin{bmatrix} x_1^{\mathrm{e}} - x_3^{\mathrm{e}} & x_2^{\mathrm{e}} - x_3^{\mathrm{e}} \\ y_1^{\mathrm{e}} - y_3^{\mathrm{e}} & y_2^{\mathrm{e}} - y_3^{\mathrm{e}} \end{bmatrix}^{-1} \begin{bmatrix} \xi_{11} & \xi_{12} \\ \xi_{21} & \xi_{22} \end{bmatrix} \dots \\ \dots \begin{bmatrix} x_1^{\mathrm{e}} - x_3^{\mathrm{e}} & x_2^{\mathrm{e}} - x_3^{\mathrm{e}} \\ y_1^{\mathrm{e}} - y_3^{\mathrm{e}} & y_2^{\mathrm{e}} - y_3^{\mathrm{e}} \end{bmatrix}^{-T} \begin{bmatrix} 1 & 0 \\ 0 & 1 \\ -1 & -1 \end{bmatrix}^{T} \det \left| \begin{bmatrix} x_1^{\mathrm{e}} - x_3^{\mathrm{e}} & x_2^{\mathrm{e}} - x_3^{\mathrm{e}} \\ y_1^{\mathrm{e}} - y_3^{\mathrm{e}} & y_2^{\mathrm{e}} - y_3^{\mathrm{e}} \end{bmatrix} \right| \end{aligned} \tag{B.5}$$

It can be noticed that the formation of $\mathbf{j}_{\mathrm{e}}$ is simliar to the formation of $\mathbf{k}_{\mathrm{e}}$ shown in equation A.19. Comparing to the diffusion stiffness matrix formulation, the difference is that each entry calculated here is a scalar. This is because the nodal solutions d_{e}^{AQ} and $\bar{d}_{\mathrm{e}}^{BR}$ are know vectors, leading to scalar values. In the formation of the diffusion stiffness matrices, the contracting vectors were either variations to be minimized or solutions to be recovered.